Western Graduate&PostdoctoralStudies

Western University
Scholarship@Western

Electronic Thesis and Dissertation Repository

10-13-2016 12:00 AM

The Circumstellar Environments of B-emission Stars by Optical Interferometry

Bethany Grzenia, *The University of Western Ontario*

Supervisor: C. E. Jones, *The University of Western Ontario*

A thesis submitted in partial fulfillment of the requirements for the Doctor of Philosophy degree in Astronomy

© Bethany Grzenia 2016

Follow this and additional works at: https://ir.lib.uwo.ca/etd

 Part of the Stars, Interstellar Medium and the Galaxy Commons

Recommended Citation

Grzenia, Bethany, "The Circumstellar Environments of B-emission Stars by Optical Interferometry" (2016). *Electronic Thesis and Dissertation Repository*. 4216.
https://ir.lib.uwo.ca/etd/4216

This Dissertation/Thesis is brought to you for free and open access by Scholarship@Western. It has been accepted for inclusion in Electronic Thesis and Dissertation Repository by an authorized administrator of Scholarship@Western. For more information, please contact wlswadmin@uwo.ca.

Thesis advisor: Professor C. E. Jones Bethany Grzenia

Abstract

A series of B-emission (Be) stars was observed interferometrically and numerically modelled to be consistent with the observations. Uniform geometrical disks were used to make first-order inferences about the configuration of the disk systems' extended structures and their extent on the sky. Later, the BEDISK-BERAY-2DDFTpipeline was used to make sophisticated non-local thermodynamic equilibrium (LTE) calculations of the conditions within the disks.

In the first instance, sixteen stars were observed in the near-infrared (K-band, 2.2μm) with the Palomar Testbed Interferometer (PTI). The BEDISK portion of the pipeline was used to model disk temperature and density structures for B0, B2, B5 and B8 spectral types, which were then compared to observations of stars most closely matching one of these types. This is the first time such an extensive set of Be stars observed with long-baseline interferometry has been analyzed with self-consistent non-LTE numerical disk models.

The subsequent studies were focussed specifically on 48 Per and ψ Per. Both stars were observed with the Navy Precision Optical Interferometer (NPOI) in 2006-November and December, with additional observations taken of ψ Per in 2010-January and 2011-February. Hα spectra for both stars were recorded contemporaneously with the 2006 NPOI observations. Models were calculated with the full BEDISK-BERAY-2DDFT pipeline to produce spectral line profiles and synthetic images which were constrained via direct comparison with published studies including Quirrenbach et al. (1997) and Delaa et al. (2011). The results of these comparisons were generally favourable. The pipeline output was also used to estimate the mass of the 48 Per disk and to compute spectral energy distributions which were compared with those in Touhami et al. (2010). Although 48 Per is largely quiescent, ψ Per shows considerable variability over the epochs in which it was observed. The use of interferometry to probe the effects of variability on the extended structure is novel.

Keywords: stars, B-emission; optical interferometry; decretion disks; Hα spectroscopy

Coauthorship Statement

Chapter 2: PTI
My role: I completed a background literature search, chose n and $\rho_\circ$ input parameters for BEDISK and ran BEDISK for the spectral types appearing in the chapter. I determined the goodness-of-fit for the models that were produced, and used the results to construct temperature and density structures for the disk surrounding each star. I generated the majority of the plots appearing in the chapter (with exceptions as indicated) and took primary responsibility for the preparation of the manuscript.

C. E. Jones[*] (CEJ) ran and analyzed additional BEDISK models to fit ranges of n and $\rho_\circ$ to the disks of the program stars. CEJ was instrumental in developing and revising the manuscript. CEJ also advanced the Poeckert and Marlborough (1978) level population code as seen in Millar and Marlborough (1998) and codeveloped the BEDISK code with TAAS. BEDISK was used in Chapters 2, 3 and 4

C. Tycner[†] (CT) provided research support (including IDL codes for some tasks) for the modelling and analysis processes and significant input while preparing the manuscript. CT cowrote the NASA grant proposal with SAR.

T. A. A. Sigut[‡] (TAAS) provided the packaged BEDISK code and guidance for its use, as well as assistance with text revisions. TAAS cowrote the original BEDISK code (used in Chapters 2, 3 and 4) with CEJ.

S. A. Rinehart[‡] (SAR) cowrote with CT the NASA proposal to support the PTI archival work. SAR provided comments on the analysis of the PTI data and contributed to its scientific interpretation as well as assistance with preparing the manuscript for the chapter.

G. T. van Belle[§] (GTvB) provided software and assistance with data reduction for the analysis. GTvB also provided feedback on the analytical results as well as preliminary versions of the chapter.

Chapter 3: 48 Per
My role: I was responsible for background literature searches, calculating and analyzing mod-

[*]University of Western Ontario
[†]Central Michigan University, Mount Pleasant, MI, US
[‡]NASA Goddard Space Flight Center, Greenbelt, MD, US
[§]Lowell Observatory, Flagstaff, AZ, US

els with the Bedisk-Beray-2dDFT pipeline, and preparing the manuscript.

CEJ contributed to the analysis of 48 Per, particularly the sections pertaining to SEDs and disk mass estimates. CEJ also generated some of the data plots and contributed greatly to the preparation of the manuscript.

CT obtained interferometric and Hα observational data for 48 Per. In addition, CT assisted with data analysis and was involved with revising previous versions of the chapter.

TAAS developed and maintained the Beray and 2dDFT codes and provided assistance with the use of the Beray and 2dDFT codes. As well, TAAS supplied Matlab scripts that were used for analysis in Chapters 3 and 4. TAAS also assisted with manuscript preparation and creation of a number of the data plots appearing in this chapter.

R. T. Zavala[¶] assisted with data acquisition and reduction at NPOI.

Chapter 4: ψ Per
My role: I was responsible for work similar to what is described for Chapter 3.

CEJ performed a similar role as in Chapter 3.

CT provided similar assistance to that in Chapter 3, but observed ψ Per.

TAAS assisted with Chapter 4 in a manner nearly identical to Chapter 3.

[¶] United States Naval Observatory Flagstaff Station, Flagstaff, AZ, US

Acknowledgments

I would like to thank my supervisor, Prof. Carol Jones, for her guidance and assistance (and patience) over the last four years. I extend my gratitude as well to The University of Western Ontario, and the Physics and Astronomy Department, for their financial support. I would also like to recognize the other members of my advisory committee, Prof. Peter Brown, and Prof. Martin Houde, for their input. Prof. Aaron Sigut developed and provided the BERAY and 2DDFT codes, along with a number of plots used in interpreting the results of this work. I am grateful for this vital input.

I also thank our postdocs, Dave Stock, Anahí Granada, and Andy Pon for their valuable contributions toward the preparation of this thesis and the background work needed to bring it to completion, along with the countless hours they spent listening to my practice talks. I acknowledge with gratitude my past supervisors, Prof. Carlo Segre, Prof. Jeff Terry (Illinois Institute of Technology) and Prof. Chris Tycner (Central Michigan University) as well, for helping lay out the path that brought me to this point.

To my friends, here and elsewhere, who helped me maintain my sanity through this whole process–you have my most heartfelt thanks. Finally, to my parents, Paula and Paul...thanks, and good job.

This material in Chapter 2 is based upon work supported by the National Aeronautics and Space Administration under Grant No. NNX08AQ24A. The Palomar Testbed Interferometer is operated by the NASA Exoplanet Science Institute and the PTI collaboration and was constructed with funds from the Jet Propulsion Laboratory, Caltech, as provided by the National Aeronautics and Space Administration. BJG acknowledges support from Central Michigan University. This research has made use of services produced by the NASA Exoplanet Science Institute at the California Institute of Technology. This work is supported by the Canadian Natural Sciences and Engineering Research Council through Discovery Grants to TAAS and CEJ.

For Chapters 3 and 4, BJG recognizes support from The University of Western Ontario. CEJ and TAAS wish to acknowledge support though the Natural Sciences and Engineering Research Council of Canada. CT acknowledges support from Central Michigan University and NSF through grant AST-1614983. The Navy Precision Optical Interferometer, NPOI, is a joint project of the Naval Research Laboratory and the US Naval Observatory, in cooperation with Lowell Observatory and is funded by the Office of Naval Research and the Oceanographer of the Navy. We thank the Lowell Observatory for the telescope time used to obtain the Hα line spectra presented in this work and NPOI for the interferometry data.

This research has made use of the SIMBAD database, operated at CDS, Strasbourg, France.

Contents

List of tables

List of figures

"Wheels within wheels in a spiral array,
a pattern so grand and complex..."

Rush, "Natural Science"

1 Introduction

1.1 Introduction

B-emission, or Be stars, are hot and massive stars which possess decretion disks around their equatorial regions. Material in these disks originates from the surface of the central star and is launched into orbit. Unlike the more familiar case of accretion disks, material in decretion disks is carried outward and away from the central star by angular momentum transfer throughout the disk. Although they were regarded as a curiosity for some time, interest in Be stars has been renewed in recent years due to advances in instrumentation and the realization that understanding disks around one class of objects will contribute to understanding the disks that occur in so many other situations throughout the universe.

The first report of a Be star was made in 1866 by Angelo Secchi, a priest working in the observatory of the Collegio Romano. Secchi noted that the spectrum of γ Cassiopeiae contained a bright emission line, unlike the absorption lines more commonly seen in the spectra of other stars (Secchi, 1866). It was realized later that the bright emission line he observed was part of the Balmer emission spectrum associated with the circumstellar environment surrounding γ Cas (Porter and Rivinius, 2003). In 1931 Otto Struve suggested that the emission lines that define Be stars are the result of the environment in the immediate vicinity of the star (Struve, 1931). Struve surmised correctly that the attributes of the emission lines resulted from the presence of circumstellar disks oriented at different angles with respect to our line of sight.

Be stars present unique observational challenges. While conventional telescopes have al-

lowed astronomers to discern the presence of circumstellar material and infer that it is distributed in an equatorial disk, the limited angular resolution of conventional telescopes imposes a significant barrier to a full understanding of the Be phenomenon. Fortunately, interferometry has been developed, first in radio and more recently in near-infrared and optical wavelengths, to address this issue. The high angular resolution associated with interferometry permits astronomers to distinguish the star-plus-disk systems, and their inherent structure, from point sources. More recent advancements have begun to allow features within Be disks to be resolved (Tycner, 2011).

1.2 B-emission Stars

In the years since Secchi's report, the investigation of Be star environments has become an active area of research, particularly over the past decade as new observational technologies and increased computing power have become available. The hallmark of Be stars is the presence of a Balmer-series spectral emission line originating in the circumstellar environment due to radiative recombination. These lines are known in many cases to be transient; nonetheless, a star retains its Be classification even after its emission line is no longer observed (Harmanec, 1983).

While some might consider Be stars to be rather esoteric, one notes that disks are ubiquitous throughout the universe. Thus, it must be stated emphatically that although the study of decretion disks will necessarily produce some results that are applicable to only one disk type, researching the fundamental physics of Be star disks can yield knowledge that is valid for a broad array of astrophysical disks. A thorough understanding of disk dynamics will help astronomers understand the behaviour of not only these decretion disks, but may also provide insight to protoplanetary disks, active galactic nuclei, and the disks surrounding black holes, for example.

What follows is a discussion of B-type stars generally, and how the observed emission lines distinguish Be stars from their ordinary B counterparts.

1.2.1 Differentiating Ordinary B and B-emission Stars

Although the primary focus of this research is B-emission stars specifically, it is useful to discuss B-type stars generally. B-type stars are massive and occupy the upper left region of the HR diagram. Due to their mass, they fuse hydrogen into helium rapidly and their blackbody radiation peaks at shorter wavelengths (around 2000 Å (ultraviolet), compared to about 5000 Å (visible) for a star such as the Sun). In the visible range, these stars radiate much more strongly at the blue end of the spectrum rather than elsewhere, resulting in their bluish

appearance. Typically, B-type stars have masses ranging from about 4 to 18$M_\odot$ with corresponding effective temperatures of 11,000 to 30,000 kelvin (Cox, 2000). Unlike the Sun, which is expected to have a main-sequence lifetime of approximately of 10^{10} years, B-type stars tend to occupy the main sequence over timescales on the order of 10^7 years. Over the range of B-star masses, luminosity ranges from about 25,000 to 100,000$L_\odot$.

Although emission lines were the first distinguishing characteristic revealed by observation, as investigation continued a number of other important properties were discovered. Be star disks are known for their infrared excess resulting from free-free emission throughout the disk (Coté and Waters, 1987). Other emission lines, including He I and singly ionized metals, are commonly found (Porter and Rivinius, 2003). Polarization effects observed due to the interaction of the star and the material surrounding it lend significant support to the models in which the circumstellar material is distributed in an equatorial disk. Although the behaviour of a Be star at long wavelengths is a defining characteristic, this is not the case at short wavelengths. In the ultraviolet, Be stars have spectral energy distributions which are very similar to those found for ordinary B stars (Porter and Rivinius, 2003).

A number of questions about Be stars remain unanswered. For example, it is not understood whether all B stars undergo a Be phase over the course of their evolution. As well, it has been observed that the ratio of Be to ordinary B stars is highest for early types, with B2 stars being most likely to exhibit emission lines (Zorec and Briot, 1997). It is understood that the proportion of Be stars that has been estimated is most likely a lower limit due to the transient nature of the Be phenomenon. Averaged across all spectral classes, Porter and Rivinius (2003) estimate that about 17 percent of B-type stars show the Be phenomenon. This proportion increases for earlier B stars (Slettebak, 1982).

The presence of emission lines is not limited to so-called classical Be stars, which will be the focus of this work. The phenomenon has been seen as well in Herbig Be stars, in which case the lines arise from the stars' natal disks. B[e] stars, with thicker, dusty disks, are also associated with hydrogen Balmer emission. However, two important differences can be noted between Be and B[e] stars. First, Be stars are on the main sequence or are slightly evolved, some having reached the giant phase, while B[e] stars have evolved to the supergiant phase. Second, forbidden lines are observed in the spectra of the B[e] stars, hence the [e] designation in common with the notation for forbidden atomic transitions. Some additional configurations are also associated with the Be phenomenon. These include Algols, composed of main sequence or slightly evolved stars in a semidetached binary system; and β Cephei stars, early B stars in which pulsation is driven by iron. The emission lines in a classical Be star, however, are produced in a thin, gaseous disk in orbit around the star's equator.

1.2.2 Rapid Rotation

Be stars are also known to be rapid rotators, with rotation rates significantly in excess of rates seen for ordinary B stars. It is understood that the rate of rotation among Be stars is approaching the critical velocity, at which the star's self-gravity would be completely counteracted by the force at which material is projected outward, resulting in breakup of the star.

Critical velocity is defined as

$$V_c = \left(\frac{GM_*}{R_e}\right)^{1/2} = \left(\frac{2GM_*}{3R_p}\right)^{1/2}, \tag{1.1}$$

where R_e and R_p are the equatorial and polar radii, respectively, and M_* is the stellar mass (Townsend, Owocki, and Howarth, 2004). The different radii are related to the star's oblateness. The line extending from the centre of the star to its surface at the equator, R_e, becomes elongated due to the rapid rotation of the star; elongation along the line from the centre to the pole is minimal. One study (Yudin, 2001) showed that among a sample of 463 Be stars, all were rotating at less than critical velocity. Interestingly, the speed of rotation with respect to the critical speed increases with later spectral types. For example, Yudin (2001) noted that the ratio of $V_e \sin i$ to critical speed averaged to 0.55 for B2V to B2.5V stars. For B6V to B9.5V, the average increased to 0.78. It was also shown that over the entire sample, the distribution of $V_e \sin i$ values peaked around 220 km s^{-1}. Here, V_e is defined as the rotational velocity of the star at its equator, and i is the inclination angle of the star's rotational axis with respect to our line of sight.

Townsend, Owocki, and Howarth (2004) state that $V_e \sin i$ may be "systematically underestimating $V_e \sin i$". Rotation as a means of removing material from a star in order to form a disk was proposed initially by Struve (1931). Stars rotating at about 70 percent of critical are too slow to eject material without the aid of a secondary mechanism because the effective surface gravity is still too high. Effective surface gravity diminishes by about a factor of ten when the star is rotating around 95 percent of critical (Townsend, Owocki, and Howarth, 2004).

Rapid rotation also complicates estimation of a star's spectral type by distorting its photospheric lines, which introduces difficulties in modelling. For some stars a series of disparate spectral types is found in the literature. A good example of this can be found for KX Andromedae in Harmanec (1983). No fewer than ten spectral classes were found in the literature available at that time, ranging from B0 IV-IIIe to A5p. Along with the difficulties introduced by rapid rotation, the disk itself also interferes with spectral line determination.

In addition to the effects noted above, rapid rotation results in gravity darkening (see Section 1.3.2) effects which impact disk formation mechanisms. In fact, the wind-compressed disk model discussed in Section 1.3.2 failed when gravity darkening effects were added to the model. This was particularly true when the original model was altered to take nonradial line-driving forces into consideration.

Rapid rotation may have interesting evolutionary effects on Be stars. A study by Frémat et al. (2005) asserted that rapid rotators evolve at slower rates than comparable stars of the same mass that are more slowly rotating. Frémat et al. (2005) found that apparent effective temperature decreases as $V_e \sin i$ increases due to a levitation effect on the stellar material. Another study (Meynet, 1999) suggests that rapid rotation alters the evolutionary tracks of massive stars by shifting them toward brighter and redder regions on the HR diagram. The effects of rapid rotation on stellar evolution remains remain poorly understood and at times controversial, and research in this area is ongoing.

1.2.3 Classical Be Stars

Classical Be stars include Be stars and Be shell stars. The types are distinguished by the shapes of their spectral lines. Although the disks responsible for the Be phenomenon will be discussed more extensively in Section 1.3, it is useful to describe how the orientation of the disks explains the differences in emission line shapes seen in the different types of Be stars.

The disks of Be shell stars are presumably viewed edge-on ($i = 90°$) and their spectral lines display narrow central depressions, which extend below the continuum. Disk systems viewed at arbitrary angles are, not surprisingly, more commonly observed and thus comprise the majority of Be stars. The spectra associated with these stars can also possess central depressions, although they do not typically extend below the continuum.

These cases are schematically represented in Figure 1.1 (adapted from Slettebak (1979)). As described in Section 1.2.2, Be stars are rapid rotators. Rapid rotation is associated with Doppler broadening, in which spectral lines widen as the rotational speed of their source increases. The four lines shown in Figure 1.1 would result in different measurements of $V_e \sin i$. In the pole-on case, $V_e \sin i$ would be at a minimum, and the line does not undergo broadening. The next two examples are seen from intermediate angles of inclination. These lines are associated with larger $V_e \sin i$ and are broadened. The doubly peaked line profile is also associated with increasing i. Finally, in the edge on case $V_e \sin i$ is at a maximum and the line is maximally broadened and the doubly peaked structure is at its most pronounced. The central absorption feature is evident in this case, and results from geometric effects.

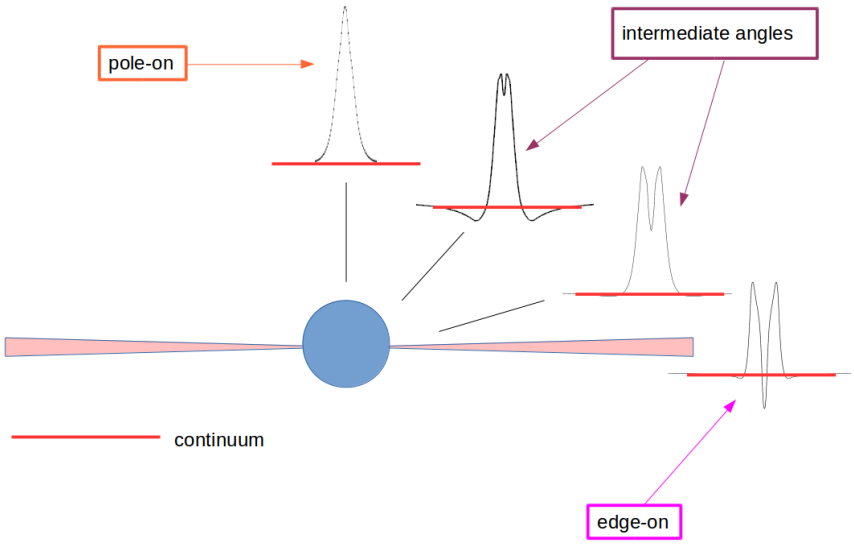

Figure 1.1: A schematic of spectral lines observed as a circumstellar disk is viewed from different angles. Pole-on viewing is associated with strong, narrow emission lines; as the viewing angle increases to more intermediate angles the line widens and broadens. Partial absorption of the emitted light occurs due to the presence of circumstellar material. Viewed with the disk edge-on, the emission line has two clear peaks along with a central trough which dips below the continuum level. In this case the trough is attributable to absorption as well as attenuation due to the disk geometry. Figure is adapted from Slettebak (1979).

1.2.4 Variability

Variability is commonly observed in stars which display the Be phenomenon, and is observed over a variety of timescales. In general, long-term variability in Be stars occurs over periods of years as disks grow and dissipate. Changes seen observationally may be profound. Of course, exceptions do exist in regard to this long-term variability; some disk systems have been observed to remain stable over multiple decades. Perhaps the best example of this is the star 1 Delphini. Observations of 1 Del and its disk are consistent with those of a disk that has not changed considerably over an approximately forty year span (Haubois et al., 2012).

Intermediate-term variability occurs on timescales of a few years. One phenomenon commonly associated with intermediate-term visibility is the one-armed density oscillation, seen for example in the disk of ζ Tauri. The inhomogeneity produces changes in the relative strengths of the short (violet) and long (red) wavelength peaks in the emission line; this is referred to as the violet/red or V/R ratio. McDavid et al. (2000) successfully modelled the relationship between V/R and changes in polarization using a one-armed density wave. The wave is represented visually in Figure 1.2. Another analysis (Wisniewski et al., 2007) probed the disk of ζ Tau spectroscopically. They found that the Hα lines were oriented opposite to other emission lines (such as H I and Fe II), lending support to the one-armed oscillation pro-

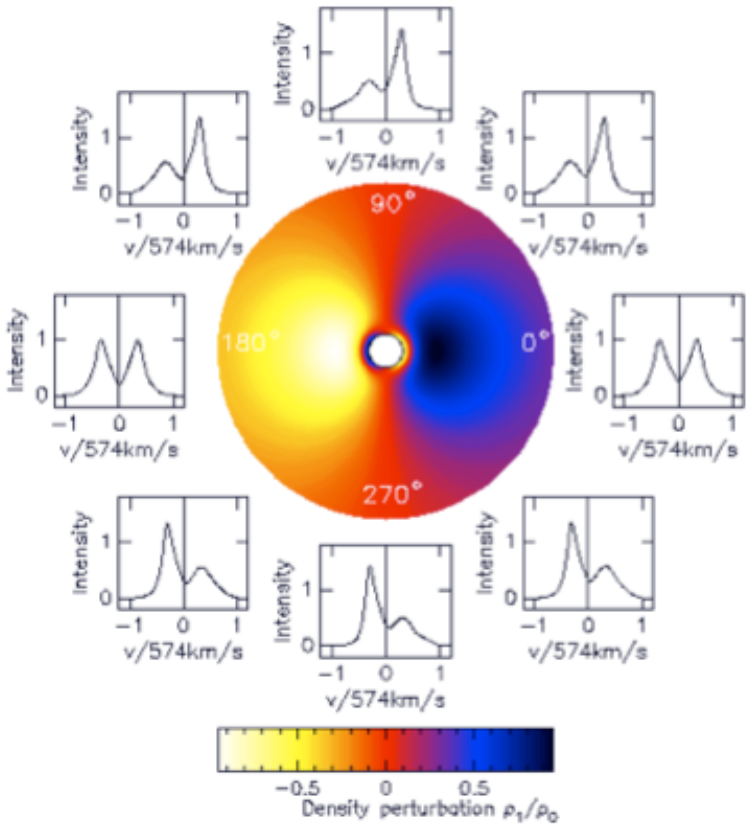

Figure 1.2: Representation of one-armed density wave in the disk of ζ Tauri. As the density enhancement travels within the disk, the relative strengths of the long and short wavelength peaks (the violet-to-red or V/R ratio) changes accordingly. The enhancement is associated with a stronger red peak; stronger flux in the blue relates to decreased disk density. This figure is a reproduction of Figure 2 in "A Connection Between V/R and Polarization in Be Stars", McDavid, D.; Bjorkman, K. S.; Bjorkman, J. E.; Okazaki, A. T. 2000, The Be Phenomenon in Early-Type Stars, IAU Colloquium 175, ASP Conference Proceedings, Vol. 214, edited by Myron A. Smith and Huib F. Henrichs. Astronomical Society of the Pacific, ISBN 1-58381-045-5, 2000, p.460. © ASP, used with permission.

posed by McDavid et al. (2000). Figure 1.3 is a schematic of the disk; the region of reduced density is indicated by the darker shading; the lighter shading corresponds to a density enhancement. The Hα and H I lines are included in order to show the regions of the disk from which they emerge. It can be seen clearly along the line of sight that the spiral structure of the density oscillation causes a combined Doppler shift effect. In other words, if we look for example at the density enhancement, the portion in the inner part of the disk that is associated with the H I line is approaching and is thus blueshifted, making the short-wavelength (violet, V) peak stronger. Contemporaneously the outer portion of the density enhancement, which is associated with Hα, is receding with respect to our line of sight and the longer-wavelength

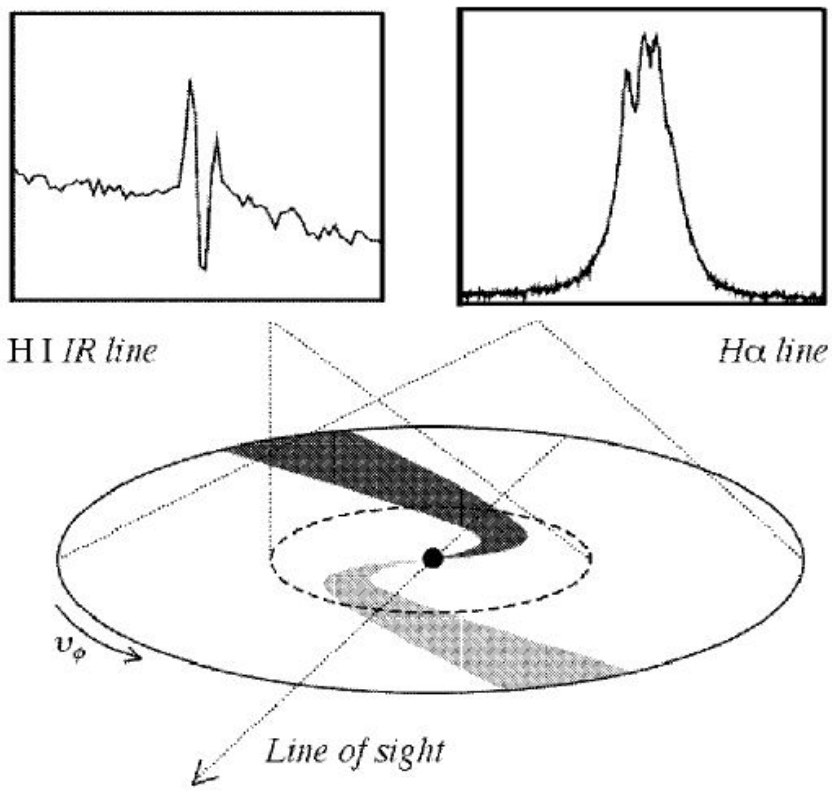

Figure 1.3: Illustration showing the origin of the V/R discrepancy in the disk of ζ Tauri. In this specific case changes can be seen in the profiles of the Hα line emanating from the outer regions of the disk as well as the H I line which forms closer to the photosphere. The timing and degree of variation between the two lines depends on the geometry of the density inhomogeneity. Appeared as Figure 3 in "Toward Mapping the Detailed Density Structure of Classical Be Circumstellar Disks", Wisniewski, J. P.; Kowalski, A. F.; Bjorkman, K. S.; Bjorkman, J. E.; Carciofi, A. C. 2007, The Astrophysical Journal, Volume 656, Issue 1, pp. L21-L24. © AAS and reproduced with permission.

(red, R) peak in the emission line is stronger. This configuration gives rise to the observed V/R fluctuations.

Shorter-term variability has other causes and occurs on a timescale ranging from hours to days (Percy, 1994). Some, such as stellar pulsation, are obviously due to processes within the star itself. Nonradial pulsations (NRPs), known to occur in massive stars, are particularly interesting because they can modify emission line profiles (Kogure and Leung, 2007). As well, NRPs in Be stars can be particularly violent. While such pulsations do not transfer sufficient amounts of mass and angular momentum to be the cause of disk formation, NRPs may nonetheless be adding mass to previously established disks (Rivinius et al., 2002).

Low-grade variability for ψ Per was suggested by the study Jones, Tycner, and Smith (2011). However, a more recent work demonstrates that ψ Per is actually a highly variable star, with the variations occurring on timescales of days (Draper et al., 2014). Our present understand-

ing is that ψ Per serendipitously entered a phase of relative quiescence while the observations for the Jones, Tycner, and Smith (2011) were taken; inactive periods seem to be an aberration for this star. Since the study in Chapter 4 includes observations covering three epochs, fluctuations in the star's output must be carefully considered in order to constrain our models as accurately as possible. Attempts to quantify Be star variability as a function of time via interferometric observation have not appeared in the literature.

1.3 Disks: Characteristics, Formation and Evolution

It has been established that the Be phenomenon is the result of circumstellar disks surrounding B-type stars. These disks are geometrically thin, with opening angles on the order of a few degrees (Quirrenbach et al., 1997). They do not seem to be structurally homogeneous; it has been demonstrated (Millar and Marlborough, 1998) that the temperature and density structures of the disk both radially and in the vertical direction.

Dougherty and Taylor (1992) examined the disk of ψ Persei, at that time the brightest Be star in radio, at 15 GHz using the VLT radio telescope. Their observations clearly showed that the radio-emitting extended structure associated with ψ Per was asymmetric on the sky. Furthermore, their findings implied that the asymmetry was due to the presence of dense plasma around the star, thereby confirming the presence of a circumstellar disk. They noted as well that the disk was observed approximately edge-on at a position angle of 152°, consistent with more recent results in Hα (Delaa et al., 2011). Dougherty & Taylor's results also showed that the radio-bright region of the disk had an extent of approximately 3700 solar radii along its major axis, corresponding to a diameter of about 17 AU. This was the first report of a true image of a Be star disk.

As mentioned by Coté and Waters (1987), in the study of Be stars the IR excess features far more prominently than radio brightness; not all Be stars are radio bright, but all have significant IR output. The extent of the IR-producing region is smaller than the radio-producing region found by Dougherty & Taylor. For a typical Be star, the IR excess comes from disk material surrounding the star. Free-free interactions give rise to the excess IR radiation observed with these stars (Coté and Waters, 1987).

Circumstellar disks are said to be in Keplerian rotation, meaning that material within the disk follows a $v \propto r^{-1/2}$ velocity law. The Keplerian rotation model had been proposed by Hanuschik et al. (1995) and was later confirmed for shell stars by Rivinius et al. (2001). Keplerian rotation has been supported by observational studies, such as Meilland et al. (2007), for more general cases. Keplerian rotation has important implications for understanding the overall kinematics of disks and is key to the viscous decretion disk model described in Section

1.3.3. In fact, a study by Meilland et al. (2007) of the circumstellar environment of α Arae, using the AMBER/VLTI instrument, was the first to detect Keplerian motion. They generated relatively sophisticated kinematic models using the SIMECA code. Their models assumed thin disks and polar enhanced winds, the results of which were reasonably well matched to their observations. However, the results obtained by Meilland et al. (2007) were not definitive because the models were produced from a small number of observations. Later models made by Oudmaijer et al. (2011) confirmed the findings of Meilland et al. (2007). The Oudmaijer et al. (2011) study compared angular momentum-conserving (AMC) and Keplerian models to spectroastrometric measurements of β CMi taken with the VLT. They demonstrated that while both models reproduced the observed Hα profile, only the Keplerian disk model fit the spatial profile of β CMi. Thus, the results of the study by Oudmaijer et al. (2011) confirmed what had been suggested by Meilland et al. (2007).

In the eighty or so years since Struve (1931) proposed that the circumstellar material responsible for the Be star phenomenon is rotationally supported, a series of models have been used to try to explain precisely how the disks arise. These have included a simple rotational model, the bistability mechanism, wind-compressed disk (WCD) models, and the viscous decretion disk (VDD) model that is presently gaining favour. The simple rotational model is described in Section 1.2.3; the latter three are presented below.

1.3.1 Bistability Model

In their study of the luminous blue variable (LBV) P Cygni, Pauldrach and Puls (1990) described a bistable stellar wind configuration. A discontinuity is seen in their calculated wind model, corresponding to the optical depth of the circumstellar material to the Lyman continuum (Pauldrach and Puls, 1990). Not surprisingly, rapid stellar winds are associated with regions that are optically thin.

Lamers and Pauldrach (1991) attempt to explain the Be phenomenon with the bistability mechanism. Their model considered light in the Lyman continuum with wavelength 91.2 nm, and was predicated on the idea that the optical depth would be on the order of 3 somewhere between the equator and pole of the star. Given the dependence of optical depth on latitude, this seemed likely to occur. Once this condition has been met, the bistability model predicts that a rarefied, high-speed, highly ionized stellar wind will emanate from the pole. From the equator there will be a low-speed, dense wind that is not highly ionized. Lamers and Pauldrach (1991) state that the bistability mechanism does not sufficiently explain equatorial mass loss in the Be phenomenon. While initially promising, the bistability model fell out of favour because the optical depth does not fluctuate in a manner consistent with the model.

1.3.2 Wind-Compressed Disk Model

Bjorkman and Cassinelli (1993) proposed the wind-compressed disk (WCD) model, which was at that time a considerable advancement in the study of the Be phenomenon. Essentially, the model proposed that radiatively driven winds followed a series of streamlines emanating away from the stellar surface. The authors state that gravity and radiation pressure play a role in directing the outflow toward the stellar equator, where it collects and forms a dense disk.

While the WCD model was one of the first formulations of a mechanism of disk formation, further research has demonstrated that circumstellar disks are not wind-compressed. Owocki, Cranmer, and Gayley (1998) showed that the addition of gravity darkening (described below), which is highly relevant in a rapidly rotating star, ultimately resulted in the failure of the WCD model. Once gravity darkening was taken into account, the WCD model was shown to produce a region around the stellar equator which was actually depleted of material in direct contrast to the dense disks that are known to exist around Be stars. Although gravity darkening enhances mass loss from the equatorial regions, Owocki, Cranmer, and Gayley (1998) showed that the WCD model predicts that under these conditions the winds will direct material away from the equator radiatively along nonradial lines. This process depletes material around the equator while enhancing it in the polar regions. Thus, a disk cannot form due to wind compression and the WCD model is therefore invalid.

The WCD model suffered from other fundamental shortcomings. Owocki (2006) notes that a star rotating at less than its critical velocity does not impart enough angular momentum to its decreting material to cause it to orbit the star. Material in the inner disk thus reaccretes onto the parent star. Stellar wind removes material from the outer reaches of the disk. These combined processes decrease the density of the disk until it is far too rarefied to produce the Balmer emission lines by which Be stars are identified. Finally, modification of the WCD model to include a global magnetic field can produce valid models (c.f. Cassinelli et al. (2002)). However, such large-scale magnetic fields have not been detected around Be stars (c.f. Wade et al. (2014b), Wade et al. (2014a)).

Gravity darkening was proposed initially by von Zeipel (1924). Be stars, as rapidly rotating masses of plasma, often show significant oblateness. Thus, the speed of a parcel of material at the equator will be higher than that of a parcel found near the poles. In this manner the effective gravity experienced by a sample of stellar material becomes dependent on the latitude at which it is located. Radiation from the faster-moving and cooler material near the equatorial regions is inhibited while the poles appear to brighten. It has been demonstrated that the effective temperature at the poles (T_p) of a rapidly rotating star (Townsend, Owocki, and Howarth, 2004) increases while holding the luminosity of the star constant, as expressed

in Equation 1.2.

$$T_p = \left(\frac{g_p L_*}{\sigma \Sigma_1} \right)^{0.25}. \tag{1.2}$$

In Equation 1.2, Σ_1 is the surface-area weighted gravity of the star, σ is the Stefan-Boltzmann constant, L_* is the stellar luminosity and g_p is the effective gravity at the pole.

1.3.3 Viscous Decretion Disk

A valid model for circumstellar disks needs to account for Keplerian rotation and the slow outflow of material from the inner to outer regions of a geometrically thin disk. It must also fit timescales, understood generally to be on the order of decades, required for the formation and dissipation of the disks. The viscous decretion disk (VDD) model has been the most successful to date at describing the observed behaviours of Be star disks. The VDD model shares similarities with the models used for protostellar disks (Carciofi, 2011) and is based closely on the α-prescription theory (Pringle, 1981; Shakura and Sunyaev, 1973). The fundamental difference, aside from the respective origins of each type of disk, is that material flows inward in protostellar disks while it is the opposite for Be star disks. Carciofi et al. (2012) used photometry and HDUST simulations to estimate the viscosity constant for 28 CMa.

The general summary of the VDD model is as follows: stellar material is ejected from the surface of a Be star and begins to orbit around its equatorial region. The process by which this occurs is at present unknown. Turbulent viscosity within the orbiting material carries it out and away from the stellar surface via transfer of angular momentum, causing the disk to grow and expand. Continual addition of angular momentum to the material at the base of the disk is necessary for the continued development of the disk. If we consider the material within the disk to be infinitesimal elements of fluid, as we add more angular momentum to the disk, these elements will progress outward. This process relies on the radial density gradient of the disk. If the density drop-off with respect to radius is too shallow, sufficient transfer of angular momentum to the fluid surrounding the star will not occur. While the VDD model is the most promising to date, it suffers an important weakness in that it does not explain how material is launched from the star into orbit as part of the disk. Most implementations of the VDD model rely on assumptions for the rate of mass loss from the star.

1.4 Detailed Modelling

Very broadly, hydrodynamic modelling is used to predict the behaviour of a fluid in a particular system. In the investigation of the Be phenomenon, hydrodynamic models are generated to visualize the internal structures of the disk. While such an approach might be consid-

ered "ideal", it tends to be highly computationally intensive. Fortunately, hydrodynamic behaviours can be simulated by means of static models. A series of static models can be generated in such a way that their input parameters are altered to simulate the evolution of a star-plus-disk system, which can then be compared to observations taken over longer timescales. In effect, this is comparable to a single hydrodynamic model. The BEDISK code will be used to compute density and temperature structures as well as details regarding the state of the circumstellar gas. The BERAY code will be used to synthesize images of a star-plus-disk system on the sky for a specific wavelength (see Section 1.5) which can then be compared to observation and adjusted as necessary. The synthesized interferometric image can be used with other codes to forecast visibilities, which can be compared directly with interferometry.

1.4.1 POECKERT AND MARLBOROUGH

Although BEDISK came into use fairly recently, similar treatments were used with much earlier models. Poeckert and Marlborough (1978) generated models of γ Cassiopeiae based on observational work. They assumed that circumstellar material was distributed around the equatorial plane of the star, and that the distribution was axisymmetric. They further assumed that the parent star was spherical and rotating at its critical velocity. The code calculates ionization states and level populations of the ground state as well as 2S and 2P for hydrogen, under the assumption of radiative equilibrium. Their study utilized an effective kinetic temperature of 20,000 K for γ Cas. Four equally spaced points above the equatorial plane comprised the modelling grid.

1.4.2 MILLAR AND MARLBOROUGH

Millar and Marlborough (1998) (hereafter referred to as MM98) improved upon the modelling done by Poeckert and Marlborough (1978). The newer study examined the accuracy of the original model, eliminated an error, and expanded greatly upon the original code. Poeckert and Marlborough (1978) used only collisional transitions with $n = \pm 1$. The code produced by Millar and Marlborough (1998) takes many more transitions into consideration, which results in a more physically accurate description of the thermodynamic behaviour within the circumstellar environment.

The modelling procedures used by MM98 differed from those of Poeckert and Marlborough (1978) in a number of important ways. The sampling grid for the newer model was larger and more sophisticated. As opposed to Poeckert & Marlborough's small grid, MM98 utilized twenty points throughout the disk, which were chosen to correspond to exponential decreases in density.

Millar and Marlborough (1998) used a fundamentally different approach for calculating disk temperature. While Poeckert and Marlborough (1978) relied on an isothermal disk, Millar and Marlborough (1998) computed a self-consistent temperature distribution within the disk (see Figure 1.4). This different approach means the state of the gas, including the level population and ionization fraction, is determined self-consistently. This is critical for the accurate interpretation of observations.

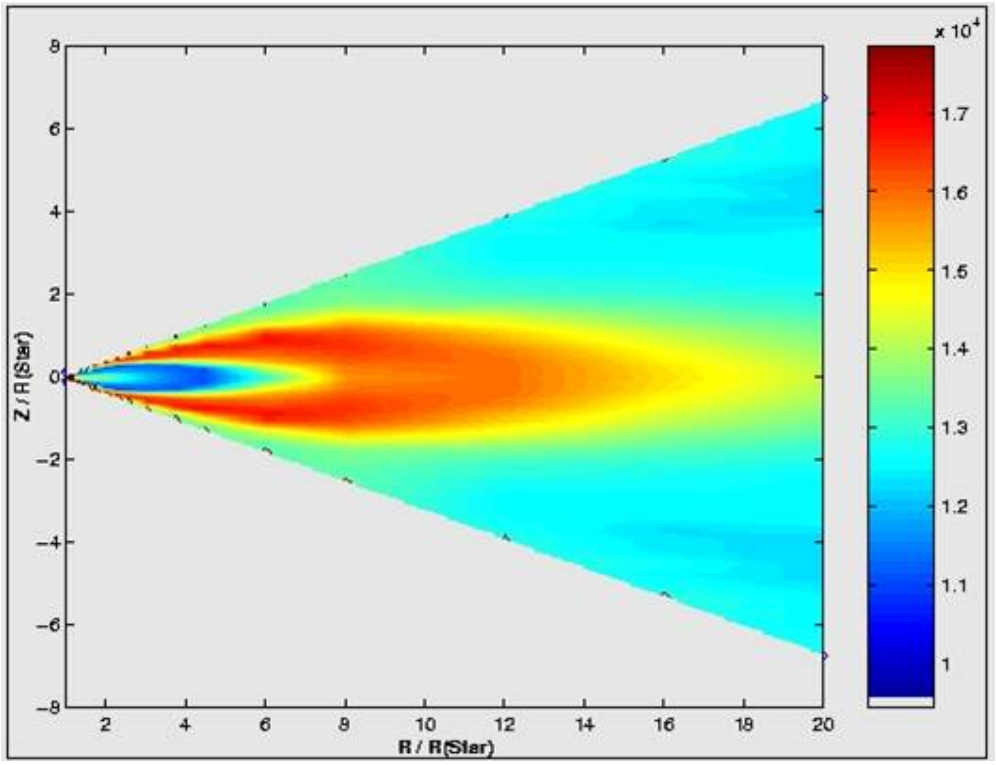

Figure 1.4: Temperature distribution within the disk of γ Cassiopeiae as calculated by Millar and Marlborough (1998).

It should be noted that the cool region near the stellar surface in Figure 1.4 (located between about $R/R_* = 0$ and $R/R_* = 5$) was particularly interesting. Intuitively, one would expect that this region would be the hottest portion of the disk. Other studies (for example, Carciofi and Bjorkman (2008), utilizing the HDUST code) have consistently replicated this finding. The cooler region nearest the star is a result of the high concentration of circumstellar material there. The high density corresponds to a greater optical depth, and thus the radiation from the star is less efficient at heating up that portion of the disk.

1.4.3 Bedisk and Beray

Bedisk is a non-local thermodynamic equilibrium (LTE) code developed by Sigut and Jones (2007), which is typically used with a power-law,

$$\rho(R, Z) = \rho_\circ \left(\frac{R_*}{R}\right)^n \exp\left[\left(-\frac{Z}{H}\right)^2\right] \tag{1.3}$$

to compute the density structure of circumstellar disks, such as that in Figure 1.5. As one

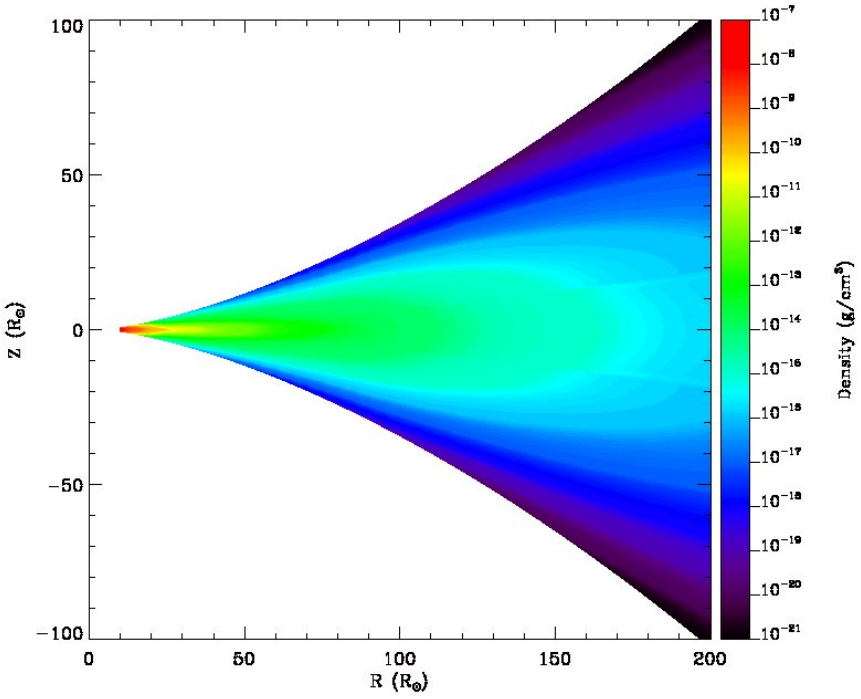

Figure 1.5: Density structure of γ Cassiopeiae computed with Bedisk (Grzenia, 2009).

might expect, $\rho(R, Z)$ is a computed density, and $\rho_\circ$ is the density of the disk in the region nearest the star (i.e., the base density). R_* and R are the stellar radius and horizontal distance from the star, respectively; Z is the distance above the midplane of the disk while H is the scale height. While power-law description is used throughout this work, the code can utilize other density distributions. The computational grid is a function of R, and a set number of steps in the Z direction perpendicular to the disk. The density distribution in the Z direction is approximately hydrostatic. Mirror symmetry of the disk in the vertical direction is assumed.

Bedisk also has the capability to account for the thermodynamic conditions in a disk with

solar metallicity rather than one composed purely of H and He. While the effects of metallicity are not always large, this is useful for making a more complete model because the cooling effects of metallicity are considered. Metals are important because the numerous low energy levels in a metal atom are readily excited. As the atoms deecxite, energy in the form of a photon is released, resulting in an overall cooling effect. Iron, in particular, makes a significant contribution and is part of the model. As our models become more realistic by describing the ionization states and level populations of the species within the disks, they will agree better with observations of real stars thereby allowing us a better understanding of the properties of the circumstellar environment.

BERAY is a related radiative transfer code. Sigut (2011) states that BERAY takes temperature and density structures output by BEDISK and solves the radiative transfer equation along approximately 10^5 rays spread throughout the disk. The solutions are used to make a variety of predictions, including the equivalent widths of metal lines, unresolved spectra, and images on the sky (Sigut, 2011).

1.4.4 2DDFT

The final code, 2-dimensional Discrete Fourier Transform or 2DDFT was developed to allow models made in BEDISK and BERAY to be compared directly to interferometric observed visibilities. Output from BERAY includes a real-space image of a disk system extended structure that fits the (n, ρ_o, i) specified by the user. 2DDFT transforms the model image into Fourier space, rendering a set of theoretical interferometric visibilities (expressed as the squared visibility or V^2, which are the normalized Fourier powers for each observations) with respect to spatial frequency which can then be compared directly to the interferometric observable. The code also accounts for the distance to the target star.

1.5 INTERFEROMETRY

Be star disks pose a series of observational challenges that are difficult or impossible to meet with standard telescopes. Most troublesome is the necessity of high angular resolution (AR), which is proportional to the aperture of a standard telescope. AR can be improved significantly by taking interferometric observations. Signals from smaller telescopes can be separated by a known distance and combined to form interference fringes, which are essentially observations of the star made in Fourier space. By Fourier transforming the interference fringes, it is possible to characterize the disk surrounding a Be star. Generally speaking, the angular resolution available to an interferometric observer is equivalent to that which could be obtained from a telescope with an aperture the same size as the interferometer's baseline.

1.5.1 Overview, History, and Current Facilities

Michelson's interferometer was pivotal to our understanding of the propagation of electromagnetic (EM) radiation. His device piqued the interest of some observers, particularly in France, who saw its potential as an astronomical instrument (Lawson, 2000). However, given the level of precision and the technical challenges involved with astronomical interferometry, after some initial progress interest in the interferometer waned for several decades. Modern interferometric techniques can be traced back to the development of radio astronomy, which was more readily developed as a result of the much longer EM wavelengths it utilizes.

Optical interferometry, defined commonly as using EM radiation in the visible and near-infrared wavelengths, did not begin to develop in earnest until the early 21st century. While the principles are similar, optical interferometry is a greater technical challenge due to the shorter wavelengths involved. First, the instrument itself must be built to a far higher precision than what is required of radio. Tolerances on the order of nanometres are required, even with baselines spanning hundreds of metres. Another difficulty arises from the atmosphere. Fluctuations within the atmosphere (due, for example, to thermal effects) have a more significant effect on optical wavelengths and can make interferometry impossible under some conditions. A third technical challenge involves the requirement that the beamlines be evacuated. Dispersion effects due to the presence of air in the beam pipes can degrade the signals from each telescope, quite possibly rendering the information useless. Unlike radio interferometry, which allows observers to record their observations for later analysis provided they are accurately timestamped, with optical interferometry observations must instead be dealt with in real time. Oudmaijer et al. (2012) give an overview of the current state of optical interferometry. They note that in addition to Be stars, interferometry has been used to characterize faint active galactic nuclei as well as to observe massive protostellar objects which would ordinarily be obscured. More relevant to this work, however, are studies of Be disk kinematics and observations of stellar surfaces. The authors point out that spatial and spectral resolution of Be stars, combined with appropriate models, have allowed astronomers to conclude that Be star disks undergo Keplerian rotation, thereby solving a key piece of the puzzle surrounding the Be star phenomenon. As well, surface studies have shown that rapidly rotating stars tend to exhibit oblateness, as one might expect. The related phenomenon of gravity darkening, described previously, can also be seen.

Because interferometric observation is vital to the study of Be stars, it will be used to verify and further constrain our numerical models. Candidate instruments for obtaining the necessary data are the Navy Precision Optical Interferometer (NPOI) and Very Large Telescope Interferometer (VLTI). Both instruments operate in the visible wavelength regime and their

individual capabilities are described in Section 1.5.1.1 and Section 1.5.1.2, below.

1.5.1.1 NPOI

Seen in Figure 1.6, the Navy Precision Optical Interferometer (NPOI, formerly the Navy Prototype Optical Interferometer) is situated on Anderson Mesa near Flagstaff, Arizona and is a collaborative effort among the United States Naval Observatory, the Naval Research Laboratory, and Lowell Observatory. NPOI began operations in the late 1990s, imaging a binary star and limb darkening in 1996 and 1997, respectively. Armstrong et al. (1998) provides a very thorough description of NPOI, portions of which are summarized throughout this section. The design of NPOI was based on that of the Mark III interferometer, which operated at Mt.

Figure 1.6: Aerial view of NPOI. Image from http://usic.wikispaces.com/Navy+Prototype+Optical+Interferometer+(NPOI) and licensed under a Creative Commons Attribution Share-Alike 3.0 license.

Wilson during the 1980s. It was designed with the goals of high-precision astrometry and the ability to image stars brighter than approximately magnitude 8. It was built with ten 50 cm siderostats arranged in an imaging array (with six elements) and astrometric subarray (with four elements). The siderostats feed 12 cm apertures which lead to the optics processing facility. The astrometric subarray is fixed, whereas the elements comprising the imaging array can be rearranged. Baselines range from 2.0 m in the astrometric array to a maximum of 437 m for imaging. Per Armstrong et al. (1998), observations at NPOI are made in a wavelength regime spanning 450 to 850 nm. This is well-suited to the study of Be stars in Hα.

1.5.1.2 VLTI

The Very Large Telescope Interferometer (VLTI), located near Paranal, Chile, in the Atacama Desert, is operated by the European Southern Observatory (ESO). The VLT (seen in Figure 1.7) consists of a total of eight telescopes. Four are 8.2 m in diameter and are equipped with adaptive optics systems. While they are typically run independently for other modes of observation, these large telescopes can be combined to form a powerful interferometer. In addition, there are another four telescopes with 1.8 m apertures which are dedicated for interferometric use. Like NPOI, VLTI is intended for both imaging and astrometry (Labeyrie, Lipson, and Nisenson, 2006). The longest baselines at VLTI are about half the length of

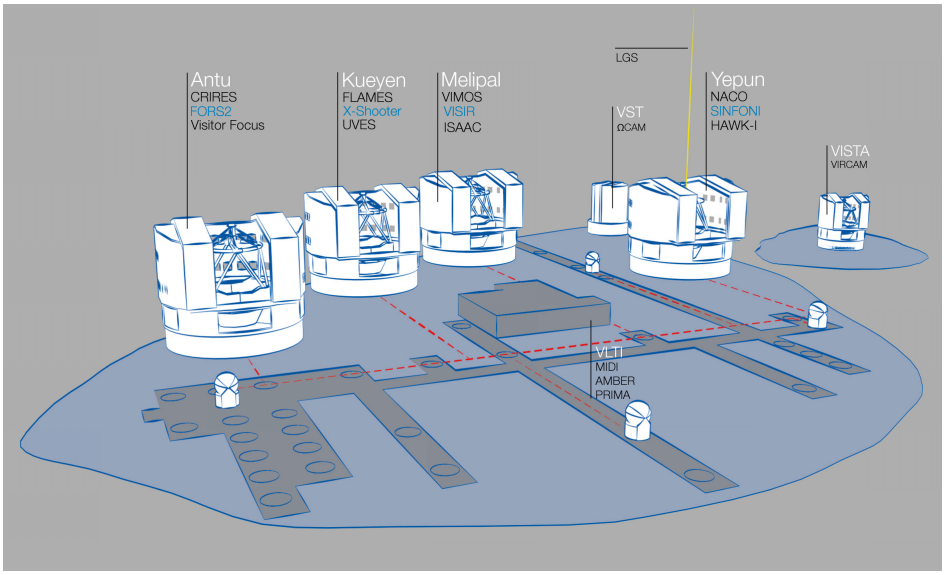

Figure 1.7: Diagram of the VLT array. The small 1.8 m telescopes are dedicated interferometric elements. The larger telescopes are used for other purposes but can be moved as indicated by the red dashed lines in various configurations as an interferometer. Image from European Southern Observatory (© ESO) under the Creative Commons Attribution 4.0 International License.

those at NPOI, at 202 m. Unlike NPOI, however, the apertures at VLTI are significantly larger and the facility can observe in a much broader range of wavelengths: the entire visible spectrum, near ultraviolet, and infrared to 25 μm (Labeyrie, Lipson, and Nisenson, 2006). This vast range of wavelengths includes not only the Hα line, but a several of the other hydrogen Balmer emission lines as well, which would be useful for determining the sizes of the regions that emit them. VLTI is potentially an exceptionally useful tool for investigating the Be phenomenon.

1.5.1.3 CHARA

A number of other optical interferometers are in operation around the world. The Center for High Angular Resolution Astronomy (CHARA) interferometer, located at the Mount Wilson Observatory in southern California, is an instrument comparable to NPOI and VLTI. It is comprised of six 1-metre telescopes on a Y-shaped configuration, allowing for baselines between 30 and 330 m. CHARA is an optical and near-IR instrument which observes wavelengths in the V and K bands specifically. The interested reader is directed to ten Brummelaar et al. (2005), which describes CHARA in considerably more detail than what has been provided here.

1.5.2 Long Baseline Interferometry

The observational approach to be taken in the course of this study of Be stars is known as long baseline interferometry, although for brevity and in keeping with common usage it will be referred to simply as interferometry. Labeyrie, Lipson, and Nisenson (2006) present a very thorough development of the physical and historical aspects of interferometry; the interested reader is directed to this source for the more specific and specialized details. Star-plus-disk systems will be studied in the so-called optical regime.

At its simplest an interferometer can be represented by a pair of telescopes (or other apertures, such as siderostats) separated by a distance referred to as the baseline length, as exemplified in the schematic shown in Figure 1.8. Starlight arrives at the interferometer as a series of plane-parallel wavefronts (although subject to atmospheric perturbations). If these wavefronts are not arriving exactly parallel to the baseline, they will have to travel an additional distance after encountering the first aperture before reaching the second. The interferometer is set up to compensate for this difference in path length. If we consider the baseline to be a vector extending from one aperture to the other, the length of the delay line needed to achieve zero path-length difference will be equal to the scalar product of the baseline vector and a unit vector pointing from the baseline to the direction of the star. This length is added to the beam path between the first telescope and the beam combiner.

After adjusting the optics to achieve zero path-length difference, the beams are combined, allowing them to produce interference fringes. The characteristics of these interference fringes provide information via Fourier analysis about the extended structure of the source. A quantitative description of this process has been provided in Section 1.5.3. In this manner observers have been able to deduce the non-point source structure of Be star-plus-disk systems.

While the relative simplicity of an interferometer with two telescopes is useful for explaining generally how such an instrument works, in reality we are not limited to the use of only

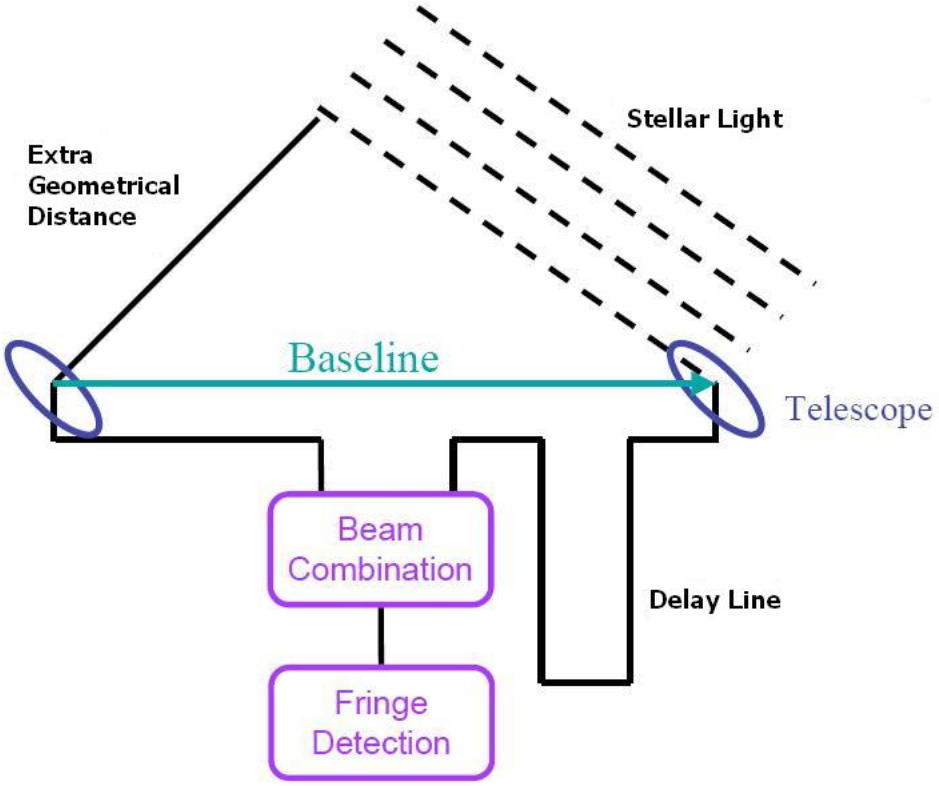

Figure 1.8: Schematic diagram of an interferometer. Image courtesy C. Tycner.

two telescopes. A number of interferometers, such as NPOI, combine signal from two to more than ten apertures simultaneously.

The distance by which two telescopes in an interferometer are separated relates directly to the resolution that can be obtained. In other words, the interferometer has an angular resolution that would be equivalent to that obtained by a standard telescope with a diameter equal to the baseline distance. The enhanced angular resolution comes at a steep price, however; only those portions of the source which are parallel to the projected baseline can be resolved. A more complete picture is obtained by allowing the projected baseline to change as the Earth rotates, or to increase the number of baselines utilized. In either case observers can combine the information from the different baseline projections to get a more complete picture of the target's behaviour. Thus, imaging on multiple baselines contemporaneously is clearly advantageous over observing on single baselines.

As was mentioned previously, variability of Be stars can occur over very short timescales. Obtaining a "snapshot" of a star at a given time makes it possible to discern the variability and its effect more specifically rather than seeing the effect averaged out, as is the case with

other observational methodologies. With multiple simultaneous observations, one can also take advantage of the fact that the atmospheric conditions are the same.

1.5.3 Theoretical Description of Interferometry

As stated previously, one of the strengths of interferometry is its high angular resolution. Labeyrie, Lipson, and Nisenson (2006) state that interferometric resolution can be in excess of atmospheric seeing. This is certainly the case if the desired angular resolution is simply what is enough to resolve a target sufficiently.

Using the "classical" resolution formula, where $R = 1.22\,(\lambda/D)$, for a typical observation at 656 nm (λ) with a 100 m (D) baseline, we have a limiting resolution of 1.7 mas. This corresponds to the first minimum of a diffraction pattern. However, objects with a smaller angular size than this are nonetheless resolved to an extent adequate to measure the sizes of their disks even if the exact features are not perfectly resolved. In this way, the already superior angular resolution of the interferometer is extended.

It must be emphasized that interferometry depends on the Fourier transform (FT). In the cases that follow, the fitting functions of the V^2 versus spatial frequency plots represent the extended sources on the sky in Fourier space. The intricacies of the FT are described well in Thompson, Moran, and Swenson (1986). For an extensive treatment, the reader is directed to Bracewell (2000).

The primary observable in amplitude interferometry is the visibility. In its simplest form, it is expressed as

$$V = \frac{I_{max} - I_{min}}{I_{max} + I_{min}}, \tag{1.4}$$

where I_{max} and I_{min} correspond respectively to the maximum and minimum intensities of the fringes. Equation 1.4 was used to describe the output of Michelson's original interferometer (Labeyrie, Lipson, and Nisenson, 2006). Modern interferometry relies on detailed knowledge of the instrument's characteristics as well as the FT.

In practice, observers typically use the squared visibility,

$$V^2(u,v) = \left| \int \mathcal{A}(\alpha,\beta) F(\alpha,\beta) \exp[-2\pi i(\alpha u + \beta v)] d\alpha d\beta \right|^2 \tag{1.5}$$

which is a function of the source structure (described by angles α and β), aperture efficiency $\mathcal{A}(\alpha,\beta)$, and spatial frequency of the baseline. $F(\alpha,\beta)$ has units of power per solid angle (Grzenia, 2009; Lawson, 2000). Equation 1.5 is derived from the interaction of EM waves interacting with two apertures. Here, the quantities u and v are spatial frequency terms, which

are detailed below in Equations 1.13 and 1.14.

Following the derivation in Lawson (2000), if we consider an idealized interferometer with a pair of identical apertures separated by a distance $\vec{B} = \vec{x_2} - \vec{x_1}$ (where $\vec{x_1}$ and $\vec{x_2}$ are the positions of the first and second apertures), we can express the EM waves at each aperture as

$$\begin{aligned} \phi_1 &\propto e^{i\vec{k}\cdot\vec{x_1}} e^{-i\omega t} \\ &\propto e^{-ik\hat{s}\cdot\vec{x_1}} e^{-i\omega t} \end{aligned} \tag{1.6}$$

and

$$\begin{aligned} \phi_2 &\propto e^{i\vec{k}\cdot\vec{x_2}} e^{-i\omega t} \\ &\propto e^{-ik\hat{s}\cdot\vec{x_1}} e^{-ik\hat{s}\cdot\vec{B}} e^{-i\omega t} \end{aligned} \tag{1.7}$$

Eliminating the common term, we can now express the waves as

$$\phi_1 \propto e^{-i\omega t}, \text{ and} \tag{1.8}$$

$$\phi_2 \propto e^{-ik\hat{s}\cdot\vec{B}} e^{-i\omega t}. \tag{1.9}$$

In this set of equations, $\vec{B}$ is the baseline vector running from the position of aperture 1 to aperture 2, $\vec{k}$ is the wavevector as defined in Jackson (1975), and $\hat{s}$ is a unit vector originating at the midpoint of $\vec{B}$ and pointing at the source.

We find a time-averaged detected power, P, from the direct sum of the waves at the two apertures:

$$\phi_{net} = \phi_1 + \phi_2, \text{ and} \tag{1.10}$$

$$P \propto \phi_{net}^{*} \phi_{net}. \tag{1.11}$$

It is this last quantity, P, that is related to the source visibility. It can be rewritten in terms of the aperture and power per solid angle as

$$P = \int d\Omega \mathcal{A}(\alpha, \beta) F(\alpha, \beta) \tag{1.12}$$

The expression in Equation 1.5 is integrated over a solid angle to obtain a more compact expression for the power. We note that the integrand in Equation 1.12 is the same as that in Equation 1.5, but lacking phase information.

The spatial frequency terms u and v in Equation 1.5 are related to the x and y components of the baseline vector $\vec{B}$. Spatial frequency is merely baseline length expressed in terms of the

wavelength over which observations are made and is used to describe the coordinates of the observation in Fourier space. Thus,

$$u = \frac{B_x}{\lambda} \text{ and} \tag{1.13}$$

$$v = \frac{B_y}{\lambda}, \tag{1.14}$$

where λ represents wavelength. As before, this derivation closely follows Lawson (2000) and the interested reader can find the full treatment in chapter 2 of that work.

Although no object on the sky is a true point source, in some cases it is either impossible or unnecessary to make the distinction. In the case of interferometric observation, those targets which cannot be distinguished from a point source have $V^2 = 1$. If we examine the equation for the visibility in this case,

$$V(u, v) = e^{-2\pi i(\alpha u + \beta v)}, \tag{1.15}$$

it is readily apparent that $|V(u, v)|^2 = 1$. Lawson (2000) goes on further to point out that this equation describes only the phase of the observation and contains no further information about the source.

A simple case of an object with an extended structure, and thus visibilities which will deviate from unity, is that of the uniform disk (UD). In the case of a Be star-plus-disk system, the UD attempts only to make a first-order estimate of the angular extent on the sky of the object. It is a simple geometrical model, assuming a uniformly illuminated circular patch on the sky, and it does not account for the disparate contributions from the star and its disk (Grzenia, 2009).

The UD is described by a first-order Bessel function of the first kind (Lawson, 2000),

$$V^2_{UD} = \left(\frac{2J_1\left(\pi\theta\sqrt{u^2 + v^2}\right)}{\pi\theta\sqrt{u^2 + v^2}} \right)^2. \tag{1.16}$$

In Equation 1.16, u and v are the coordinates of each observation as explained previously and θ is the diameter of the UD which is being fit to the observations.

An idealized V^2 versus fringe spacing plot of a UD can be seen in Figure 1.9.

An example of real observational visibilities can be seen in Figure 1.10. The points shown in the figure correspond to observations of 48 Persei made at NPOI. Each baseline is represented by a different colour. Note that the majority of data points fall within an "envelope" indicated by the two dotted lines, which will be explained in detail in Chapter 3. The plot shows clearly that 48 Per deviates from a point source. As expected, V^2 has an overall downward trend

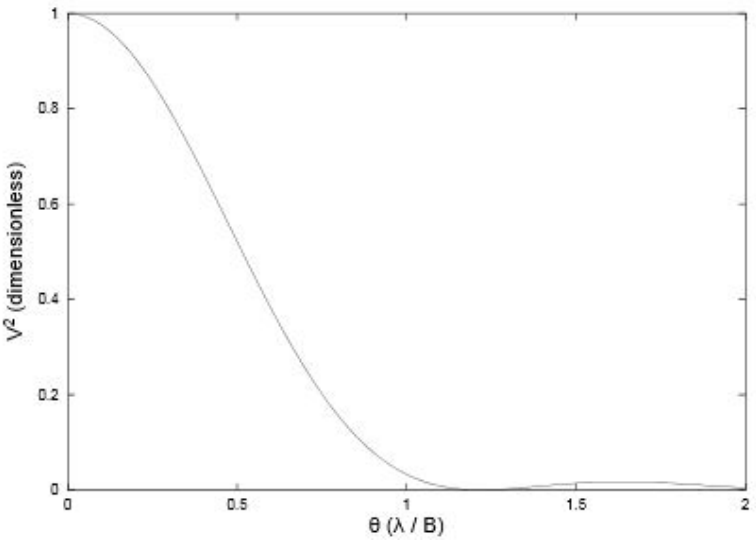

Figure 1.9: Plot of squared visibility versus spatial frequency of an ideal uniform disk (Lawson (2000), JPL Publication 00-009 07/00).

as the spatial frequency increases. It is also readily apparent that the target does not fit the model of a point source, in which V^2 does not deviate from a value of 1.0 as indicated by the dashed line. Elliptical Gaussian fits are represented by the dotted lines in Figure 1.10. These geometrical models are a means of describing the shape of the target on the sky. While in some ways it is a rudimentary, first-order analysis, it is nonetheless a reasonable starting point for characterizing the star and its disk. The upper line corresponds to the minor axis of the fit, while the lower line corresponds to the major axis. In an ideal case, the squared visibilities of all observations will fall within the area demarcated by the two dotted lines, which some points falling precisely on either the upper or lower curve in the event that the baseline is aligned exactly with an axis. To within errors, this is largely the case in Figure 1.10. The solid black lines are unique to each baseline and are related to the change in the projected orientation of the baseline throughout the observing period. While the baseline obviously remains fixed with respect to the Earth as the observations are being taken, Earth's rotation causes the projection of the baseline on the sky to move throughout the night. Over the course of a few hours' observations, this causes the baseline to change its orientation with respect to the source, and in effect samples its shape.

Figure 1.11 is the (u, v) plane for observations of the Be star 48 Persei taken at the NPOI (Tycner, 2013). The (u, v) plane is a means of expressing the coordinates of the elements of an interferometer and can be used to judge the level of sky coverage for a particular target. The coordinates (u, v) relate to the spatial coordinates of the interferometric elements in the

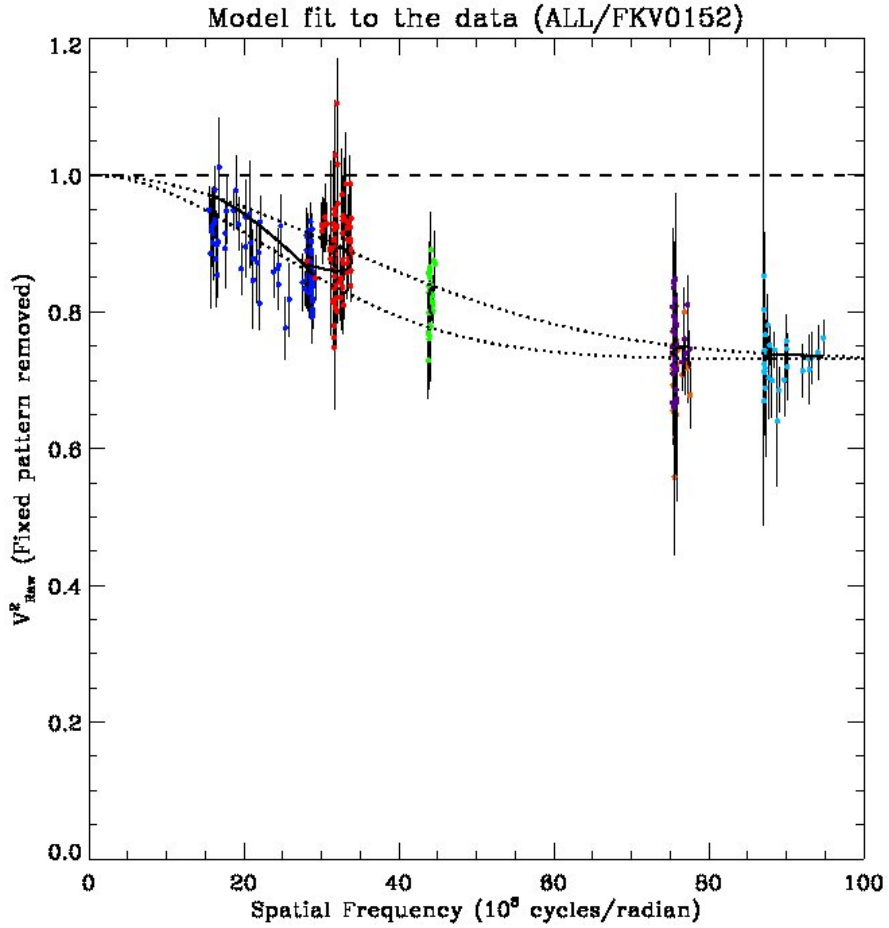

Figure 1.10: Squared visibility versus spatial frequency plot of observations of 48 Persei taken at NPOI (Tycner, 2013).

(X, Y, Z) space. A full derivation is shown in Chapter 4 of Thompson, Moran, and Swenson (1986); for purposes of this work, the relationship between the two is as follows:

$$\begin{aligned} u &= X_\lambda \sin H + Y_\lambda \cos H \\ v &= -X_\lambda \sin\delta \cos H + Y_\lambda \sin\delta \sin H + Z_\lambda \cos\delta \\ w &= X_\lambda \cos\delta \cos H - Y_\lambda \cos\delta \sin H + Z_\lambda \sin\delta. \end{aligned} \tag{1.17}$$

In this notation, $(X_\lambda, Y_\lambda, Z_\lambda)$ are the components of the baseline in (X, Y, Z) space; δ and H are the respective declination and hour angle of the target. X is defined with respect to the astronomical meridian and Y with due east while Z is placed at the celestial pole. It is rather apparent at this point the ostensibly two-dimensional (u, v) plane is actually a three-dimensional space, however in practice the w coordinate is typically eliminated (Thompson, Moran, and Swenson, 1986).

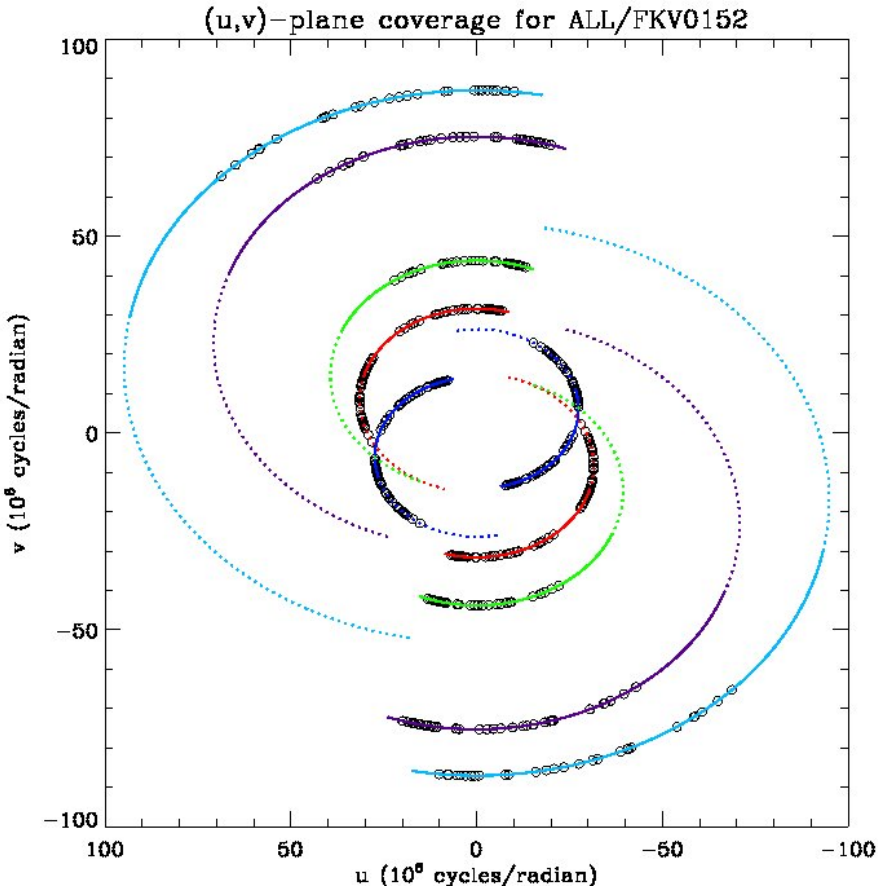

Figure 1.11: Plot of the (u, v) plane for NPOI observations of 48 Per (Tycner, 2013). Actual observations are indicated by open circles; the solid coloured arcs indicate coverage that may have been obtained from the meridian to hour angle =+6 (6 h west). The dotted portions correspond to possible coverage from the meridian to HA=-6 (6 h east).

Continuing to follow the derivation in Thompson, Moran, and Swenson (1986), we can rearrange the expressions in Equation 1.17 to obtain an equation for an ellipse,

$$u^2 + \left(\frac{v - Z_\lambda \cos \delta_\circ}{\sin \delta_\circ} \right)^2 = X_\lambda^2 + Y_\lambda^2, \tag{1.18}$$

where the declination has been set to a reference position*. The result is that the arcs traced out on the (u, v) plane have a semimajor axis equal to $\sqrt{X_\lambda^2 + Y_\lambda^2}$, and the centre of the ellipse is located on the v axis, displaced from the origin by $Z_\lambda \cos \delta_\circ$. The ellipses in Figure 1.11 are consistent with this result. The variations in the arcs follow from Equation 1.18 and

*Thompson, Moran, and Swenson (1986) state that the form of Equation 1.18 is a result of setting the hour angle and declination to $(H_\circ, \delta_\circ)$, the phase reference position. The phase reference position is defined in terms of (u, v, w) space with respect to north and is described in detail in Thompson, Moran, and Swenson (1986).

demonstrate that observing from different baselines at various times and for various integration times necessarily results in differing sky coverages.

It should also be apparent that the arcs in the (u, v) plane seem to be mirror images of one another. Note that squaring the X_λ and Y_λ terms removes information about whether the coordinates are positive or negative numbers. The resulting ambiguity cannot be resolved and therefore the mirrored arcs are considered equally valid.

1.6 Research Program

Verification of computational models by experimentation and observation is vital to the advancement of knowledge. In the specific case of Be stars, detailed models may be paired with observations of actual stars to enhance the descriptive abilities of the models. For this study a number of modelling techniques are available to complement the interferometric and spectroscopic data obtained observationally.

1.6.1 Observation Program

Although interferometry is the focus of this work, it has not been the sole source of information about Be stars and other methodologies continue to add to our knowledge of the phenomenon. Spectroscopy and polarimetry yielded results that were indicative of disks long before the high resolution of interferometry allowed for their detection.

Spectroscopy was key to the initial characterization of Be stars and remains useful for discerning the "average" features of the star-plus-disk system. Perhaps the most useful example is that of Doppler broadening. The width of spectral lines is related to the rotational speed of the disk; those disks that rotate fastest produce the broadest lines (see Figure 1.12). Other aspects of the lineshape describe the inclination angle and any asymmetry present in the disk. For example, those disks that are viewed edge on tend to be associated with doubly peaked spectral lines showing a strong absorption feature (although this is not a strict rule; Silaj et al. (2010) show that changes in the disk density and corresponding temperature distribution can alter the spectral lines such that they appear to indicate changes in inclination angle of the disk).

Light from Be stars was observed to be linearly polarized, a finding that helped lead to the understanding that the Be phenomenon is related to the presence of a disk. Thomson scattering of electrons within the circumstellar environment produces linearly polarized light (Halonen and Jones, 2013). The fact that this polarization is detected points to a disk-shaped distribution of material. As it is emitted, starlight is unpolarized; interaction with the circumstellar material linearly polarizes the light. A small net polarization is detected as a result

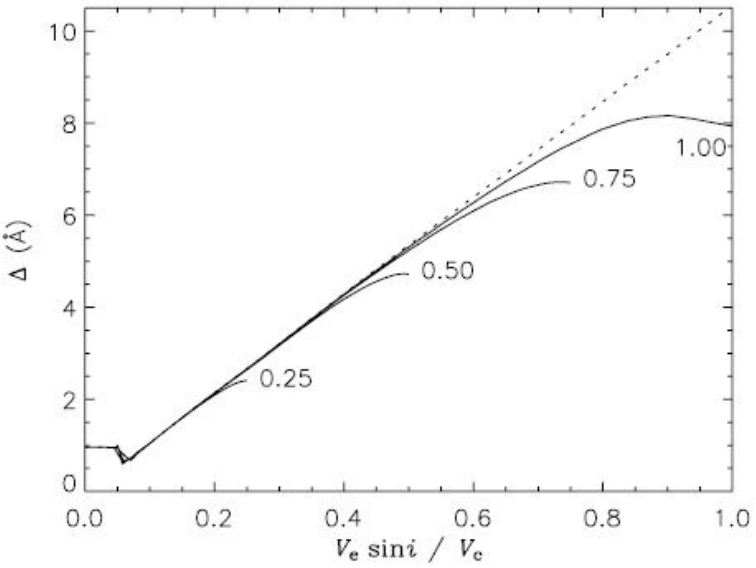

Figure 1.12: Graph from Townsend, Owocki, and Howarth (2004) showing the relationship between Doppler broadening (in Å) and projected rotational velocity as a fraction of $V_{critical}$. For smaller fractions (up to about $0.5V_{critical}$) this relationship remains nearly linear. Larger values of $V/V_{critical}$ deviate more rapidly and the Doppler broadening measurment becomes a less reliable indicator of projected rotational velocity. Image is Figure 1 from "Be-star rotation: how close to critical?", Townsend, R. H. D.; Owocki, S. P.; Howarth, I. D. 2004 Monthly Notices of the Royal Astronomical Society, Volume 350, Issue 1, pp. 189-195. © Royal Astronomical Society. Used with permission of the author.

of this interaction. If the circumstellar material were spherically distributed instead, each polarized photon passing through the material would be cancelled by an oppositely polarized photon, thereby resulting in zero net polarization.

Advances in interferometry since the dawn of the 21st century helped to renew interest in the Be star phenomenon. As stated previously, examination of the circumstellar environment of Be stars is necessary to understand the phenomenon. The spatial extent of these circumstellar regions tend to be on the order of milliarcseconds, as mentioned previously. Far too small to be observed by ordinary telescopes, investigation of circumstellar environments was restricted to means such as spectroscopy and polarimetry (Section 1.7). While these techniques continue to yield significant amounts of information about circumstellar environments, further elucidating their structure was difficult until appropriate tools became available.

The key to observing the environment surrounding a Be star, and thus beginning to understand the Be phenomenon, is the ability to distinguish the star and its disk from a point source. This is the particular strength of interferometry. Interferometry alone can provide information about the spatial extent and orientation of a disk. Combining spectroscopy with interferometry yields more useful information. Spectroscopic observations can reveal the angle at which a disk is oriented with respect to Earth by the shape of the emission line. The

extent of these emission lines also allows observers to make inferences about a disk's rotational velocity; disks that rotate more quickly have broadened emission lines relative to slower rotators.

While spectroscopy has and continues to prove its utility in the study of the Be phenomenon, its ability to reveal the behaviour of these systems is limited. Spectra are a sort of "average" or "sum" of the disk as a whole, which forces certain assumptions about a lack of detail within the disk to be made. However, it is well understood that Be star disks are not featureless distributions of circumstellar material. They have, for instance, asymmetries in density distribution which can be revealed interferometrically but will not be described in a detailed way by examining the stellar spectrum. For example, using the VLTI, Meilland et al. (2007) found asymmetry in the disk of κ CMa. Prior spectroscopic studies were unable to reveal this level of detail in the disk's structure.

Polarimetry, and the role polarization plays in Be star disks, was described here in Section 1.6.1. Not surprisingly, adding polarimetric data about the structure of the disks can only enhance our ability to constrain our models and explain the processes within the disk.

1.6.2 Approach to Modelling

As described in detail in Section 1.4, Bedisk and Beray produce sophisticated hydrodynamical models which can be related to a number of physical processes in the disk. Calculating a large number of models has allowed us to select $(n, \rho_\circ, i)$ correspond to models that best reproduce the observations. In order to validate the models they were compared to prior published results including Quirrenbach et al. (1997), Delaa et al. (2011) and others. Most of the emphasis is placed on the Hα profile and interferometric visibilities. Along with these, however, the codes also produce model spectral energy distributions (SEDs) which can be compared directly to observed SEDs.

The observations utilized in this work came from two sources. Chapter 2 used data contained in the Palomar Testbed Interferometer Archive. These data are publicly available. The observations analyzed for Chapters 3 and 4 were made by one of the coauthors at the Navy Precision Optical Interferometer and Lowell Observatory in 2006 and 2010.

1.7 Goals and Concluding Remarks

The goal of this research program is to use observations to constrain the models produced by the Bedisk and Beray codes. Interferometric data, for reasons explained in the preceding sections, is uniquely suited to the study of circumstellar environments. The evolution of our understanding of disk dynamics, accompanied by the vast improvement in computer hard-

ware, has led us to a point where it has become feasible to model and interpret complicated disk behaviours. The focus is to elucidate the disks and eventually to understand whatever role they play in B-star evolution. Perhaps more importantly, due to the ubiquity of disks throughout the universe, understanding the dynamics of one type will go a long way toward explaining others.

The Palomar Testbed Interferometer (PTI) study is covered in Chapter 2. It utilized a set of archived K-band observations for sixteen stars, and takes a relatively straightforward approach to modelling disks by comparing observations first to geometrical models, and then to the more sophisticated output of BEDISK. That study shows that the agreement between the density models varied with spectral type. Generally, earlier Be stars had better agreement with the models, and fits for the subset of B8 stars were especially poor. Given the limitations of the code and the relatively poor quality of the observations, the study is nonetheless a useful starting point for investigating how the code might be updated to constrain the models. Since then, the BERAY and 2DDFT codes have been developed and permit us to produce better physical models via improved constraints.

Chapter 3 is an analysis of 48 Per, one of two stars from the PTI study examined in far greater detail. A set of 291 NPOI observations with superb (u, v)-plane coverage were acquired in November and December 2006. Spectroscopic line profiles in Hα were also recorded during that same timespan. Because of the level of sky coverage available from this dataset, we expect to be able to determine constraints on our disk models to greater precision than before.

Our study of ψ Per, mentioned in Section 1.2.4 and described in detail in Chapter 4, is especially interesting. It has been established elsewhere that ψ Per shows stable periods interspersed with periods of activity (Draper et al., 2014). Like 48 Per, it was observed both interferometrically and spectroscopically in the autumn of 2006. Because NPOI observations of ψ Per were made as well in 2010, we have a unique opportunity to analyze the changes in interferometric signatures caused by this variability. We find that the variability, as well as its attendant changes to the interferometry, indicates that the extended structure is evolving. The use of observations taken over multiple epochs to do so is unprecedented. We find specific changes in the structure of ψ Per and its disk and quantify those changes using the tools described in Section 1.4.

Modelling with BEDISK as detailed in Chapter 2 permitted us to make detailed temperature and density structure calculations for these stars, which were constrained with the observed interferometry. Chapter 3 discusses the characteristics of 48 Persei along with how the modelling was done and the results that were produced. 48 Per was quiescent and observed in

only one epoch. The second star, ψ Per, is covered similarly in Chapter 4. Unlike 48 Per, ψ Per is a variable star observed in 2006 and 2010. Prior studies have been unable to identify variability via interferometry. This thesis concludes with Chapter 5, which summarizes the results of the studies described in the following chapters and discusses implications of this work for future Be star research.

References

Armstrong, J. T., Mozurkewich, D., Rickard, L. J., et al. (1998). *ApJ* 496, p. 550. DOI: 10.1086/305365.

Bjorkman, J. E. and Cassinelli, J. P. (1993). *ApJ* 409, pp. 429–449. DOI: 10.1086/172676.

Bracewell, R. N. (2000). Boston: McGraw Hill.

Carciofi, A. C. (2011). In: *IAU Symposium*. Ed. by C. Neiner, G. Wade, G. Meynet, et al. Vol. 272. IAU Symposium, pp. 325–336. DOI: 10.1017/S1743921311010738. arXiv: 1009.3969 [astro-ph.SR].

Carciofi, A. C. and Bjorkman, J. E. (2008). *ApJ* 684, pp. 1374–1383. DOI: 10.1086/589875. arXiv: 0803.3910.

Carciofi, A. C., Bjorkman, J. E., Otero, S. A., et al. (2012). *ApJL* 744, L15, p. L15. DOI: 10.1088/2041-8205/744/1/L15. arXiv: 1112.0053 [astro-ph.SR].

Cassinelli, J. P., Brown, J. C., Maheswaran, M., et al. (2002). *Astrophysical Journal* 578, pp. 951–966. DOI: 10.1086/342654. eprint: astro-ph/0207370.

Coté, J. and Waters, L. B. F. M. (1987). *A & A* 176, pp. 93–106.

Cox, A. N. (2000). New York: AIP Press; Springer.

Delaa, O., Stee, P., Meilland, A., et al. (2011). *A & A* 529, A87, A87 (D11). DOI: 10.1051/0004-6361/201015639.

Dougherty, S. M. and Taylor, A. R. (1992). *Nature* 359, pp. 808–810. DOI: 10.1038/359808a0.

Draper, Z. H., Wisniewski, J. P., Bjorkman, K. S., et al. (2014). *ApJ* 786, 120, p. 120. DOI: 10.1088/0004-637X/786/2/120. arXiv: 1402.5240 [astro-ph.SR].

Frémat, Y., Zorec, J., Hubert, A.-M., et al. (2005). *A & A* 440, pp. 305–320. DOI: 10.1051/0004-6361:20042229. eprint: arXiv:astro-ph/0503381.

Grzenia, B. J. (2009). MA thesis. Central Michigan University.

Halonen, R. J. and Jones, C. E. (2013). *ApJS* 208, 3, p. 3. DOI: 10.1088/0067-0049/208/1/3. arXiv: 1307.6220 [astro-ph.SR].

Hanuschik, R. W., Hummel, W., Dietle, O., et al. (1995). *A & A* 300, p. 163.

Harmanec, P. (1983). *Hvar Observatory Bulletin* 7, pp. 55–88.

Haubois, X., Carciofi, A. C., Rivinius, T., et al. (2012). *ApJ* 756, 156, p. 156. DOI: 10.1088/0004-637X/756/2/156. arXiv: 1207.2612 [astro-ph.SR].

Jackson, J. D. (1975). New York: Wiley.

Jones, C. E., Tycner, C., and Smith, A. D. (2011). *AJ* 141, 150, p. 150. DOI: 10.1088/0004-6256/141/5/150. arXiv: 1103.1514 [astro-ph.SR].

Kogure, T. and K.-C. Leung, eds. (2007). Vol. 342. Astrophysics and Space Science Library.

Labeyrie, A., Lipson, S., and Nisenson, P. (2006). Cambridge University Press.

Lamers, H. J. G. and Pauldrach, A. W. A. (1991). *A & A* 244, pp. L5–L8.

Lawson, P. R., ed. (2000).

McDavid, D., Bjorkman, K. S., Bjorkman, J. E., et al. (2000). In: *IAU Colloq. 175: The Be Phenomenon in Early-Type Stars*. Ed. by M. A. Smith, H. F. Henrichs, and J. Fabregat. Vol. 214. Astronomical Society of the Pacific Conference Series, p. 460.

Meilland, A., Millour, F., Stee, P., et al. (2007). *A & A* 464, pp. 73–79. DOI: 10.1051/0004-6361:20065410. eprint: arXiv:astro-ph/0611563.

Meynet, G. (1999). In: *Spectrophotometric Dating of Stars and Galaxies*. Ed. by I. Hubeny, S. Heap, and R. Cornett. Vol. 192. Astronomical Society of the Pacific Conference Series, p. 41.

Millar, C. E. and Marlborough, J. M. (1998). *ApJ* 494, p. 715. DOI: 10.1086/305229.

Oudmaijer, R., Haniff, C., Buscher, D., et al. (2012). *Astronomy and Geophysics* 53.2, pp. 020000–2. DOI: 10.1111/j.1468-4004.2012.53214.x.

Oudmaijer, R. D., Wheelwright, H. E., Carciofi, A. C., et al. (2011). In: *IAU Symposium*. Ed. by C. Neiner, G. Wade, G. Meynet, et al. Vol. 272. IAU Symposium, pp. 418–419. DOI: 10.1017/S1743921311011008.

Owocki, S. (2006). In: *Stars with the B[e] Phenomenon*. Ed. by M. Kraus and A. S. Miroshnichenko. Vol. 355. Astronomical Society of the Pacific Conference Series, p. 219.

Owocki, S. P., Cranmer, S. R., and Gayley, K. G. (1998). *Ap & SS* 260, pp. 149–159. DOI: 10.1023/A:1001895508424.

Pauldrach, A. W. A. and Puls, J. (1990). *A & A* 237, pp. 409–424.

Percy, J. R. (1994). In: *Pulsation; Rotation; and Mass Loss in Early-Type Stars*. Ed. by L. A. Balona, H. F. Henrichs, and J. M. Le Contel. Vol. 162. IAU Symposium, p. 299.

Poeckert, R. and Marlborough, J. M. (1978). *ApJ* 220, pp. 940–961. DOI: 10.1086/155984.

Porter, J. M. and Rivinius, T. (2003). *PASP* 115, pp. 1153–1170. DOI: 10.1086/378307.

Pringle, J. E. (1981). *ARA & A* 19, pp. 137–162. DOI: 10.1146/annurev.aa.19.090181.001033.

Quirrenbach, A., Bjorkman, K. S., Bjorkman, J. E., et al. (1997). *ApJ* 479, 477 (Q97). DOI: 10.1086/303854.

Rivinius, T., Baade, D., Štefl, S., et al. (2001). *A & A* 379, pp. 257–269. DOI: 10.1051/0004-6361:20011335.

Rivinius, T., Baade, D., Stefl, S., et al. (2002). *The Messenger* 108, pp. 20–24.

Secchi, A. (1866). *Astronomische Nachrichten* 68, p. 63. DOI: 10.1002/asna.18670680405.

Shakura, N. I. and Sunyaev, R. A. (1973). *A & A* 24, pp. 337–355.

Sigut, T. A. A. (2011). In: *IAU Symposium*. Ed. by C. Neiner, G. Wade, G. Meynet, et al. Vol. 272. IAU Symposium, pp. 426–427. DOI: 10.1017/S1743921311011045.

Sigut, T. A. A. and Jones, C. E. (2007). *ApJ* 668, pp. 481–491. DOI: 10.1086/521209. arXiv: 0706.4036.

Silaj, J., Jones, C. E., Tycner, C., et al. (2010). *ApJS* 187, pp. 228–250. DOI: 10.1088/0067-0049/187/1/228.

Slettebak, A. (1979). *Space Sci. Rev.* 23, pp. 541–580. DOI: 10.1007/BF00212356.

– (1982). In: *Be Stars*. Ed. by M. Jaschek and H.-G. Groth. Vol. 98. IAU Symposium, pp. 109–121.

Struve, O. (1931). *ApJ* 73, p. 94. DOI: 10.1086/143298.

ten Brummelaar, T. A., McAlister, H. A., Ridgway, S. T., et al. (2005). *ApJ* 628, pp. 453–465. DOI: 10.1086/430729. eprint: astro-ph/0504082.

Thompson, A. R., Moran, J. M., and Swenson, G. W. (1986). New York: Wiley-Interscience.

Townsend, R. H. D., Owocki, S. P., and Howarth, I. D. (2004). *MNRAS* 350, pp. 189–195. DOI: 10.1111/j.1365-2966.2004.07627.x. eprint: arXiv:astro-ph/0312113.

Tycner, C. (2011). In: *IAU Symposium*. Ed. by C. Neiner, G. Wade, G. Meynet, et al. Vol. 272. IAU Symposium, pp. 337–341. DOI: 10.1017/S174392131101074X.

– (2013). unpublished observations.

von Zeipel, H. (1924). *MNRAS* 84, pp. 665–683.

Wade, G. A., Folsom, C. P., Petit, P., et al. (2014a). *Monthly Notices of the RAS* 444, pp. 1993–2004. DOI: 10.1093/mnras/stu1541. arXiv: 1407.3991 [astro-ph.SR].

Wade, G. A., Petit, V., Grunhut, J., et al. (2014b). *ArXiv e-prints*. arXiv: 1411.6165 [astro-ph.SR].

Wisniewski, J. P., Kowalski, A. F., Bjorkman, K. S., et al. (2007). *ApJL* 656, pp. L21–L24. DOI: 10.1086/512123. eprint: arXiv:astro-ph/0701010.

Yudin, R. V. (2001). *A & A* 368, pp. 912–931. DOI: 10.1051/0004-6361:20000577.

Zorec, J. and Briot, D. (1997). *A & A* 318, pp. 443–460.

"I saw the constellations reveal themselves
one star at a time..."

The Tragically Hip, "Bobcaygeon"

2

Palomar Testbed Interferometer

2.1 Introduction

B-emission (Be) stars are hot, rapidly rotating main sequence or slightly evolved stars surrounded by gaseous disks. Their visible spectra have at least one hydrogen Balmer emission line (Jaschek, Slettebak, and Jaschek, 1981). The emission lines need not be continuously present, and a Be star does not lose its classification in the event that the line can no longer be observed (Porter and Rivinius, 2003). The general view is that the emission lines arise from the presence of matter which has accumulated around the star due to stellar mass loss. According to Zorec and Briot (1997) the proportion of Be stars among ordinary B stars is at least 17% and is as high as 34% for spectral type B1e. Interestingly, they also find that the frequency of Be stars is independent of luminosity class for the classes V to III. This suggests that Be stars do not represent a specific stage in stellar evolution but that the properties of the star itself and its formation history are responsible for the observational features of this group.

Struve (1931) proposed the existence of disks around a number of stars including γ Cassiopeiae and now it is commonly accepted that disk-like distributions of gas surround Be stars. The study of these disks has been an active area of research for decades but none of the proposed models have been completely successful at explaining the origin or the physical characteristics of the circumstellar disks (Porter and Rivinius, 2003). Improvements in instrumentation, especially high resolution interferometry (see, for example, Quirrenbach et

a version of this chapter appears as B. J. Grzenia, C. Tycner, C. E. Jones, S. A. Rinehart, G. T. van Belle, T. A. A. Sigut; 2013, AJ, 145, 141 © AAS.

al. (1997) and Tycner et al. (2005)), and the suggestion by Townsend, Owocki, and Howarth (2004) that Be star rotation rates have been systematically underestimated, have rekindled interest in finding viable models for these systems. Recently, the viscous disk model, originally championed by Lee, Osaki, and Saio (1991), has been used successfully to model a number of key observables from Be star systems (see, for example, Carciofi et al. (2012)).

A common characteristic that all Be stars appear to share is rapid stellar rotation. For some Be stars their rotational velocity may approach their critical velocity ($v_{\rm crit}$) at which material at the equator would be rotationally supported (Townsend, Owocki, and Howarth, 2004). The actual values for their rotation rates are quite contentious, but it is generally accepted that the rates are subcritical $\sim 0.7 v_{\rm crit}$ (Porter, 1996). Establishing these rotational velocities alongside with the general physical properties of the disk structures is pivotal to our understanding of the processes that give rise to Be star behaviors (Cranmer, 2009).

In this study, we concentrate on establishing the physical characteristics of the circumstellar disks associated with these rapidly rotating stars by constraining numerical models with interferometric observations. In particular, we utilize high-angular resolution observations of 16 B-type emission stars that were obtained with the Palomar Testbed Interferometer (PTI) and which resolve the circumstellar structures in the K-band. Our study focuses on the classical Be type stars, however, we included all B-type objects with emission in the archive. For example, β Per is an Algol system, P Cyg is a luminous blue variable, and some of the other program stars are likely members of binary systems. Nevertheless, we included all of the observations available in this archival set to maximize the number of objects in our study and to provide these observations to the community. The targets were selected because they fall within the hour angle and declination limits of the PTI instrument (see Colavita et al. (1999) figure 9 for details). Our program stars are listed in Table 2.1 along with their HD number, spectral type, and any special identifying features.

The results of this study are an extension of a similar observational study by Gies et al. (2007) who observed four Be stars with the CHARA interferometer in the K′-band and obtained very detailed constraints on the disk parameters. The targets in common with Gies et al. (2007) and this study include γ Cassiopeiae, ϕ Persei and ζ Tauri. Gies et al. (2007) utilized isothermal disk models to obtain very precise disk parameters, while the results presented in this work are based on disk models that enforce self-consistent temperature distributions. In Section 2.2, we give an overview of our techniques for calibrating and analyzing the observations. We describe the geometrical and numerical modelling procedures we employed to characterize the disks in Section 2.3. The results of the comparison of our detailed numerical models to the calibrated observations are given in Section 2.4. Section 2.5 provides a compar-

ison of our results with other findings and Section 2.6 summarizes our work.

2.2 Observations

The interferometric observations used in this study have been acquired at the Palomar Testbed Interferometer (PTI), located at the Palomar Observatory in California. For a complete description of PTI, the reader is referred to Colavita et al. (1999). The observations used in our analysis were acquired between 1998 and 2006 (see Table 2.1 for the range of dates associated with each target).

The raw observations have been extracted from the PTI archive, which contain only those observations that meet specific quality standards. For example, observations are assigned grades according to the quality based on observational parameters such as jitter, squared visibility and photon counts. Furthermore, the criteria for grading the results are based on past performance of the instrument rather than specific limits, thereby giving a more robust assessment of the quality of the observations under consideration.

Data analysis commenced with processing of essentially raw values from the instrument that contains some minor preprocessing and are known as Level 1 (L1) values (Colavita, 1999). These values consist of 150 s of integration, averaged over all wavelength channels from 2.0 to 2.4 μm, and include observations of the target and its calibrator stars. For the purpose of our study, we have opted to exclude observations that have jitter in excess of 1.50 radians, thereby producing "cleaner" results than what would be obtained without such a restriction. Jitter is a means of quantifying reductions of V^2 from an ideal case. Further, jitter describes seeing conditions and the quality of the interferometric observations (Colavita, 1999).

The calibration of the Be star V^2 values is performed by estimating the interferometer system visibility (V^2_{SYS}) through observing calibration sources with empirically established point-like angular diameters (van Belle et al., 2008) to estimate the V^2 measured by an ideal interferometer at that epoch and then normalizing the raw Be star visibility by V^2_{SYS} (Boden et al., 1998; Mozurkewich et al., 1991; van Belle and van Belle, 2005). Uncertainties in the system visibility and the calibrated target visibility are inferred from internal scatter among the values in an observation using standard error-propagation calculations (Colavita, 1999). Calibrating our point-like calibration objects against each other produced no evidence of systematics, with all objects delivering reduced $V^2 = 1$. PTI's limiting night-to-night measurement error is $\sigma_{V^2_{\text{SYS}}} \approx 1.5 - 1.8\%$, the source of which is most likely a combination of effects: uncharacterized atmospheric seeing (in particular, scintillation), detector noise, and other instrumental effects. This measurement error limit is an empirically established floor from the previous study of Boden et al. (1999).

Table 2.1. List of Targets

Target	HD	Spectral Type	N	Obs. Seasons	Distance (pc)	Notes
γ Cas . .	5394	B0IVpe	14	2002	188 ± 20	possible binary[a,b,d]
ϕ Per . .	10516	B2Vpe	245	2000 – 2006	220 ± 9.7	short-period variability,binary[c,d]
β Per . .	19356	B8V	25	1998 – 1999	28 ± 1	Algol-type variable[e,f]
ψ Per .	22192	B5Ve	51	2000 – 2005	179 ± 7.04	short-period variability[c,d]
η Tau .	23630	B7III	108	1998 – 2001	124 ± 6.42	
28 Tau .	23962	B8IVe	48	2000 – 2006	208 ± 29	variable [d]
48 Per .	25940	B3Ve	5	1999 – 2002	146 ± 3.42	
ζ Tau .	37202	B2IV	17	1998 – 2005	136 ± 15.3	variable; non-axisymmetric disk[c,d,g]
ν Gem	45542	B6IIIe	3	2001	167 ± 7.8	variable [d]
β CMi	58715	B8Ve	10	1999 – 2003	50 ± 0.49	
β Lyr . .	174638	B7Ve+	127	1998 – 2003	295 ± 15	β Lyrae variable[h]
28 Cyg	191610	B2.5Ve	38	2000 – 2001	317 ± 23	
P Cyg .	193237	B2pe	154	1998 – 2002	3100 ± 1500	luminous blue variable[i,j]
59 Cyg .	200120	B1.5Vnne	2	2001	435 ± 79	variable [d]
υ Cyg .	202904	B2Vne	30	1998 – 2001	197 ± 21	variable[c]
EW Lac	217050	B3IVpe	37	2001 – 2002	252 ± 18	variable[c,d]

Column 4: N represents the number of squared visibilities obtained at PTI. Column 5: Range of observational seasons covered by the observations. Column 6: Distance based on Hipparcos parallax (Perryman et al. (1997) for γ Cas; van Leeuwen (2007) for all others). Column 7: Distinguishing characteristics of the stars, as applicable and references. [a]Harmanec et al. (2000), [b]Miroshnichenko, Bjorkman, and Krugov (2002), [c]Hubert and Floquet (1998), [d]Rivinius, Štefl, and Baade (2006), [e]Goodricke (1783), [f]Zavala et al. (2010), [g]Schaefer et al. (2010), [h]Harmanec (2002), [i]de Groot (1969), [j]Balan et al. (2010)

PTI has three baselines, north-west (NW), south-west (SW), and north-south (NS) with lengths 86, 87 and 110 m, respectively. The calibrated observations used in this study were all made with either the NS or NW baselines. The majority of stars in our sample have been observed at these baselines; however a few had observations on only one. A list of Be stars for which observations have been extracted is given in Table 2.1. For the 16 targets, a total of more than 900 V^2 points have been obtained from the PTI archive and calibrated. The V^2 observations for all of our targets are plotted in Figure 2.1.

We note that the formal error bars shown in Figure 2.1 do not account for all sources of noise. The errors do account quite well for the sources of random noise that can be attributed to photon statistics and calibration errors. However, these formal errors will not account for all sources of atmospheric variations, especially those that are not well tracked by the calibrator star. In other words, if there is atmospheric perturbation of the wavefront on timescales shorter than the cadence of the target-calibrator pairs, then such variations will not be removed during the calibration process nor will they be fully accounted for with the formal error bars. Since many Be stars are known to be variable on a variety of timescales, certainly some of the scatter is a result of this characteristic. The amount of scatter depends on the frequency of such variation, the magnitude of the variability and whether the variability was captured during the time of our observations. Furthermore, since we combine the observations for each star, our calculated disk sizes (see Table 2.2) and our range of density parameters (see Section 2.4.3) represent an average over the time that the observations were acquired.

2.3 Methodology

2.3.1 Uniform Disk modelling

A common first approximation technique for determining the physical extent of the circumstellar regions of Be stars is the uniform disk (UD) model. The UD model, fitted to the interferometric observations in the K-band, assumes that the central star and the surrounding disk can be represented by a circularly symmetric and uniformly illuminated region on the sky. Uniform disk fits were performed for all stars for which there were sufficient number of calibrated observations and the resulting angular diameters are listed in Table 2.2. We used updated Hipparcos parallax measurements from van Leeuwen (2007) for all of our program stars with the exception of γ Cas which did not have an updated parallax. For this star we used the Perryman et al. (1997) measurement. Using these measurements we calculated the distance to each source (see Table 2.1), and converted the angular sizes in column three of Table 2.2 to physical dimensions in column four. The fifth column of Table 2.2 lists the re-

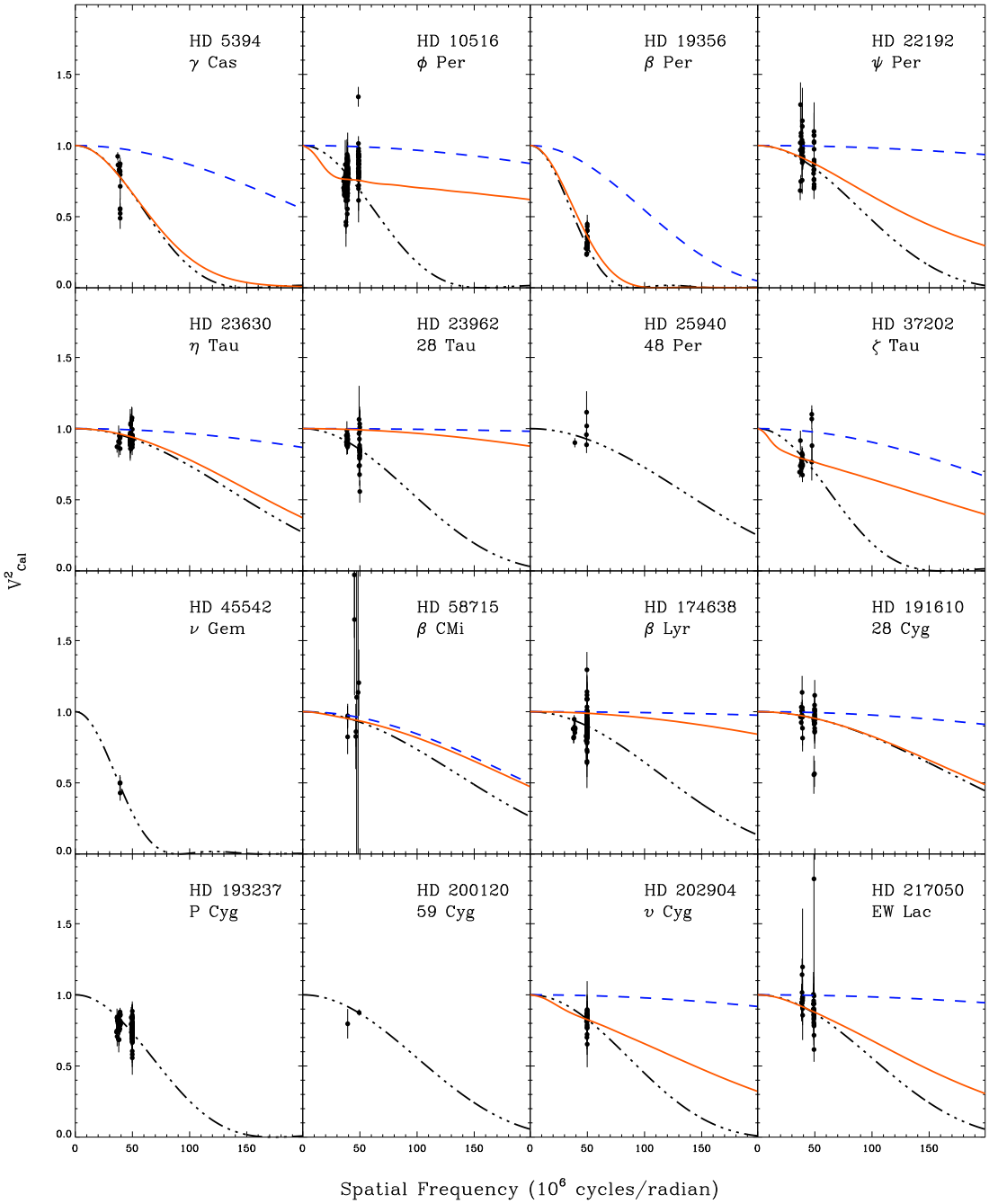

Figure 2.1: Squared visibility values for the 16 program stars. The uniform disk models fitted to the observations (dash-dotted line) along with uniform disk model representing the star itself based on the adopted stellar diameter (dashed line) are shown. The results based on the hydro-on models with the lowest χ^2_ν are also shown (solid lines).

Table 2.2. Uniform Disk Model Results

Spectral Group	Target	θ (mas)	θ (AU)	$\chi^2_\nu(\theta)$
B0	γ Cas	1.66 ± 0.05	0.31 ± 0.03	10.4
B2	ϕ Per	1.59 ± 0.01	0.35 ± 0.02	11.7
	48 Per	0.73 ± 0.13	0.11 ± 0.02	1.5
	ζ Tau	1.57 ± 0.06	0.21 ± 0.03	5.86
	28 Cyg	0.574 ± 0.039	0.18 ± 0.02	1.65
	P Cyg[a]	1.45 ± 0.01	4.5 ± 2.3	2.06
	59 Cyg	0.98 ± 0.09	4.5 ± 0.43	0.09
	υ Cyg	1.14 ± 0.01	0.22 ± 0.02	4.43
	EW Lac	0.981 ± 0.033	0.25 ± 0.02	1.78
B5	ψ Per	1.1 ± 0.03	0.20 ± 0.01	4.49
	ν Gem	2.78 ± 0.11	0.46 ± 0.03	0.587
B8	β Per (Algol)	2.78 ± 0.02	0.077 ± 0.003	3.07
	η Tau	0.712 ± 0.011	0.088 ± 0.005	0.71
	28 Tau	1.04 ± 0.02	0.22 ± 0.03	1.47
	β CMi	0.719 ± 0.323	0.036 ± 0.016	1.16
	β Lyr	0.584 ± 0.02	0.17 ± 0.01	1.42

Column 3: Size of uniform disk (UD) model in milliarcseconds. Column 4: Size of UD in astronomical units, based on the Hipparcos distances in Table 2.1. Column 5: χ^2_ν errors estimated from the UD modelling routine and reduced by the number of available observations per star. [a]System possesses spherical wind structure.

duced χ^2 (denoted χ^2_ν) errors estimated from the UD modelling routine and reduced by the number of available observations per star.

The UD modelling represents a good first-order approximation and is commonly used as a model of choice, especially if the quantity of observations is limited or a simple (and single) parametric description of the circumstellar structure is desired. Nonetheless, it should be noted that the estimated disk sizes are dependent on the functional form of the adopted model and adopting a different geometrical model for the disk will produce different disk sizes. Furthermore, a UD model assumes that the disk and the central star can be approximated with a single uniform surface intensity across the K-band. Of course, a more realistic model would treat the central star and surrounding disk independently, necessitating a different approach to modelling.

In addition to the UD modelling, described above, we also fit our program stars with ellip-

tical disks (ED) to check for deviations from circular symmetry on the plane of the sky. See the paper by Tycner et al. (2006) for details about ED fits. We report our findings below in Section 2.4.

2.3.2 Numerical Disk modelling

The basic model for a circumstellar disk of a Be star represented by a geometrically thin, equatorial disk, heated by the photoionizing radiation field of the central star was championed by Poeckert and Marlborough (1978) and since then has become a highly cited model. An extension of the model to a non-uniform disk temperature structure based on radiative equilibrium was first obtained by Millar and Marlborough (1998). The numerical disk models presented in this study are computed using the latest version of this disk model, which enforces radiative equilibrium and vertical hydrostatic equilibrium to obtain the disk temperature structure (Sigut and Jones, 2007; Sigut, McGill, and Jones, 2009). The numerical code (which we refer to as Bedisk code) has been successfully used to interpret a wide range of Be star observables, from interferometric visibilities (Jones et al., 2008; Tycner et al., 2008) to hydrogen line profiles (Silaj et al., 2010) and infrared line fluxes (Jones et al., 2009).

The disk modelling routine, Bedisk, as developed by Sigut and Jones, 2007 provides a more physical representation of the star-plus-disk system. Notably, a distinction is made between the intensity of the central star and that of the disk. The central star is represented by a synthetic spectrum chosen from the grid of synthetic model atmospheres of Kurucz (1993), selected based on the $T_{\rm eff}$ and $\log(g)$ of the central star. The disk is modelled with a power law density grid as described by

$$\rho(R, Z) = \rho_{\circ} \left(\frac{R_*}{R}\right)^n \exp\left[-\left(\frac{Z}{H}\right)^2\right], \tag{2.1}$$

where $\rho_{\circ}$ is the density of the disk at the stellar surface, n is the power law exponent, R is the distance from the stellar rotation axis (while R_* is the stellar radius), Z is distance in the direction parallel to the star's axis of rotation (and perpendicular to the disk) and H is the vertical scale height, defined as:

$$H = \sqrt{\frac{2R^3}{\alpha_{\circ}}}, \tag{2.2}$$

where

$$\alpha_{\circ} = GM_* \frac{\mu_{\circ} m_{\rm H}}{kT_{\circ}}. \tag{2.3}$$

In Equation 2.3, G is the gravitational constant, M_* is the mass of the central star, $\mu_{\circ}$ refers to

the mean molecular weight of the circumstellar material, m_H is the atomic mass of hydrogen, k is the Boltzmann constant, and T_0 is an assumed isothermal temperature for the disk (which is used only to calculate the disk scale height in Equation 2.1). Assuming a constant temperature irrespective of the vertical height Z in this manner allows radiatively balanced models to be generated, although the vertical density distribution is not exactly consistent with the calculated temperature distribution (we refer to these models as *hydro-off*). However, Sigut, McGill, and Jones (2009) has described how BEDISK code can also self-consistently solve for the vertical temperature and density structure of the disk while enforcing vertical hydrostatic equilibrium. In this case, the vertical density structure no longer has the analytic form of equation 2.1, although the radial power-law drop-off is still assumed (see Sigut, McGill, and Jones, 2009, for more details). We refer to the models generated with the vertical hydrostatic equilibrium enforced as *hydro-on* models.

An important aspect of BEDISK is its use of solar chemical composition. Earlier codes neglected the metallicity of the disk material, given that the disks are obviously composed predominantly of hydrogen. However, heavier elements contribute to the heating and cooling processes within the disk and therefore affect both the thermal structure of the disk and the intensities of its emission lines (Jones, Sigut, and Marlborough, 2004). Although Be stars are found in both lower- and higher-metallicity environments, with lower metallicity showing higher prevalence of the Be phenomenon (Martayan, Baade, and Fabregat, 2010; McSwain and Gies, 2005), we opt to model the stars in this study at the solar chemical composition. We made this choice because our program stars are located within the Milky Way. Regions such as the Small Magellanic Cloud (SMC) contain a larger proportion of low-metallicity Be stars; the lack of metallicity in the SMC stars means their stellar winds are less efficient at removing angular momentum from the system. This facilitates faster rotational rates and the formation of equatorial gaseous disks. Stars in the Milky Way are generally more metal-rich than those in the SMC, making the use of models with solar metal concentrations appropriate.

The models presented here utilized an 84 by 50 grid, meaning the grid consists of 84 radial rings starting at the stellar photosphere, where at each radial location calculations are performed at 50 steps above the mid-plane (mirror symmetry is assumed for the region below the mid-plane). Figure 2.2 shows the computation grid in the disk as function of R and Z. The output generated by the BEDISK code is in the form of spectral energy distributions, which were used to construct synthetic images. The UD modelling assumed circular symmetry and we extend this assumption to our thermal disk models. However, it is clear that some stars will neither be viewed pole-on, nor might their disks be circularly symmetric. For

example, the disk of ζ Tauri (HD 37202) is known to be asymmetric and viewed at a non-zero angle of incidence (Carciofi et al., 2009; Quirrenbach et al., 1997; Tycner et al., 2004; Vakili et al., 1998). However, because the quantity of interferometric values for most of our sources is quite small and in some cases we only have observations from one baseline orientation, reliable determination of deviation from circular symmetry is not possible. Therefore, for the purpose of determining the general physical characteristics of the disks, as opposed to detailed geometrical properties, we neglect the effects of projection and any deviations from circular symmetry in our analysis and instead approximate the disks with circularly symmetric models seen pole-on.

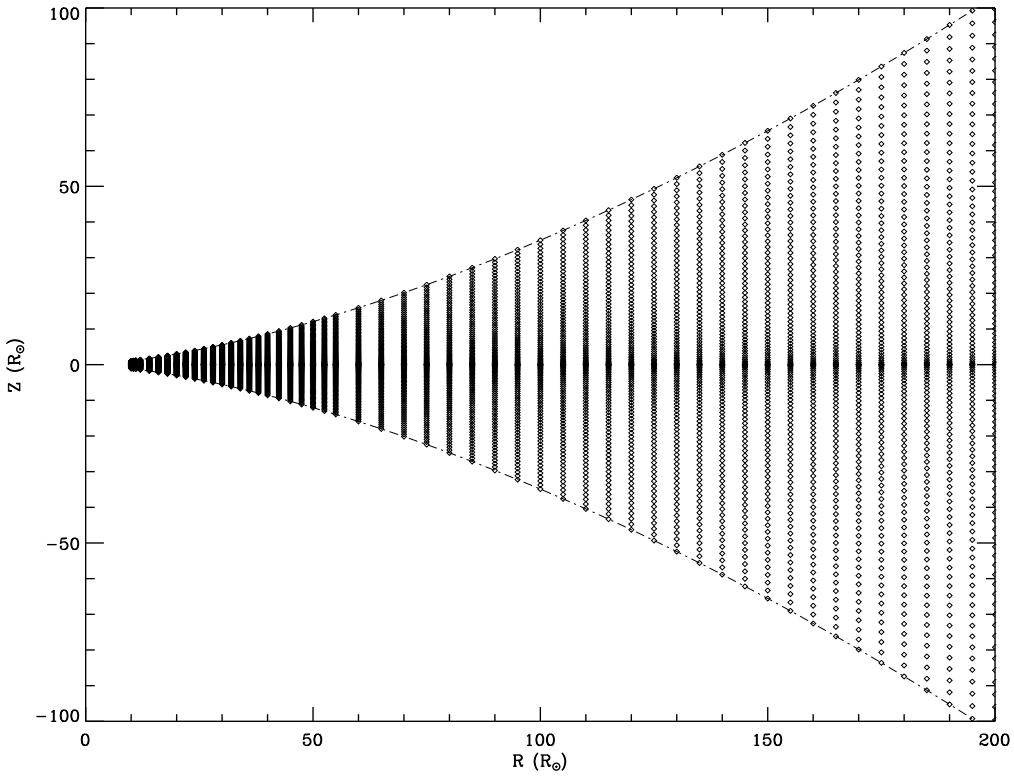

Figure 2.2: The computational grid throughout the disk as a function of R and Z adopted for this investigation. The disk thickness increases with R as described in Equations 2.1 and 2.2. In other words, the scale height H increases with distance from the photosphere, resulting in a disk that ``puffs up.''

Following the procedure outlined in Tycner et al. (2008) for comparing synthetic images to interferometric observations, we compared the synthetic images from BEDISK to the squared visibilities for each of the 16 sources. We used a χ^2 statistic as a measure of goodness-of-fit to find a range of n and $\rho_\circ$ values that best represent the characteristics of the Be star disk.

The use of circularly-symmetric (or pole-on) images for the analysis of the PTI observa-

tions does require some further justification. To this end, we have used the BERAY code of Sigut (2011) to construct images of some of our model disks for a range of inclination angles. The BERAY code uses as input the disk temperature and density structure from a BEDISK solution to solve the radiative transfer equation along a series of rays through the Be star-plus-disk system. The non-LTE level populations computed by BEDISK are used to construct the gas opacity and emissivity. Rays which terminate on the stellar surface use a model photospheric intensity (appropriate for the adopted $T_{\rm eff}$ and $\log(g)$ for the star) for the boundary condition at the start of the ray. Rays which pass through the disk assume no incident radiation. Thus BERAY produces monochromatic images of the Be star system on the sky which can be used to evaluate how serious an error is made by analyzing the PTI sample with the circular, zero-inclination images produced by BEDISK.

Figure 2.3 shows the results for a model of the Be star γ Cas with disk density parameters $n = 3.5$ and $\rho_0 = 1.0 \times 10^{-10}$ g $\cdot$ cm^{-3}. An outer disk radius of $R_d = 12\ R_*$ was assumed, and the images were produced in the K band (2.179 μm) with a resolution on the sky of 0.05 R_*. The model was assumed to be viewed at a distance of 188 pc, the Hipparcos catalogue distance for γ Cas (Perryman et al., 1997). Images were produced for viewing inclinations of 5, 45, and 60°. To compute the interferometric visibilities, the images were summed along the minor axis of the disk, and the resultant 1D images (along the major axis) were discrete Fourier transformed (DFT) to produce the corresponding visibilities. The major axis was selected in order to use the largest spatial scale present in each image, which gives the largest departures from unity in the corresponding visibilities (where a visibility of 1 corresponds to an unresolved point source). Hence this approach is representative of what happens when the disk is fully resolved by the observations. The left panel of Figure 2.3 shows the minor-axis summed, 1D images, and the right panel, the DFT of these images. As can be seen from the figure, the effect of inclination is quite small; the visibilities at 50 Mλ, the maximal spatial frequency for the 110 m baseline of PTI in the K band, differ by about $\pm$10%. This difference is likely well within our observational uncertainties. Thus the signal is mainly sensitive to the bulk properties of the disk gas (to within the limits shown) and not to the geometry along the unresolved dimension. For this reason, we are confident that the uncertainties introduced by use of the circular, pole-on image of BEDISK to analyze our sample of Be stars in a uniform manner are entirely commensurate with the PTI data quality.

The capabilities of the BERAY code are more thoroughly explored in Chapters 3 and 4.

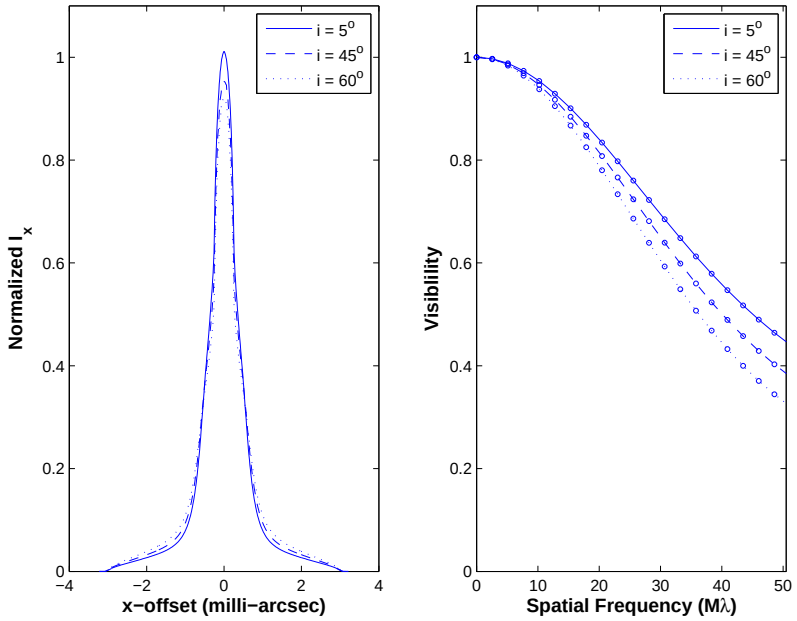

Figure 2.3: Results of an additional analysis to determine whether the pole-on disk model is justified. Left panel: major axis, summed intensity as a function of off-set from the centre of the star (in milli-arseconds) for the γ Cas model seen at three inclination angles. The profiles are normalized to unit area. The disk model assumed $n = 3.5, \rho_0 = 1.0 \times 10^{-10}\,\mathrm{g \cdot cm^{-3}}$ and $R_d = 12R_*$. Right panel: the corresponding discrete Fourier transforms expressed as visibility versus spatial frequency (in units of 10^6 cycles/radian.)

2.4 Results

2.4.1 Uniform Disks

Figure 2.1 shows the observed squared visibility versus spatial frequency for the 16 stars in our sample. The model curves for the circularly symmetric UD results, with the angular disk sizes listed in Table 2.2, are also shown. The stars listed in Table 2.2 have been divided into groups based on spectral type for ease of comparison with the results from the next section, which separate all the targets into one out of four groups. The groups divide the spectral range B0–B8 into four groups with γ Cas as the only B0 star; B1.5 to B3 stars in the second group, B5 to B6 stars in the third group, and all remaining stars (B7 to B8) in the fourth group.

Overall the UD fits model the observations well with a few exceptions. The targets that showed relatively low quality fits, as determined based on the reduced χ^2 (χ^2_ν, which are χ^2 goodness-of-fit quantities reduced by the number of observations against which a given model is evaluated) values listed in Table 2.2, were γ Cas, ϕ Per, ζ Tau, υ Cyg, ψ Per, and β Per. We attribute these low quality fits to a combination of non-pole geometry for γ Cas (see Section 2.4.2), variations from axisymmetry, variability, and at least in the last case to a possible binary signature. However, as stated previously, since our observations cover only very limited range of spatial frequencies and we have very small number of values in each of the observing seasons we choose to average these effects by simply fitting a single circularly symmetric model. We believe that such a simple and single parametric description of the interferometric signature is still useful to describe the most general property of the emitting region, i.e., its angular extent on the sky.

2.4.2 Elliptical Disks

In order to validate our assumption of the assumed circular symmetry for the circumstellar disks we fit the observed squared visibilities shown in Figure 2.1 with elliptical uniform disk models. The fitting procedure followed the same modelling approach as outlined in section 4 of Tycner et al. (2006) where the model for the circumstellar disk can be represented by an elliptical uniform disk with an axial ratio *r* defined as the ratio of the minor to major axis (i.e., an axial ratio of unity represents a circularly symmetric disk).

For the stars, β Per, ψ Per, η Tau, 28 Tau, β Lyr, and P Cyg we find axial ratios close to unity supporting the fact that our assumption of circular symmetry is appropriate. For these stars their ratios range from a minimum of 0.60 ± 0.05 to a maximum of 0.75 ± 0.04 with a mean and standard deviation of 0.73 ± 0.08, respectively. For ϕ Per, 48 Per, ζ Tau, β CMi, 28 Cyg, υ Cyg, and EW Lac the errors are very large and we conclude that the ellitpical uniform disk

fit simply fails to converge to a valid solution with a statistically meaningful axial ratio (i.e., we fail to detect axial flattening in these systems).

For 48 Per, ν Gem and 59 Cyg there were not enough observations to justify an elliptical model fit (see Table 2.4) so we did not include these targets in our modelling. γ Cas with an axial ratio of 0.30 ± 0.04 is the only target for which our ellitpical uniform disk modelling indicates significant ellipticity on the plane of the sky. Therefore, with a possible exception in the case of γ Cas, we proceed with our numerical models under the assumption of circular symmetry and assume that any minor deviations from circular symmetry will average out in the final results and can be ignored for the purpose of our analysis.

2.4.3 Disk Density Models

2.4.3.1 Spectral Group Bo

We begin our analysis with γ Cas, which is considered an archetypal Be star and as such is particularly well studied. However, observations show characteristics that are atypical for Be stars. For example, it exhibits unusual x-ray behavior and is probably a member of a binary system (Miroshnichenko, Bjorkman, and Krugov, 2002; Smith, Price, and Baker, 2004). Nonetheless, other studies of γ Cas are widely available for comparison and for that reason it is a good starting point. The total (n, ρ_o) grid utilized for the hydro-off models ranged from $1.0 < n < 6.6$ and $3.0 \times 10^{-11} < \rho_o < 5.0 \times 10^{-9}$ g $\cdot$ cm^{-3} and consisted of 283 models. The grid utilized for the hydro-on models was slightly different ranging from $0.1 < n < 6.6$ and $7.0 \times 10^{-12} < \rho_o < 3.0 \times 10^{-8}$ g $\cdot$ cm^{-3} and totaled 290 models. We note that the (n, ρ_o) grid is only approximately uniformly sampled with a coarser grid at the extremes of the parameters. Secondly, models were not produced for all combinations of n and ρ_o within this range. For example, models were required to be dense enough to produce emission but not so dense that gas became totally neutral. Generally, for increasing values of n (corresponding to faster density fall-off with increasing distance from the star) higher values of ρ_o are required. A comparison between models produced with and without hydrostatic equilibrium enforcement, revealed noticeable differences especially in the highest density models. Basically, if the disks are dense enough to develop a cool region in the equatorial plane, the hydrostatic enforced disks have material concentrated in a thinner volume towards the plane (Sigut, McGill, and Jones, 2009). These differences in density distribution lead to changes in the thermal structure of the disk.

Figures 2.4 and 2.5 give an example of the density and temperature distribution, respectively, for a very dense disk corresponding to the model with $n = 4.8$ and $\rho_o = 1.0 \times 10^{-9}$ g $\cdot$ cm^{-3} for γ Cas. Notice in Figure 2.4 that the region of highest density is narrower in

vertical extent nearest the star with hydro-on compared with the hydro-off case. For example, compare the density that corresponds to $\sim 10^{-12}$ g $\cdot$ cm^{-3} (in yellow) at a distance of $\sim 20\,R_\odot$. In the case of hydro-on, the vertical extent of this volume of gas is $\sim$ 20% narrower. Similarly, Figure 2.5 shows that near the star in the equatorial plane the vertical extent of the cooler region is clearly compressed with hydro-on compared to hydro-off. For example, at a distance of $\sim 40\,R_\odot$ the cool portion of the gas (in blue) corresponding to $\sim$ 6,000 K is nearly twice in the vertical extent with hydro-off. Figure 2.5 also shows that the overall disk temperature is hotter in the hydro-off case, which can be attributed to a larger quantity of gas at greater distances from the equatorial plane that has direct line of sight of the source of the ionizing radiation field originating at the stellar photosphere.

There is a subtle point to keep in mind when comparing the hydro-off and hydro-on cases. For the hydro-off models the disk density in the vertical direction is set *a priori* based on a fixed value for the disk temperature, T_0, in Equation 2.3. The value of T_0 used in this study for γ Cas is 13,500 K and is based on typical density-weighted average temperature of the disk from our models, whereas for the hydro-on case the density is determined from the hydrostatic solution constrained by the value of n and ρ_0. The implication for each of these constraints is that the mass of the disk with the same value of n and ρ_0 is different in the hydro-on and hydro-off cases. As a result, hydro-on models have a total disk mass $\sim$ 20 % less than the hydro-off case (Sigut, McGill, and Jones, 2009). This could certainly account for the larger average disk temperature for the hydro-off model in Figure 2.5 because there is more material distributed out of the plane of the disk where it can be more easily ionized by the stellar radiation field.

We have adopted both the hydro-on and hydro-off models for γ Cas. The infrared excesses are believed to originate in the densest region of the disk near the star and in and near the equatorial plane (Touhami et al., 2010). Therefore, since the hydro-on models provide a self consistent density and temperature distribution, especially important for the densest regions, the hydro-on models are expected to provide a more realistic representation of the physical conditions in the dense gas. However, since many of the previous studies that used the code BEDISK did not employ the hydro-on case we have also presented the results for γ Cas with hydro-off for comparison. We also note that for early-type Be stars, Sigut, McGill, and Jones (2009) found that differences in predicted infrared excesses from hydro-on and hydro-off were quite small for reasonable values of T_0. Rows 1 and 2 of Table 2.4 give our results for γ Cas for the hydro-off and hydro-on cases, respectively. The best fits were obtained from models corresponding to a range in χ^2_ν from the minimum value to the minimum plus 10%. The minimum, maximum, and mean values for both n and ρ_0 for the subset of models

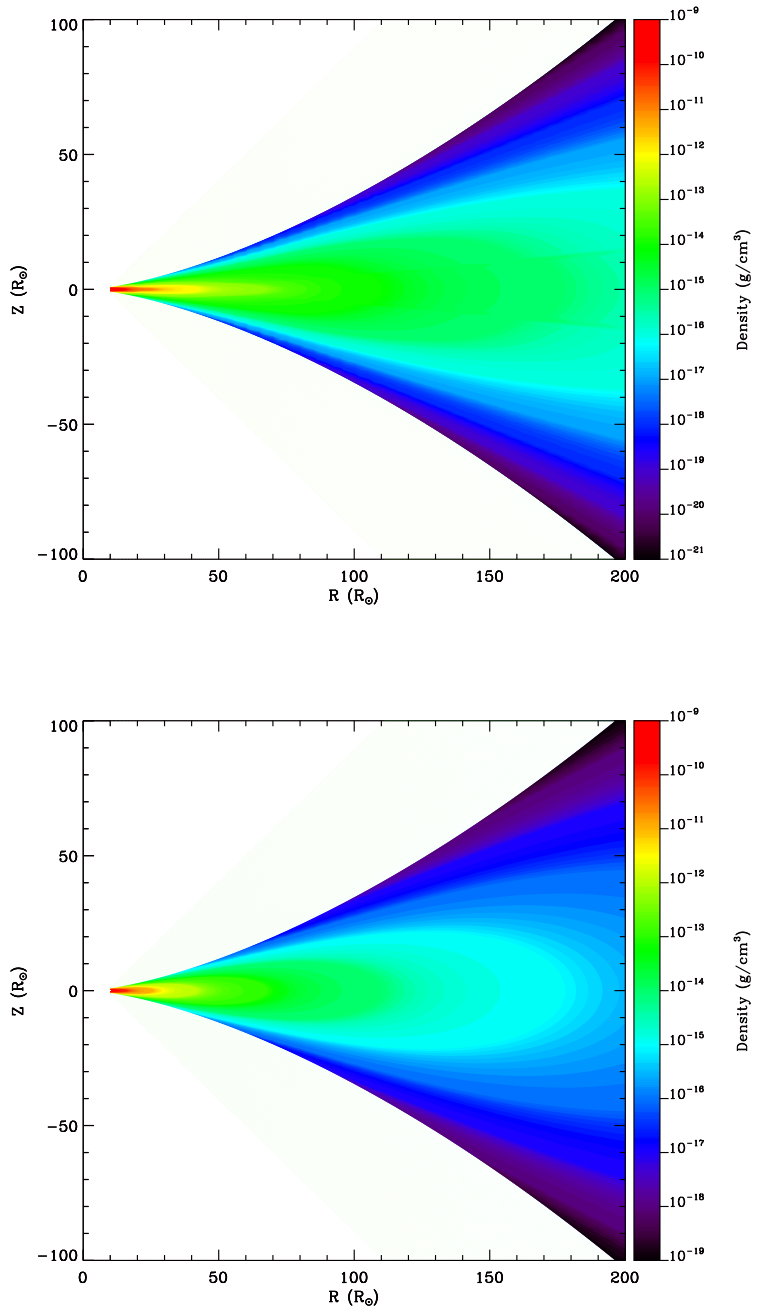

Figure 2.4: Computed density structures for γ Cas with $n = 4.8$ and $\rho_o = 1.0 \times 10^{-9}\,\mathrm{g \cdot cm^{-3}}$, with (upper panel) and without (lower panel) hydrostatic equilibrium enforcement.

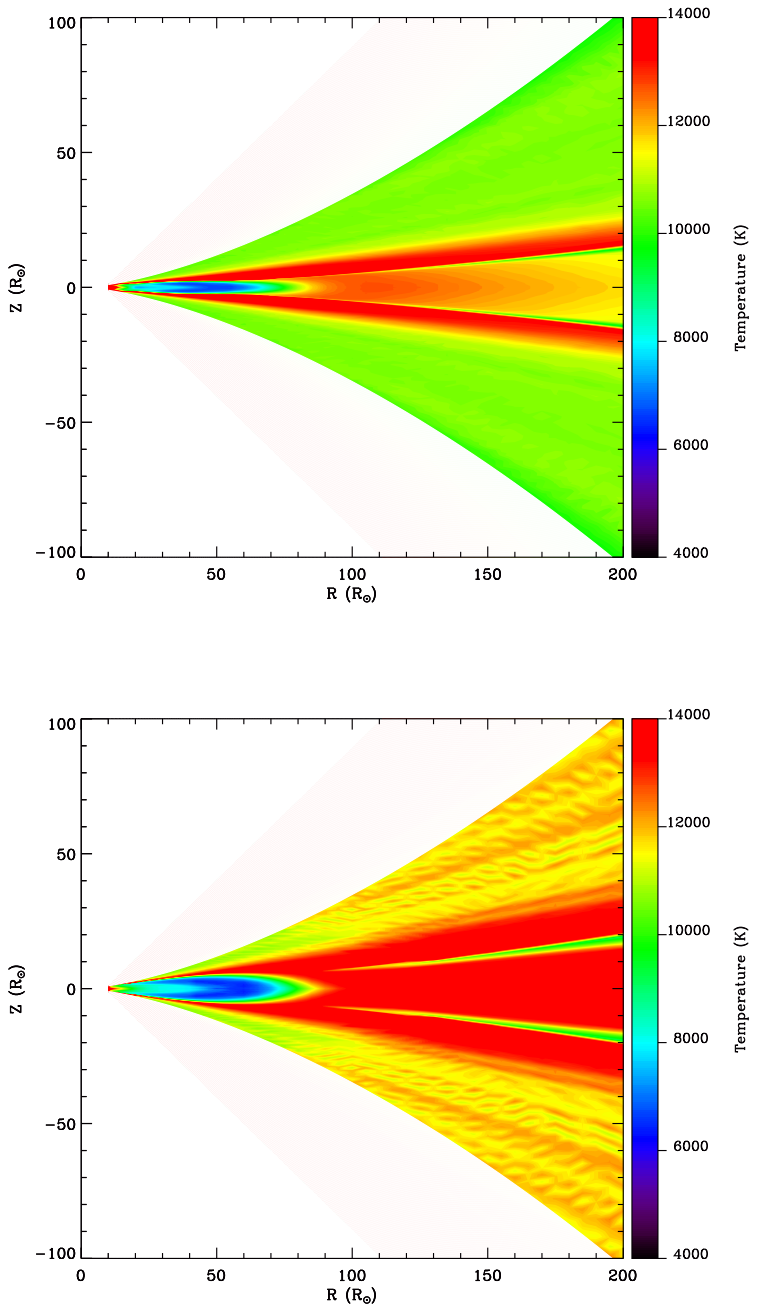

Figure 2.5: Computed temperature structures for γ Cas with $n = 4.8$ and $\rho_o = 1.0 \times 10^{-9}\,\mathrm{g \cdot cm^{-3}}$, with (upper panel) and without (lower panel) hydrostatic equilibrium enforcement.

Table 2.3. Adopted Stellar Parameters

Spectral Type	Stellar Radius ($R_\odot$)	Stellar Mass ($\mathcal{M}_\odot$)	$T_{\rm eff}$ (10^3 K)
B0	10.0	17.0	25.0
B2	5.7	10.9	20.9
B5	3.9	5.9	15.2
B8	3.0	3.8	11.4

All stellar models assumed $\log g = 4.0$ for the central star. Stellar parameters for the B0 the spectral class were taken from Millar and Marlborough (1998). Parameters for B2, B5 and B8 were adapted from Cox (2000).

corresponding to this range in χ^2_ν are also provided in Table 2.4. The numerical model for γ Cas (HD 5394) with the minimum reduced χ^2 for the hydro-on case is displayed in Figure 2.1 with a solid line.

We note that our range of best-fitting model parameters for γ Cas, and our other program stars, each represent an average set of parameters for the density over the time the observations were collected.

2.4.3.2 Spectral Group B2

Five stars in Table 2.1 are of spectral class B2; an additional four are of adequately similar spectral class (B1.5, B2.5, B3) that the B2 spectral class parameters can be used to approximate their characteristics. The stellar parameters used to generate the models were taken or estimated from Cox (2000) and are given in Table 2.3. As previously mentioned, the parameters represent average estimates for a given stellar class and are not an exact match for each star's characteristics. These stars are shown grouped together in Table 2.2 and Table 2.4. The hydro-on case was used to generate models of all the program stars in this group. In total, for this group of stars 220 models were constructed with $1.0 < n < 6.0$ and $1.0 \times 10^{-12} < \rho_0 < 1.0 \times 10^{-8}$ g $\cdot$ cm^{-3}. The subset of models corresponding to a range in χ^2_ν values from the minimum to the minimum plus 10% are shown in Table 2.4. For each of these stars, the solid line in Figure 2.1 corresponds to the hydro-on model with the minimum χ^2 value.

Of all targets, ϕ Per (HD 10516, B2Vpe) has the largest number of calibrated observations (see Table 2.1). The best-fit models have a range in χ^2_ν from 6.81 to 7.16, indicating that the model fit is not especially good. The observations plotted on Figure 2.1 for ϕ Per (HD 10516) show that despite the large number of observations, much of it is centered approximately

Table 2.4. Detailed Model Best Fits

Target	χ^2_ν		n			$\rho_\circ$ (g · cm^{-3})		
	min	max	min	max	mean	min	max	mean
γ Cas[a]	11.24	12.35	2.8	6.2	3.95	3.0e-11	5.0e-09	7.67e-10
γ Cas[b]	13.54	14.83	2.1	6.5	4.13	7.0e-12	3.0e-08	2.25e-09
ϕ Per	6.81	7.16	1.5	2.0	1.83	2.0e-12	3.0e-11	1.73e-11
48 Per[c]	...	...	...	...	...	...	...	...
ζ Tau	4.56	5.00	2.0	2.5	2.10	7.0e-12	7.0e-12	2.08e-11
28 Cyg	1.70	1.85	2.0	6.0	4.35	3.0e-12	1.0e-08	2.31e-09
P Cyg	37.31	40.95	1.0	1.5	1.40	1.0e-12	1.0e-11	7.00e-12
59 Cyg[c]	...	...	...	...	...	...	...	...
υ Cyg	4.58	5.01	2.0	4.0	2.80	8.0e-12	1.0e-08	1.51e-09
EW Lac	1.99	2.10	3.5	4.0	3.88	2.0e-09	1.0e-08	7.25e-09
ψ Per	5.03	5.53	1.2	2.5	1.78	4.0e-11	9.0e-09	8.18e-10
ν Gem[c]	...	...	...	...	...	...	...	...
β Per	12.65	...	3.0	...	...	8.0e-09	...	...
η Tau	0.96	1.03	3.0	3.0	3.0	8.0e-09	1.0e-08	9.00e-09
28 Tau	18.70	20.51	1.0	6.0	3.42	1.0e-12	1.0e-08	1.58e-09
β CMi	1.30	1.40	1.0	5.0	3.24	1.0e-12	5.0e-10	6.26e-11
β Lyr	4.50	4.95	1.0	6.0	3.32	1.0e-12	1.0e-08	2.70e-09

[a]Results for the hydro-off models.; [b]Results for the hydro-on models.; [c]For these three stars there were not enough observations to justify a model fit.

on two values of the spatial frequency which limits the effectiveness of the observations to provide strong model constraints.

The asymmetric disk (Quirrenbach et al., 1997; Vakili et al., 1998) of ζ Tau (HD 37202, B2IV), was best fit by a set of models having smaller values for n. The model corresponding to the lowest value for reduced $\chi^2 = 2.0$ has $n = 2.0$ and $\rho_0 = 7.0 \times 10^{-12}$ g $\cdot$ cm^{-3}. We note that this fit was of higher quality than that of ϕ Per, with reduced $\chi^2 = 4.56$.

P Cyg (HD 193237, B2pe) differs considerably from the other stars in the catalogue. It belongs to a class of stars referred to as luminous blue variable (LBV) stars, which are evolved, massive, and highly luminous stars that demonstrate some type of instability. P Cyg has experienced violent mass-loss events (see Smith and Hartigan (2006)) and as a result our disk models were not expected to fit the more spherically distributed circumstellar material. Consequently, the model fit failed as indicated by the χ^2_ν values; the minimum value is 37. Therefore, we have not plotted the detailed model best fit on Figure 2.1 and only the observations and uniform disk model are shown.

The best χ^2_ν fits within this group of stars are for 28 Cyg (HD 191610, B2.5Ve) and EW Lac (HD 217050, B3IVpe). Interestingly these stars are associated with early-type spectral classes, specifically B2.5 and B3. It is also interesting to note that these two stars all had best-fit models that correspond to n of 2.0 or greater. There are three other stars in this group: 48 Per (HD 25940, B3Ve), 59 Cyg (HD 200120, B2Vne), and υ Cyg (HD 202904, B3IVpe). 48 Per and 59 Cyg had too few observations to constrain our detailed models (see Table 2.1) and as a result further modelling was not completed. Therefore Figure 2.1 shows only the observations and UD fit for this star. Also, υ Cyg did not have good χ^2_ν values and further discussion is provided in Section 2.5.

2.4.3.3 Spectral Group B5

Another set of models using the parameters for spectral class B5 was generated and compared to the observations for ψ Per (HD 22192, B5Ve). In total, there were 285 models constructed with $1.2 < n < 6.0$ and $6.0 \times 10^{-12} < \rho_0 < 1.0 \times 10^{-8}$ g $\cdot$ cm^{-3}. The adopted stellar parameters and the results for the subset of the preferred models are listed in Table 2.3 and Table 2.4, respectively for the star ψ Per. For ν Gem there were only three observations in our archival set, therefore, analogous to the stars 48 Per and 59 Cyg, only the observations and UD fit are presented in Figure 2.1.

2.4.3.4 Spectral Group B8

Finally, a set of models were produced for the five remaining late type stars using the B8 stellar parameters listed in Table 2.3 over a range of $1.0 < n < 6.0$ and $1.0 \times 10^{-12} < \rho_0 < 1.0 \times 10^{-8}$ g $\cdot$ cm^{-3}. Again, these stars are shown grouped together by the horizontal lines in Table 2.2 and Table 2.4. Table 2.4 provides the range of model parameters for our preferred subset of models and the solid line in Figure 2.1 shows the model corresponding to the minimum χ^2_ν.

For β Lyr (HD 174638, B7e+), although the quality of the fit was relatively good with a minimum χ^2_ν of 4.5, it needs to be emphasized that this star is an interacting binary (Schmitt et al., 2009; Zhao et al., 2008). Therefore, the results of this study need to be approached cautiously and further analysis is needed to get a complete picture of this system. In fact, the subset of models that correspond to within 10% of the minimum χ^2_ν which span the entire range of n investigated. For β Per (HD 19356, B8V), a well known Algol type eclipsing binary, we were not able to find a good fit as indicated by the minimum χ^2_ν of 12.65. For the other stars in this spectral range, a rather poor fit was obtained for 28 Tau (HD 23962, B8IVe), while good fits were found for η Tau (HD 23630, B7III) and β CMi (HD 58715, B8Ve).

2.5 Discussion

Our study includes objects in common with other work presented in the literature and it is illuminating to compare the results presented here with other investigations. Similar work was performed by Gies et al. (2007) using the CHARA array to observe Be stars in the K′-band. We have three stars in common with their study: γ Cas, ϕ Per, and ζ Tau. For γ Cas we obtained quite a large range in model parameters for our subset of best-fit models. Gies et al. (2007) considered two different models in their analysis, a single star model and a binary system. They obtained a value for n of 2.70 and 2.65 and ρ_0 of 7.24×10^{-11} g $\cdot$ cm^{-3} and 6.61×10^{-11} g $\cdot$ cm^{-3} for the single and binary solutions, respectively. These values fall within the range of our best-fit subset of models for γ Cas. However, Table 2.4 shows that for γ Cas, with both hydro-off and hydro-on, the set of preferred models is quite large and consists of a large range in both n and ρ_0. This could be due to several factors. The χ^2 values indicate that the fit is not ideal. The assumption that the disk is symmetric about the mid-plane may not be fully appropriate for γ Cas. We note that the fits obtained by Gies et al. (2007) with χ^2_ν of 24.3 and 24.0 are also not of high quality which may be further proof that an axisymmetric disk is not a good representation for γ Cas. Also recall that we found some evidence for ellipticity for γ Cas (see Section 2.4.2). In addition, as shown in Figure 2.1 most of the observations were obtained at only a few spatial frequencies which places limits on how

well the numerical models can be constrained.

For ϕ Per our detailed model fits were much better and the agreement with Gies et al. (2007) is excellent. Gies et al. (2007) obtained a value for n of 1.80 and 1.76 and ρ_0 of 1.20×10^{-11} g $\cdot$ cm^{-3} and 1.05×10^{-11} g $\cdot$ cm^{-3} for the single and binary solutions, respectively. We find $1.5 < n < 2.0$ and $2.0 \times 10^{-12} < \rho_0 < 3.0 \times 10^{-11}$ g $\cdot$ cm^{-3} for this star. It is interesting that we both obtain a small value of n based on the infrared observations. This suggests that the density distribution, at least near the star, falls off quite slowly.

Finally for ζ Tau, Gies et al. (2007) obtained a values for n of 3.14 and 3.19 and ρ_0 of 1.95×10^{-10} g $\cdot$ cm^{-3} and 1.86×10^{-10} g $\cdot$ cm^{-3} for the single and binary solutions, respectively. We find smaller values, $2.0 < n < 2.5$, and correspondingly smaller values of ρ_0 (see Table 2.4).

For the other early type stars reasonable fits were obtained for program stars with the exception of 48 Per which we were unable to model due to insufficient observations.

We also have a number of stars in common with the work of Waters, Coté, and Lamers (1987) who used simple disk models to study the far infrared characteristics using IRAS (Infrared Astronomical Satellite). Although the observations were obtained at a different epoch, it is interesting to compare our results to theirs. Waters, Coté, and Lamers (1987) obtained $2 < n < 3.5$ for their range of the power law fall-off. Their values for ρ_0 generally agree with our findings, but Waters, Coté, and Lamers (1987) values are typically at the lower end of our range. Perhaps this is not surprising because Waters, Coté, and Lamers (1987) uses a contant opening angle of 15^0 for their disk models with the density at a given radial distance remaining constant along radial arcs above and below the equatorial plane. Recall that in our models, the disk density falls off exponentially perpendicular to the equatorial plane. Therefore, we require higher values of ρ_0 to have an equivalent amount of gas within the disk.

2.6 Conclusions

We have assembled a collection of uniform disk and numerical disk models for comparison with K-band interferometric observations for sixteen Be stars spanning spectral types from Bo to B8. Uniform disk models for sixteen targets were fitted to K-band archival observations from the Palomar Testbed Interferometer. We also determined the disk density distribution using numerical models constructed with the non-LTE radiative code Bedisk (Sigut and Jones, 2007) for the remaining fifteen stars. Our collection of numerical models has the distinction of being thermally balanced in addition to having been generated with solar chemical composition. This analysis allowed us to select a range of preferred model parameters by a comparison to the interferometric observations based on standard χ^2 tests for all but three of the fifteen stars (see Table 2.4). We present a range of best-fitting model parameters for our

program stars, representing the average density over the time the observations were collected for each star. Due to the intrinsic variability of Be stars and some of our other program stars, our range of best-fit density parameters may only be appropriate for the time over which the PTI observations were obtained.

For P Cyg (HD 193237), which possesses a spherical wind, our disk model fits failed and for the three other stars, 48 Per (HD 25940), 59 Cyg (HD 200120) and ν Gem (HD 45542), there were insufficient values to constrain our detailed models.

By combining the results from all our targets, we find best-fit models corresponding to model input parameters that ranged substantially in value with $1.0 < n < 6.5$ and $1.0 \times 10^{-12} < \rho_0 < 3.0 \times 10^{-8}$ g $\cdot$ cm^{-3}. A simple average value of n over all of our program stars for our preferred models is 3.03 ± 0.94. This result is in good agreement with other investigations of Be star disks in the infrared regime (Gies et al., 2007; Waters, Coté, and Lamers, 1987).

Silaj et al. (2010) also used the BEDISK code to construct Hα profiles for comparison with observations of 69 Be stars. Although the Hα emitting region samples a larger volume of the disk, it is instructive to compare our results with Silaj et al. (2010). Analogous to our findings, Silaj et al. (2010) determined that a large range of n and ρ_0 was required to produce suitable profiles for their program stars. Interestingly, their values for n were strongly peaked at 3.5 (see Silaj et al. (2010) figure 7). This value agrees quite well with our simple average of $n = 3.03$ from our subset of preferred models.

For some of our program stars we obtain preferred models that include upper limits of ρ_0 that are quite large. In fact, as discussed in Cranmer (2009), the largest values coincide with typical values associated with stellar photospheres. These large densities near the star in the equatorial region are consistent with the suggestion by Koubsky et al. (1997) that Be star disks begin as an optically thick extension of the star that eventually develops into a disk. Future work will be necessary to determine the generality of this statement.

References

Balan, A., Tycner, C., Zavala, R. T., et al. (2010). *AJ* 139, pp. 2269–2278. DOI: 10.1088/0004-6256/139/6/2269. arXiv: 1004.0376 [astro-ph.SR].

Boden, A. F., Colavita, M. M., van Belle, G. T., et al. (1998). In: *Society of Photo-Optical Instrumentation Engineers (SPIE) Conference Series*. Ed. by R. D. Reasenberg. Vol. 3350. Society of Photo-Optical Instrumentation Engineers (SPIE) Conference Series, pp. 872–880.

Boden, A. F., Koresko, C. D., van Belle, G. T., et al. (1999). *ApJ* 515, pp. 356–364. DOI: 10.1086/307030. eprint: arXiv:astro-ph/9811029.

Carciofi, A. C., Okazaki, A. T., Le Bouquin, J.-B., et al. (2009). *A & A* 504, pp. 915–927. DOI: 10.1051/0004-6361/200810962. arXiv: 0901.1098 [astro-ph.SR].

Carciofi, A. C., Bjorkman, J. E., Otero, S. A., et al. (2012). *ApJL* 744, L15, p. L15. DOI: 10.1088/2041-8205/744/1/L15. arXiv: 1112.0053 [astro-ph.SR].

Colavita, M. M. (1999). *PASP* 111, pp. 111–117. DOI: 10.1086/316302. eprint: arXiv:astro-ph/9810462.

Colavita, M. M., Wallace, J. K., Hines, B. E., et al. (1999). *ApJ* 510, pp. 505–521. DOI: 10.1086/306579. eprint: arXiv:astro-ph/9810262.

Cox, A. N. (2000). New York: AIP Press; Springer.

Cranmer, S. R. (2009). *ApJ* 701, pp. 396–413. DOI: 10.1088/0004-637X/701/1/396. arXiv: 0906.2772 [astro-ph.SR].

de Groot, M. (1969). *Bull. Astron. Inst. Netherlands* 20, p. 225.

Gies, D. R., Bagnuolo Jr., W. G., Baines, E. K., et al. (2007). *ApJ* 654, pp. 527–543. DOI: 10.1086/509144. eprint: arXiv:astro-ph/0609501.

Goodricke, J. (1783). *Royal Society of London Philosophical Transactions Series I* 73, pp. 474–482.

Harmanec, P. (2002). *Astronomische Nachrichten* 323, pp. 87–98. DOI: 10.1002/1521-3994(200207)323:2<87::AID-ASNA87>3.0.CO;2-P.

Harmanec, P., Habuda, P., Štefl, S., et al. (2000). *A & A* 364, pp. L85–L88. eprint: arXiv:astro-ph/0011516.

Hubert, A. M. and Floquet, M. (1998). *A & A* 335, pp. 565–572.

Jaschek, M., Slettebak, A., and Jaschek, C. (1981). Be Star Newsletter.

Jones, C. E., Sigut, T. A. A., and Marlborough, J. M. (2004). *MNRAS* 352, pp. 841–846. DOI: 10.1111/j.1365-2966.2004.07970.x.

Jones, C. E., Tycner, C., Sigut, T. A. A., et al. (2008). *ApJ* 687, pp. 598–607. DOI: 10.1086/591726. arXiv: 0807.1515.

Jones, C. E., Molak, A., Sigut, T. A. A., et al. (2009). *MNRAS* 392, pp. 383–390. DOI: 10.1111/j.1365-2966.2008.14064.x.

Koubsky, P., Harmanec, P., Kubat, J., et al. (1997). *A & A* 328, pp. 551–564.

Kurucz, R. L. (1993).

Lee, U., Osaki, Y., and Saio, H. (1991). *MNRAS* 250, pp. 432–437.

Martayan, C., Baade, D., and Fabregat, J. (2010). *A & A* 509, A11, A11. DOI: 10.1051/0004-6361/200911672. arXiv: 0909.2303 [astro-ph.CO].

McSwain, M. V. and Gies, D. R. (2005). *ApJS* 161, pp. 118–146. DOI: 10.1086/432757. eprint: arXiv:astro-ph/0505032.

Millar, C. E. and Marlborough, J. M. (1998). *ApJ* 494, p. 715. DOI: 10.1086/305229.

Miroshnichenko, A. S., Bjorkman, K. S., and Krugov, V. D. (2002). *PASP* 114, pp. 1226–1233. DOI: 10.1086/342766.

Mozurkewich, D., Johnston, K. J., Simon, R. S., et al. (1991). *AJ* 101, pp. 2207–2219. DOI: 10.1086/115843.

Perryman, M. A. C., Lindegren, L., Kovalevsky, J., et al. (1997). *A & A* 323, pp. L49–L52.

Poeckert, R. and Marlborough, J. M. (1978). *ApJ* 220, pp. 940–961. DOI: 10.1086/155984.

Porter, J. M. (1996). *MNRAS* 280, pp. L31–L35.

Porter, J. M. and Rivinius, T. (2003). *PASP* 115, pp. 1153–1170. DOI: 10.1086/378307.

Quirrenbach, A., Bjorkman, K. S., Bjorkman, J. E., et al. (1997). *ApJ* 479, 477 (Q97). DOI: 10.1086/303854.

Rivinius, T., Štefl, S., and Baade, D. (2006). *A & A* 459, pp. 137–145. DOI: 10.1051/0004-6361:20053008.

Schaefer, G. H., Gies, D. R., Monnier, J. D., et al. (2010). *AJ* 140, pp. 1838–1849. DOI: 10.1088/0004-6256/140/6/1838. arXiv: 1009.5425 [astro-ph.SR].

Schmitt, H. R., Pauls, T. A., Tycner, C., et al. (2009). *ApJ* 691, pp. 984–996. DOI: 10.1088/0004-637X/691/2/984. arXiv: 0801.4772.

Sigut, T. A. A. (2011). In: *IAU Symposium*. Ed. by C. Neiner, G. Wade, G. Meynet, et al. Vol. 272. IAU Symposium, pp. 426–427. DOI: 10.1017/S1743921311011045.

Sigut, T. A. A. and Jones, C. E. (2007). *ApJ* 668, pp. 481–491. DOI: 10.1086/521209. arXiv: 0706.4036.

Sigut, T. A. A., McGill, M. A., and Jones, C. E. (2009). *ApJ* 699, pp. 1973–1981. DOI: 10.1088/0004-637X/699/2/1973. arXiv: 0905.1295 [astro-ph.SR].

Silaj, J., Jones, C. E., Tycner, C., et al. (2010). *ApJS* 187, pp. 228–250. DOI: 10.1088/0067-0049/187/1/228.

Smith, B. J., Price, S. D., and Baker, R. I. (2004). *ApJS* 154, pp. 673–704. DOI: 10.1086/423248. eprint: astro-ph/0406177.

Smith, N. and Hartigan, P. (2006). *ApJ* 638, pp. 1045–1055. DOI: 10.1086/498860. eprint: arXiv:astro-ph/0510836.

Struve, O. (1931). *ApJ* 73, p. 94. DOI: 10.1086/143298.

Touhami, Y., Richardson, N. D., Gies, D. R., et al. (2010). *PASP* 122, pp. 379–395. DOI: 10.1086/652009. arXiv: 1003.5876 [astro-ph.SR].

Townsend, R. H. D., Owocki, S. P., and Howarth, I. D. (2004). *MNRAS* 350, pp. 189–195. DOI: 10.1111/j.1365-2966.2004.07627.x. eprint: arXiv:astro-ph/0312113.

Tycner, C., Hajian, A. R., Armstrong, J. T., et al. (2004). *AJ* 127, pp. 1194–1203. DOI: 10.1086/381068.

Tycner, C., Lester, J. B., Hajian, A. R., et al. (2005). *ApJ* 624, pp. 359–371. DOI: 10.1086/429126. eprint: astro-ph/0501552.

Tycner, C., Gilbreath, G. C., Zavala, R. T., et al. (2006). *AJ* 131, pp. 2710–2721. DOI: 10.1086/502679. eprint: astro-ph/0602087.

Tycner, C., Jones, C. E., Sigut, T. A. A., et al. (2008). *ApJ* 689, pp. 461–470. DOI: 10.1086/592097. arXiv: 0807.3971.

Vakili, F., Mourard, D., Stee, P., et al. (1998). *A & A* 335, pp. 261–265.

van Belle, G. T. and van Belle, G. (2005). *PASP* 117, pp. 1263–1270. DOI: 10.1086/449603. eprint: arXiv:astro-ph/0508266.

van Belle, G. T., van Belle, G., Creech-Eakman, M. J., et al. (2008). *ApJS* 176, pp. 276–292. DOI: 10.1086/526548. arXiv: 0711.4194.

van Leeuwen, F. (2007). *A & A* 474, pp. 653–664. DOI: 10.1051/0004-6361:20078357. arXiv: 0708.1752.

Waters, L. B. F. M., Coté, J., and Lamers, H. J. G. L. M. (1987). *A & A* 185, pp. 206–224.

Zavala, R. T., Hummel, C. A., Boboltz, D. A., et al. (2010). *ApJL* 715, pp. L44–L48. DOI: 10.1088/2041-8205/715/1/L44. arXiv: 1005.0626 [astro-ph.SR].

Zhao, M., Gies, D., Monnier, J. D., et al. (2008). *ApJL* 684, pp. L95–L98. DOI: 10.1086/592146. arXiv: 0808.0932.

Zorec, J. and Briot, D. (1997). *A & A* 318, pp. 443–460.

"There is a crack in everything.
That's how the light gets in."

Leonard Cohen, "Anthem"

3

48 Persei

3.1 Introduction

Classical Be stars are distinguished by the presence of Balmer emission lines in their spectra. As first proposed by Struve (1931), the Balmer lines are attributed to an equatorial disk of material surrounding the star (Rivinius, Carciofi, and Martayan 2013; Porter and Rivinius 2003). Other defining characteristics of Be stars include linearly polarized light, infrared and radio continuum excess due to radiative processes within the disk and rapid stellar rotation. As well, these systems often exhibit variability over a range of time scales (for details, see the recent review by Rivinius, Carciofi, and Martayan (2013)).

The classical B-emission (Be) star 48 Per (HD 25940, HR 1273, spectral type B3V) is well studied and located at a distance of 146 pc*. Slettebak (1949) originally classified this star as pole-on but the appearance of doubly peaked Hα profiles reported by Burbidge and Burbidge (1953) led Ruusalepp (1982) to suggest that it has an inclination of 34° to 40°. Since then, the value of the inclination for this system has remained contentious. The reported changes in the spectral line shape and well as other documented changes in brightness (see Tur, Goraya, and Chaubey (1987) and references therein) point to periods of variability exhibited by 48 Per. However, we note that 48 Per was particularly stable over the time our observations were acquired. See the next Section for more detail.

Studies by Quirrenbach et al. (1997) and Delaa et al. (2011) combined interferometry with

B. J. Grzenia, C. E. Jones, C. Tycner, T. A. A. Sigut. A version of this chapter was submitted to AAS Journals.

*based on Hipparcos parallaxes; see van Leeuwen (2007)

other observables for 48 Per, and their work is ideally suited to detailed comparison with the results presented here. The Quirrenbach et al. (1997) study, hereafter 'Q97', obtained interferometric observations with the Mark III Interferometer (Shao et al., 1988) as well as spectropolarimetric observations. Although Mark III has since been decommissioned, it was a predecessor to the instrument used for this study, the Navy Precision Optical Interferometer (NPOI; see Armstrong et al. 1998 for a technical description), and the two instruments share some characteristics. 48 Per was observed with six distinct interferometric baselines resulting in a set of 46 observations in the study by Q97. Through modelling they were able to place bounds on the size and inclination of the Hα emitting region. The orthogonal position angles obtained via interferometry and polarimetry demonstrated conclusively (and for the first time) that Be star disks could not be both geometrically and optically thick. More recently, Delaa et al. (2011) or 'D11', obtained data from the Center for High Angular Resolution Astronomy (CHARA) interferometer (ten Brummelaar et al., 2005) and also utilized spectroscopic measurements from the attached VEGA instrument (Mourard et al., 2009) to constrain estimates for the size of the Hα emission region for 48 Per. Q97 confirm the nearly pole-on orientation found by Slettebak (1949) by determining a minimum inclination of 27° consistent with an inclination of 30 $\pm$10° by D11.

The overall progression of this study is as follows; in Section 3.2 we detail our observational program, and Section 3.3 provides an overview of the code used to calculate the theoretical disk models, along with the data pipeline we developed to analyze the model and observational data. The results of this analysis are presented in Section 3.4. Finally, Section 3.5 discusses our findings along with a comparison to other work and implications.

3.2 Observation Program

Our observations of 48 Per were obtained at the Navy Precision Optical Interferometer (NPOI), located near Flagstaff, AZ, USA. The NPOI has an unvignetted aperture of 35 cm with an effective aperture for the observations of 12.5 cm set by the diameter of the feed system optics. See Armstrong et al. (1998) and Hutter et al. (2016) for additional technical descriptions of this facility. Typically, observations from up to five baselines are obtained simultaneously; for this study, baseline lengths ranged from 18.9 m to 64.4 m. A total of 291 observations of 48 Per were made at NPOI in the autumn of 2006. The specific dates of observation are shown in Table 3.1, and Table 3.2 provides details such as time, (u, v)-space coordinates, and baseline specifier for each individual observation. Table 3.2 is published in its entirety in a machine readable format in Appendix A. Figure 3.1 shows the (u, v) plane coverage acquired at NPOI; individual observations are represented by open circles and the arcs are possible

Table 3.1. Dates of NPOI Observations

Dates	Data Points
2006 Nov 07	18
2006 Nov 08	18
2006 Nov 09	26
2006 Nov 10	10
2006 Nov 11	14
2006 Nov 14	1
2006 Nov 15	10
2006 Nov 16	22
2006 Nov 17	42
2006 Nov 18	24
2006 Nov 20	36
2006 Nov 21	42
2006 Nov 22	24
2006 Nov 23	4

coverage from the meridian 6^h east (dashed lines) and from the meridian to 6^h west (solid lines). The blue, red, green, violet and light blue colours correspond to data from baselines of 18.9, 22.2, 29.5, 51.6, and 64.4 m, respectively. These observations utilized a 150-Å bandpass centred on Hα (6563 Å). Figure 3.2 shows interferometric observations, depicted as solid circles, expressed as a normalized Fourier power V^2 (i.e., the interferometric visibility). The solid black curves each correspond to one specific baseline and depict changes in spatial frequency resulting from diurnal motion. The dotted lines are the minor and major axis of an elliptical Gaussian fit to the data and the dashed line represents the central star modelled with a uniform disk of 0.306 mas. The colours correspond to the baselines as described for Figure 3.1 except the additional orange colour is also for the baseline length of 51.6 m, the same as the violet colour. In this case, the data obtained from this particular baseline was collected from two different spectrographs. These two sets are unique and show the consistency between the outputs from the beam combiner. In Figure 3.1 only violet is shown because these two sets from this baseline sample the same (u, v) spatial coordinates.

Contemporaneous Hα observations were obtained with the Solar Stellar Spectrograph (SSS), an echelle spectrograph attached to the John S. Hall Telescope at Lowell Observatory (Tycner et al. 2006; Hall et al. 1994). The line is singly peaked, consistent with a disk viewed

Table 3.2. Interferometric NPOI Observations of 48 Per (partial)

JD-2,450,000	u (m)	v (m)	V^2 (arbitrary)	Baseline[1]
4046.749	17.189	−21.882	0.834 ± 0.026	AC-AE
4046.749	−29.224	0.422	0.849 ± 0.033	AC-AW
4046.782	21.140	−18.991	0.854 ± 0.062	AC-AE
4046.782	−30.994	−4.121	0.893 ± 0.128	AC-AW
4046.815	24.338	−15.402	0.793 ± 0.040	AC-AE

Table 3.2 is included as Appendix A in its entirety in a machine readable format. A portion is shown here for guidance regarding its form and content. [1]The baselines AC-AE, AC-AW, AW-W7, AC-W7, AE-W7 correspond to lengths of 18.9, 22.2, 29.5, 51.6, and 64.4 m, respectively.

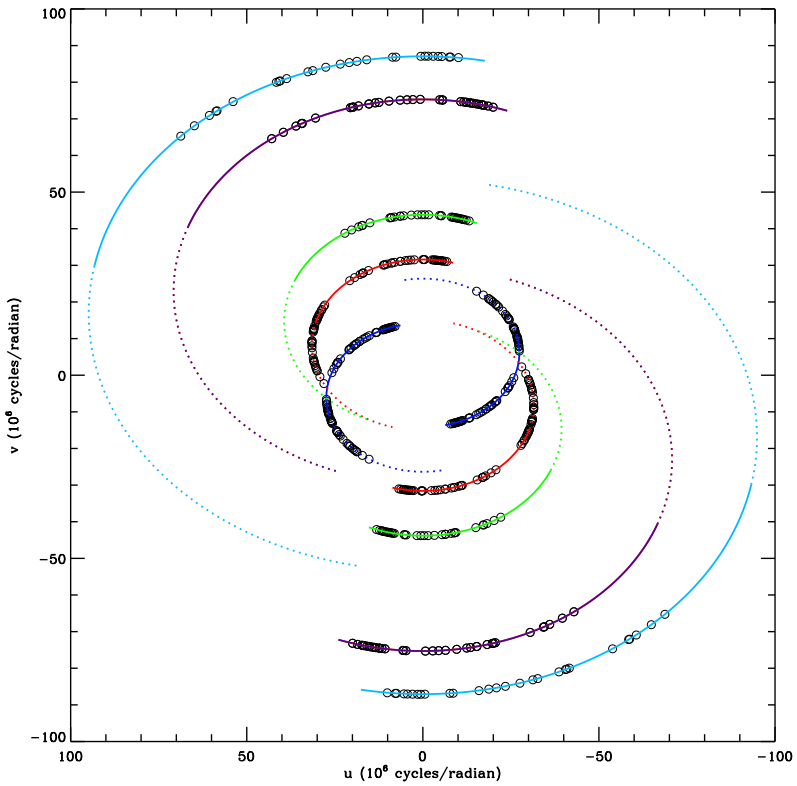

Figure 3.1: Sky coverage in the (u, v) plane for 48 Per. The circles correspond to data points obtained at five unique baselines at the dates listed in Table 3.1. The arcs represent possible coverage from the meridian 6^h east (dashed lines) and from the meridian to 6^h west (solid lines). The blue, red, green, violet and light blue colours correspond to data from baselines of 18.9, 22.2, 29.5, 51.6, and 64.4 m, respectively.

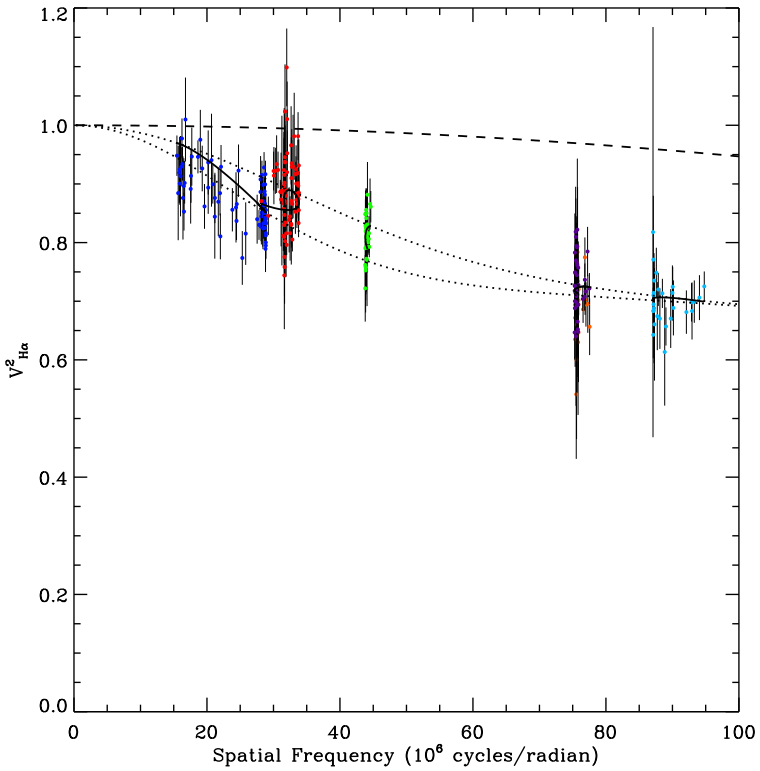

Figure 3.2: Observed interferometric visibility versus spatial frequency for 48 Per. The dotted lines represent the major and minor axes of the disk system modelled with of elliptical Gaussian fit, GD, to the data as seen on the sky; the dashed line represents the central star with a uniform disk, UD, diameter of 0.306 mas. The colours correspond to the baselines as described for Figure 3.1 except the additional orange colour is also for the baseline length of 51.6 m, the same as the violet colour. The solid black curves each correspond to one specific baseline and depict changes in spatial frequency resulting from diurnal motion.

more pole-on to mid inclinations. Over the course of our observing program the Hα emission line remained remarkably stable. In fact, Hα spectra acquired on 2006 Nov 1 and on 2006 Dec 9 that bracket the time frame of our interferometric data are indistinguishable, with Hα equivalent widths of 28.2 and 28.1 Å, respectively. The observed Hα spectra (blue circles) obtained on 2006 Nov 1 is shown in Figure 3.3 along with a sample of our best-fitting models based on our figure-of-merit ($\mathcal{F}$) analysis. See the next section for details about our Hα spectral fitting procedure.

3.3 Modelling

3.3.1 Data Pipeline: Bedisk, Beray and 2dDFT

Bedisk was developed by Sigut and Jones (2007). It is a non-local thermodynamic equilibrium (non-LTE) modelling code which calculates self-consistent temperature distributions based on the corresponding density distribution and level populations within the disk (Sigut and Jones, 2007). For the present study, the density structure within the circumstellar disk was described by a power law:

$$\rho(R, Z) = \rho_\circ \left(\frac{R_*}{R}\right)^n \exp\left[-\left(\frac{Z}{H}\right)^2\right], \tag{3.1}$$

where $\rho_\circ$ is the density at the disk-star boundary and Z is the distance from the plane of the disk measured normal to the disk. H is the vertical scale height of the disk measured perpendicular to the disk. We assume that H is in approximate vertical hydrostatic equilibrium with a temperature $0.6T_{\mathit{eff}}$ of the star; see Sigut, McGill, and Jones (2009) for details.

The temperature and density distributions as well as level populations calculated with Bedisk are used as inputs to Beray (Sigut, 2011). The Bedisk-Beray sequence is used to obtain a model intensity image of the disk system on the plane of the sky. Beray calculates a formal solution of the radiative transfer equation through the disk along approximately 10^5 rays from the observer's line of sight. The computational region extends from the photosphere to a distance (in terms of stellar radii) specified by the user. For this study, models were computed for disk sizes of 6.0, 12.5, 25.0 and $50.0R_*$. Interferometry data produces a series of visibilities as a function of spatial frequency, which is itself a representation of the interferometric baseline (Thompson, Moran, and Swenson, 1986). The 2D Discrete Fourier Transform (2dDFT) code takes the 2-dimensional discrete Fourier transform of the Beray image and produces V^2 as a function of spatial frequency. The code then compares the model to a set of observations specified by the user and estimates goodness-of-fit based on a reduced

Table 3.3. Stellar Parameters Adopted for 48 Per.

Parameter	Value
M ($\mathcal{M}_\odot$)	7.6
R ($R_\odot$)	4.8
L ($L_\odot$)	2580
T_{eff} (K)	18800
$\log g$	4.0
Distance (pc)	146[a]
Angular Diameter (mas)	0.306[b]

Notes: [a]parallax distance based on van Leeuwen (2007); [b]calculated from spectral type and distance.

χ^2 (χ^2_ν) test. We note that these same codes were previously used by Sigut et al. (2015) to model the Be star *o* Aquarii. In addition to determining the density distribution within the disk, our Fourier analysis is used to calculate the system's angular dimensions on the sky, the position angle of the system, the disk mass and corresponding angular momentum.

3.3.2 Model Parameters

The spectral type B3Ve was adopted for 48 Per, which is consistent across the two comparison studies of Q97 and D11, and with the Bright Star Catalog (Hoffleit and Jaschek, 1982). Further, this is in agreement with examples in the literature dating back over the past six decades (see, for example, Butler and Seddon (1960) or Borgman (1960)). The parameters for the B3Ve type were determined by linear interpolation from Cox 2000 and are provided in Table 3.3.

3.3.3 Computational Grid

The parameter space was chosen to be consistent with n and ρ_0 values that would be expected for Be star disks based on historical predictions (Waters, 1986) and on contemporary studies (see, for example, section 5.1.3 of Rivinius, Carciofi, and Martayan (2013) for a summary of recent results in the literature). As mentioned above our models were computed for a range of disk size from 6.0 to 50.0R_*. Other model parameters were varied as follows; $1.5 \leq n \leq 4.0$ in steps of 0.25, $1.0 \times 10^{-13} \leq \rho_0 \leq 2.5 \times 10^{-10}$ g $\cdot$ cm^{-3} in increments of 2.5 over each order of magnitude, with inclinations ranging from 20° to 65° in steps of 5°.

3.4 Results

3.4.1 Hα Spectroscopy

Our Hα line profile models were compared directly to the observed spectra obtained on 2006 Nov 1. Our models spectra were convolved with a Gaussian of FWHM of 0.656 Å to match the resolution of 10^4 of the observed spectra. For each comparison, the percentage difference between the observed line and model prediction were averaged over the line from 6555 Å to 6570 Å to determine figure-of-merit value, $\mathcal{F}$, computed by,

$$\mathcal{F} = \frac{1}{N}\sum_i w_i \frac{\left|F_i^{obs} - F_i^{mod}\right|}{F_i^{obs}}, \tag{3.2}$$

with

$$w_i = \frac{F_i^{obs}}{F_c^{obs}} - 1, \tag{3.3}$$

where F_{mod} and F_c are the model flux and the continuum flux, respectively. Finally $\mathcal{F}$ was normalized by the best-fit, i.e. $\mathcal{F}/\mathcal{F}_{min}$, so that in our analysis the model best-fit has a value of 1. Equation 3.3 emphasizes the fit in the core and peak of the line while minimizing differences in the wings. This technique of matching the core of the line was found to be useful in a previous study for *o* Aquarii (Sigut et al., 2015). Overall, our model spectra were too weak in the wings similar to the results of D11 and Sigut et al. (2015). Figure 3.3 shows the four best-fitting spectra within 20% of the best-fitting model along with the observed line. The density parameters for each model are listed in the legend in the upper right of the figure along with the value of $\mathcal{F}$. The parameters in brackets in the legend correspond to ρ_0 in $g \cdot cm^{-3}$, n, disk size in R_*, and inclination angle. The parameters corresponding to our best-fit are $(\rho_0, n, R_{disk}, i) = 5.0\times10^{-12}\, g \cdot cm^{-3}, 2.0, 50R_*, 45^\circ$ (blue line on Figure 3.3). The average inclination for the four best-fit models is $46 \pm 5^\circ$.

The Hα line observed for 48 Per has an equivalent width (EW) of 28.2 Å and exhibits the singly-peaked profile we expect to see from a disk system with low to moderate inclinations. Q97 estimated the lower limit for the inclination angle of 48 Per to be 27°. D11 determined a best-fit inclination from their kinematic model of $30 \pm 10^\circ$. Our model spectra for inclinations at 30° and lower did not reproduce the observed line shape well. The model Hα lines were too narrow and the wings of the line were too weak. Considering a slightly larger set of 16 best-fitting models, corresponding to $\mathcal{F}$ within $\sim$ 30% of the best-fit, there are 3 models with an inclination of 35°, and the remainder in this set have inclinations between 40° and 55° with only one model at this highest value. The average inclination of this set is $47 \pm 7^\circ$. The

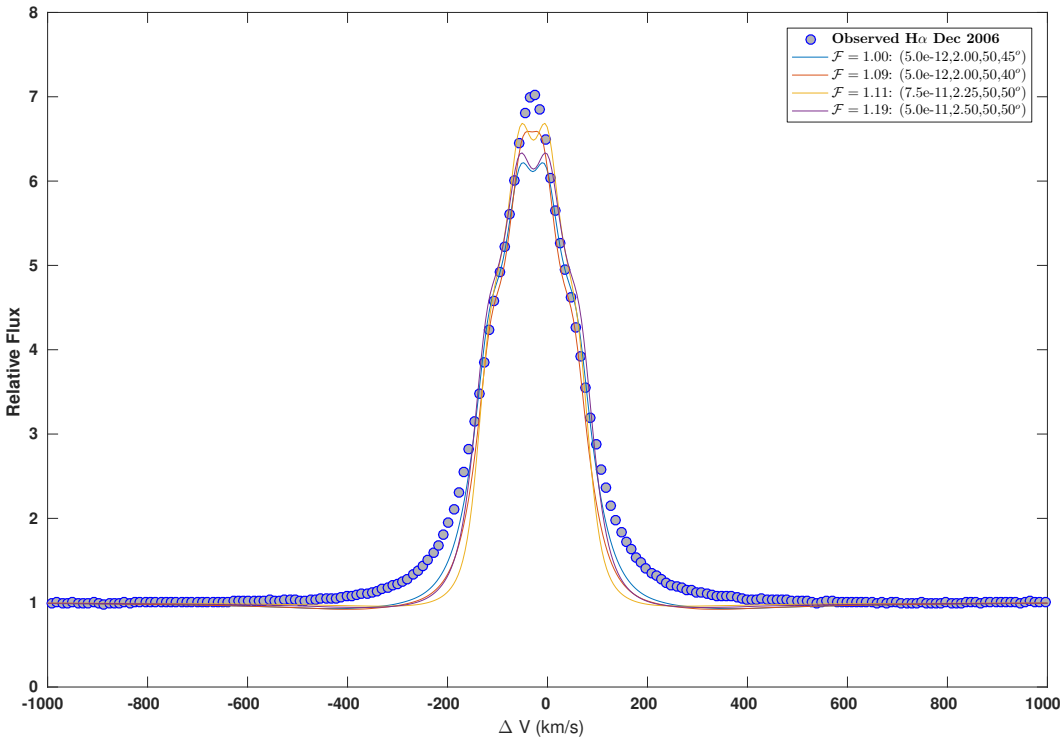

Figure 3.3: The Hα line profile for 48 Per (blue circles) obtained on 2006 Nov 1 (equivalent width 28.2 Å) is shown with a sample of our best fitting models with (ρ_o, n, R_{disk}, i)= 5.0×10^{-12} g $\cdot$ cm^{-3}, 2.0, 50R_*, 45° (blue line), (ρ_o, n, R_{disk}, i) = 5.0×10^{-12} g $\cdot$ cm^{-3}, 2.0, 50R_*, 40° (red line), (ρ_o, n, R_{disk}, i)= 7.0×10^{-11} g $\cdot$ cm^{-3}, 2.25, 50R_*, 50° (yellow line), and (ρ_o, n, R_{disk}, i)= 5.0×10^{-11} g $\cdot$ cm^{-3}, 2.50, 50R_*, 50° (purple line), corresponding to $\mathcal{F}/\mathcal{F}_{min}$ of 1.00, 1.09, 1.11 and 1.19, from top to bottom, respectively.

models with the greater inclinations tended to fit the wings better since broader lines occur naturally with increasing inclination but the spectra corresponding to highest inclinations have a doubly-peaked shape unlike the observed profile.

Figure 3.4 shows the inclination versus $\mathcal{F}/\mathcal{F}_{min}$ for all of our computed models for $\mathcal{F}/\mathcal{F}_{min} \leq 2$. The symbols in the lower left of the figure correspond to the density power law exponent, n. The values of the base density, ρ_o, vary with n. Generally, for small n, i.e. slower density fall-off with increasing distance from the central star, ρ_o is also correspondingly reduced to obtain a similar amount of material in the disk to produce the Hα emission and vice versa. The horizontal dotted lines on Figure 3.4 correspond to the inclination $\pm 1\sigma$ obtained from Gaussian disk fits, GD, to the interferometry for ease of comparison. See Section 3.5 for more details about the geometric fits.

We see from Figure 3.4, and as discussed above, that our best-fitting models for $\mathcal{F}/\mathcal{F}_{min} \leq 1.2$ have inclinations with $46 \pm 5°$. However, with slight increases in the value of $\mathcal{F}/\mathcal{F}_{min}$ to within ~ 30 % we see a range in the inclination of $\sim 30°$ to $55°$. The lower limit of this range is consistent with the lower limit obtained by Q97 and the result of D11. Note all of our spectroscopic best-fitting models with $\mathcal{F}/\mathcal{F}_{min} \leq 2.0$ shown in Figure 3.4 corresponded to models computed with a disk size of $50R_*$.

3.4.2 Hα Interferometry

The image file outputs from Beray were fed into 2DDFT to obtain models of V^2 against spatial frequency which were then compared directly to data obtained from interferometry by a reduced χ^2 calculation. The best V^2 fit, $(n, \rho_o, i) = 3.0, 1.0 \times 10^{-10}$ g $\cdot$ cm^{-3}, $45°$, is shown with corresponding interferometric observations in Figure 3.5. Each plotted point represents a model V^2 that has a corresponding observed V^2 at the same location in (u, v) space. The model V^2 symbols are plotted as green circles (181 points), red triangles (62 points) and blue plus signs (48 points). The colours represent the degree of agreement between the model and observations. The green points have V^2 within the errors, and the red and blue represent models that have reduced χ^2 (χ^2_ν) too low and too high, respectively. The χ^2_ν corresponding to the best-fit model is 1.39 with a position angle, PA, of $121 \pm 1°$.

Figure 3.6 shows the PA for our models that correspond to $\chi^2_\nu \leq 5$. Horizontal lines correspond to the mean PA (solid blue line) and the mean $\pm 1\sigma$ (blue dotted lines) obtained from model fits to the interferometry for $\chi^2_\nu \leq 2.5$. We note that for models with $\chi^2_\nu \leq 2.5$ that there is considerable scatter in the PA of about the mean of $140°$ of $\sim 15°$. However, the five best-fit models corresponding to $\chi^2_\nu \leq 1.5$ shown on Figure 3.6 have a tight range of PAs of 121 ± 1. This is good agreement with the PA determined from the best elliptical Gaussian

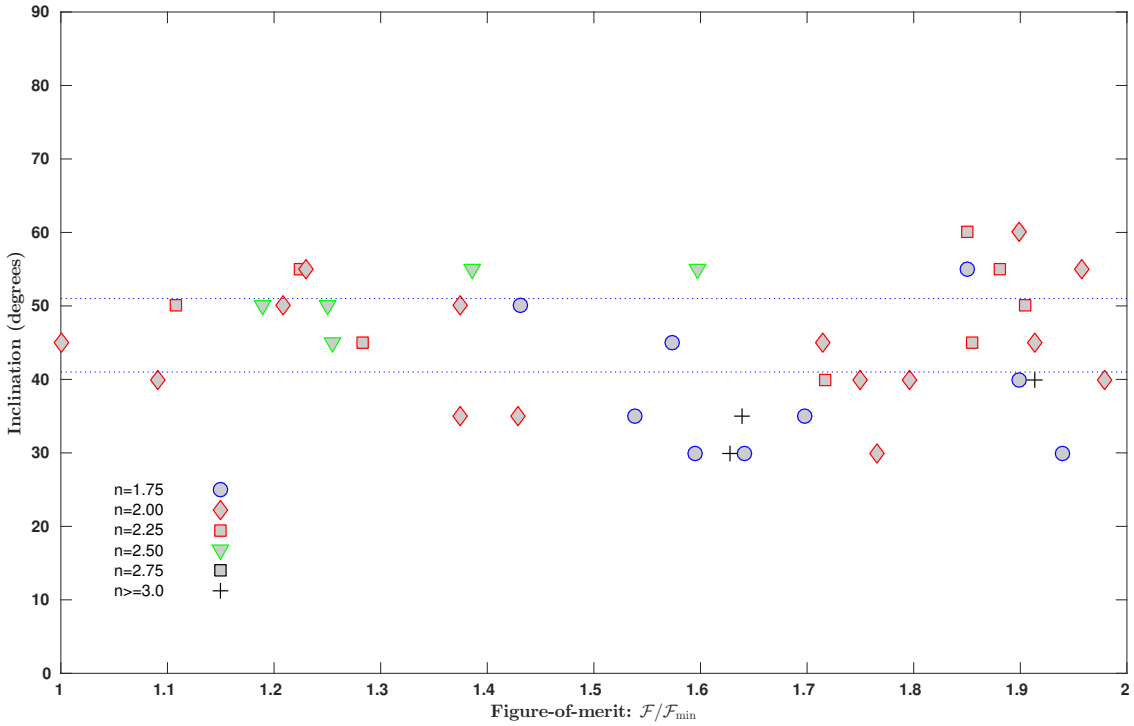

Figure 3.4: The model inclination distribution from Hα spectroscopy versus $\mathcal{F}/\mathcal{F}_{min}$. The symbols in the lower left show the range of n corresponding to models for $\mathcal{F}/\mathcal{F}_{min} \leq 2.0$. The horizontal dotted lines correspond to the inclination $\pm 1\sigma$ obtained from Gaussian disk fits, GD, to the interferometry.

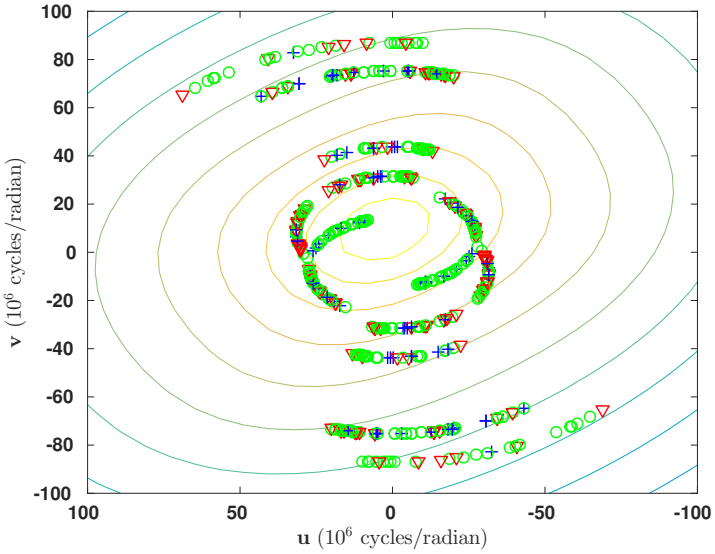

Figure 3.5: Best interferometric fit, (n, ρ_o, i) = 3.0, 1.0×10^{-10} g $\cdot$ cm^{-3}, 45°, plotted with observations. The model V^2 symbols are plotted as green circles (181 points), red triangles (62 points) and blue plus signs (48 points). The colours represent the degree of agreement between the model and observations. The green points have V^2 within the errors, and the red and blue represent models that have χ^2_ν too low and too high, respectively. The best-fit model has χ^2_ν of 1.39 and a position angle of $121 \pm 1°$. The contour spacing is 0.05 with the innermost contour corresponding to 0.95.

fit to the interferometry data shown in Figure 3.2. See Section 3.5 and Table 3.5 for details.

3.4.3 V^2 Geometric Fits

It is also interesting to compare the size the Hα emitting region and position angle of our models with geometric fits to the interferometry data. Geometric fits were also computed by D11 and Q97 for 48 Per so we include a comparison with their work as well. Tables 3.4 and 3.5 compare the results of geometric fits to the visibilities using UD and GD fits, respectively. These tables also provide the axis ratios of the minor axis to major axis, the position angle of the major axis of the disk on the sky with respect to north, the fractional contribution from the photosphere of the central star to the Hα containing interferometric signal, c_*, the reduced χ^2 and the number of data, N. The reader is referred to Sigut et al. (2015) and references therein for more details about our geometric models.

Table 3.4 shows good agreement with D11 for the axis ratio and position angle for the UD fits, however, we obtain a larger major axis than D11. There may be several reasons for this discrepancy. The fitting procedure is slightly different in each study with D11 determining the disk parameters by removing the stellar contribution. More significantly, we note that we have a substantially larger set of interferometry data consisting of 291 points providing a

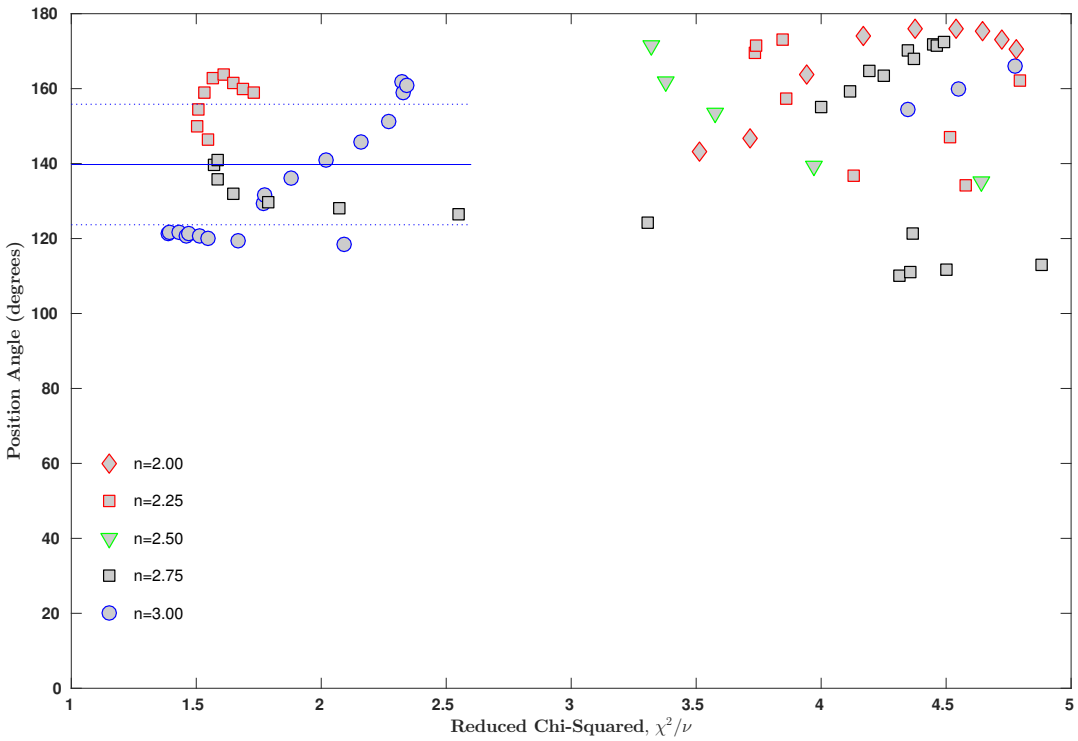

Figure 3.6: Plot of position angles, PA, in degrees versus χ^2_ν for $\chi^2_\nu \leq 5.0$. The symbols in the lower left show the range of the density parameter, n. The horizontal lines correspond to the mean PA (solid blue line) and the mean $\pm 1\sigma$ (blue dotted lines) obtained from model fits to the interferometry for $\chi^2_\nu \leq 2.5$.

Table 3.4. Uniform Disk (UD) Geometric Fits.

Study	Major Axis (mas)	Axis Ratio	Position Angle (°)	c_*	χ^2_ν
This study[a]	5.70 ± 0.11	0.69 ± 0.02	119 ± 3	0.876 ± 0.002	1.480[b]
D11	3.4 ± 0.2	0.765 ± 0.244	110 ± 19	—	0.56

Notes: [a]The central star is assumed to be represented by a UD of 0.306 mas. [b]The reduced χ^2 includes 291 points.

Table 3.5. Elliptical Gaussian Disk (GD) Geometric Fits.

Study	Major Axis (mas)	Axis Ratio	Position Angle (°)	c_*	χ^2_ν
This study	3.24 ± 0.08	0.71 ± 0.03	122 ± 3	0.855 ± 0.003	1.456
Q97	2.40 ± 0.52	0.86 ± 0.18	81 ± 43	–	–
Q97 Modified Fit	2.77 ± 0.56	0.89 ± 0.13	68	0.27	–
D11 result	2.1 ± 0.2	0.76 ± 0.35	115 ± 33	–	0.62

The same as Table 3.4 except for GD fits.

greater sky coverage in the (u, v) plane (see Figure 3.1). Table 1 and figure 1 in D11 shows the details of their observations and (u, v) plane coverage which is much less extensive compared to our data set. Q97 also fit their data for 48 Per with a UD and a ring-like model but the specific details about these geometric fits are not provided in their paper because they resulted in larger χ^2 than their GD fits. However, they mention that these models were not significantly different from the results for their GD models shown in Table 3.5.

A comparison of the results for the GD fits are presented in Table 3.5 and show good agreement with the major axis between D11 and this study. D11 obtained a smaller major axis than we obtain however D11's result does agree with Q97 within the errors. The axis ratios point to a disk that is not viewed at large inclination angle that would result in large deviations from circular symmetry. There is agreement in the PA obtained except for the modified model (that takes the contribution of the star into account) by Q97 which gives a PA about half the other values presented in Table 3.5. We also note that our definition of c_* is conceptually similar to c_p used by Q97. However, they used a 1 nm filter and did not fit for the parameter c_p. Their value is based on photometric counts and the expected values based on the V and B - V index.

Our UD and GD fits to interferometry shown in Table 3.4 and 3.5 give predicted axis ratios of 0.69 ± 0.02 and 0.71 ± 0.03, respectively. If we assume an infinitely thin disk, these ratios translate into inclination angles of $\sim 46°$, nearly identical to our predicted inclination of $45 \pm 5°$ from spectroscopy. Recall the horizontal dotted lines on Figure 3.4 corresponding to the inclination $\pm 1\sigma$ obtained from GD fits, plotted for convenience, with a range of predicted inclinations for $\mathcal{F}/\mathcal{F}_{min} \leq 2$ from our spectroscopy analysis. Clearly there is strong agreement between the geometric fits and our spectroscopy results for 48 Per's inclination.

A comparison of Tables 3.4 and 3.5 reveals that the major axis for the UD fits are always

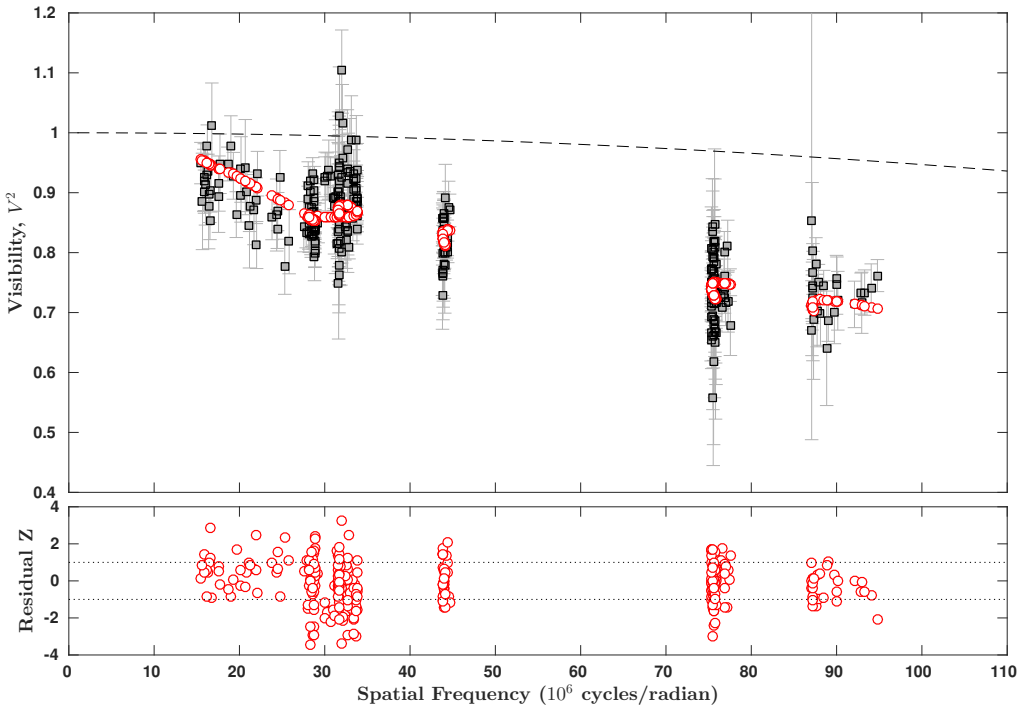

Figure 3.7: A comparison of predicted BERAY visibilities to the observations is shown in the top panel. The observed data along with associated error bars are shown in black and the model in red. The plot is constructed using the best-fit model with the parameters (n, ρ_o, i)= 3.0, 1.0×10^{-10} g · cm^{-3}, 45°. The dashed line corresponds to the star of a uniform disk of 0.306 mas. The residuals between the model and the data are shown in the bottom panel.

larger than the GD fits for each respective study. As a minor point of clarification, this is expected because the UD fits represent the major axis as the largest extent of the disk projected on the plane of the sky but for the GD fit, the size is proportional to the width of the Gaussian which only contains 68% of the light.

In order assess our model predictions, we compared our predicted BERAY visibilities with our best-fitting model obtained by our interferometry analysis. Figure 3.7 shows our model predictions corresponding to $(n, \rho_o, i) = 3.0, 1.0\times10^{-10}$ g · cm^{-3}, 45°. The observed data are shown in black with the model in red. The dashed line corresponds to the star of a uniform disk of 0.306 mas. The residuals between the model and the data are shown in the bottom panel.

Finally, we note that the best-fit elliptical Gaussian fit from our interferometry, shown in Figure 3.2, gives a PA of $121.65 \pm 3.17°$ in good agreement with our PA model results shown in Figure 3.6 for our five best-fit models with PAs of $121 \pm 1°$ corresponding to $\chi^2_\nu \leq 1.5$.

3.4.4 Spectral Energy Distributions

Spectral energy distributions, SEDs, were also computed with Beray, for wavelengths 0.4 to 4.2 microns for comparison with observations from Touhami et al. (2010). The SEDs were computed for the same range of density parameters and for the range of disk sizes as described in Section 3.3.3. Figure 3.8 shows the best fit model (solid blue line) corresponding to a χ^2_ν of 1.49 and a model with a much poorer fit (dashed red line). The parameters of the best fit model are $(\rho_o, n, R_{disk}, i) = 2.5\times10^{-10}$ g $\cdot$ cm^{-3}, 4.0, $6R_*$, and 25°. The poorer fit model has a reduction in its base density, ρ_o, by a factor of 250 but with all of the other parameters identical to the best fit model. The Touhami et al. (2010) fluxes are scaled separately at 0.44 μm following the prescription described in Sigut et al. (2015).

Note that the SED is best-fit by smaller disks of enhanced density that rapidly fall off with increasing distance from the central star. This seems to indicate that a volume of gas nearest the star with increased density is required to fit the near infrared flux with the size of the Hα emitting region being much larger.

3.4.5 Combined Results from Spectroscopy, Interferometry, and SED fits

Table 3.6 summarizes our model best-fit results based on Hα spectroscopy, Hα interferometry and SED fits. We note that while the best models from spectroscopy and interferometry are reasonably consistent and modelled with a disk size of $50R_*$, the SED best-fit corresponds to a disk size of $6R_*$ in our grid. As mentioned previously, the SED seems to indicate that a smaller volume of gas nearest the star of enhanced density is required to fit the IR flux. Figure 3.9 summarizes the best-fitting models within 20% based on our $\mathcal{F}/\mathcal{F}_{min}$ values for spectroscopy and χ^2_ν values for the interferometry and SED fitting. The regions enclosed in the red and blue solid lines in Figure 3.9 show the best 20% of our models for Hα, and V^2. The symbols on each ellipse are models. For the Hα spectroscopy there are four models within 20%. The parameters corresponding to these models are shown in Figure 3.3. For the Hα interferometry there are 19 models within 20% corresponding to χ^2_ν from 1.39 to 1.68. These 19 models have an average $n = 2.7 \pm 0.3$, $\rho_o = 5.5 \pm 4.2 \times 10^{-11}$ g $\cdot$ cm^{-3}, and inclination of 38° $\pm$ 12°. Interestingly, there is only one model corresponding to the best-fit SED within 20% and the position of this model is indicated by the shaded circle. This particular model has a χ^2_ν of 1.49. The position of the best parameters for the 36 top models for the SED are shown by the black dotted ellipse and represent $\chi^2_\nu \leq 4.01$. The dashed lines on Figure 3.9 show the model ($n = 2.25$ and $\log \rho_o = -11.1$) corresponding to the intersection of Hα spectroscopy and the Hα visibilities that is most consistent with these two observables.

As discussed above the model fits to the Hα spectroscopy and interferometry selected for

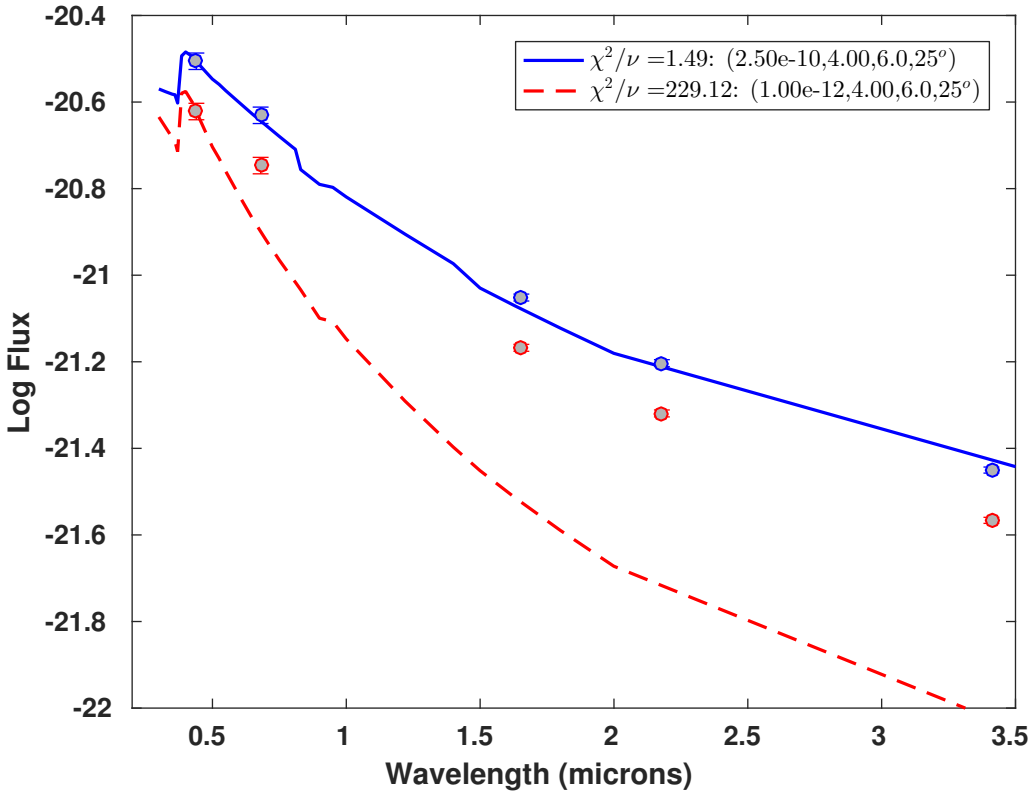

Figure 3.8: Spectral energy distributions for 48 Per compared with fluxes reported by Touhami et al. (2010). The best fit model is shown in as the solid blue line and a model with a much poorer fit is shown by the dashed red line. The parameters of each model are shown in the legend in the upper right of the Figure. Note that the parameters of the two models are identical except that the poorer fit has a reduction in its base density, ρ_o, by a factor of 250. The Touhami et al. (2010) fluxes are scaled separately at 0.44 μm.

Table 3.6. Best-fit Hα, V^2 and SED model results.

Fit	n	ρ_o (g cm^{-3})	i ($^\circ$)
Hα	2.0	5.0×10^{-12}	45 ± 5
V^2	3.0	1.0×10^{-10}	45 ± 12
SED	4.0	2.5×10^{-10}	25 ± 7

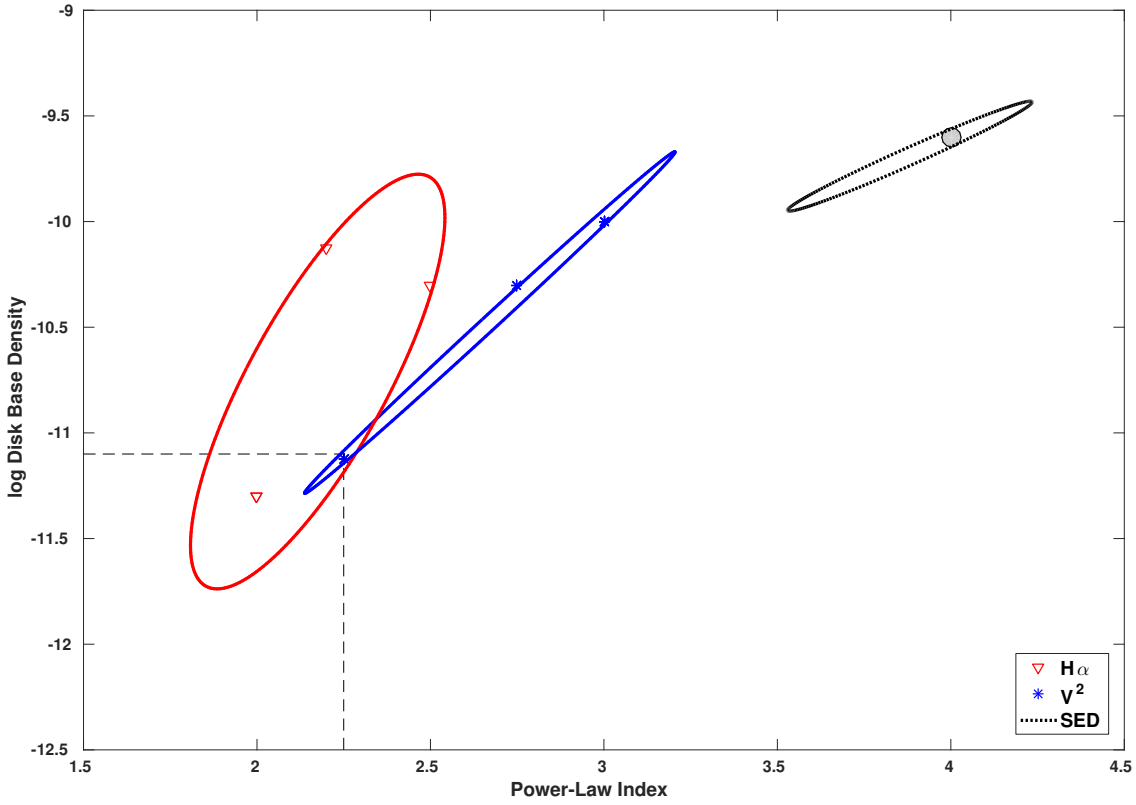

Figure 3.9: Best fitting density parameters, n and $\rho_\circ$ for 48 Per. The regions enclosed in the red and blue solid lines show the best 20% of our models for Hα, and V^2. The symbols on each ellipse are models. The SED has only one best fitting model in the 20% range and the position of this model is indicated by the shaded circle. The position of the best parameters for the 36 top models for the SED are shown by the black dotted ellipse and represent reduced χ^2 from 1.5 (the best fit) to 4.1. The dashed lines show the intersection of Hα spectroscopy and the visibilities for the model ($n = 2.25$ and $\log \rho_\circ = -11.1$) that is most consistent.

disks of $50R_*$ in our grid of models. By taking our best-fit image computed with Beray at $i = 0°$ (face-on) and constrained by Hα interferometry, we can integrate from the central star along a radial rays over distance to obtain a better estimate of the extent of the Hα emitting region. At large distances from central star, the Hα emission tends to originate from an increasingly diffuse disk. Therefore, we chose to integrate until 90% of the Hα flux is contained within the disk. Our best-fit model with n and log ρ_0 of 2.25 and = -11.1, respectively, corresponding to spectroscopy and the visibilities fitting as shown by the dashed lines in Figure 3.9 gives us R_{90}/R_* of 28.4, where R_{90} represents the radial distance corresponding to 90% of the Hα emission. This value corresponds to a mass for the Hα emitting region of 5.1×10^{24} g or $3.4 \times 10^{-10} M_*$. We note that this is likely a lower limit to the disk mass in the Hα emitting region since we find that a small, dense disk near the star is required to fit the SED. We also note that the radial extent of this dense region is not well constrained because the density falls rapidly with distance due to the large value of $n = 4.0$. Hence our disk mass estimate is not particularly sensitive to the radial extent of this region. For example, using the model that best reproduces the SED corresponding to $n = 4.0$ and $\log \rho_0 = -9.6$, for an R_{90}/R_* of 5 and 10 we obtain a disk mass of 3.5×10^{24} g and 4.3×10^{24} g, respectively. Therefore, the disk mass could easily double if this dense region was included. Furthermore, as mentioned above, our models produce Hα spectra that are too weak in the wings and this provides additional support to our claim that our mass estimate is a lower limit.

Finally, following the prescription in Sigut et al. (2015), we use our disk mass to determine the angular momentum, J, in the disk compared to the central star's momentum, J_*. We use an equatorial velocity of 360 km s^{-1} and assume 80% critical rotation for this calculation. For the model corresponding to the best-fit from spectroscopy and interferometry corresponding to a disk mass of 5.1×10^{24} g or 3.4×10^{-10} M_* we obtain a value for J of 3.6×10^{44} g cm^2 s^{-1} or 5.0×10^{-8} J_*. Using the mass estimates corresponding to the SED fits with R_{90}/R_* of 5 and 10, and disk masses of 3.5×10^{24} g and 4.3×10^{24} g, respectively, we obtain 9.3×10^{43} g cm^2 s^{-1} or 1.3×10^{-8} J_* and 1.3×10^{44} g cm^2 s^{-1} or 1.8×10^{-8} J_*. We note that, as already discussed, J corresponding to the region of enhanced density near the star required by the SED fitting is not very sensitive to the radial extent of this region due to the large power law value. We also see that also this region may be equivalent to the Hα disk mass, but its contribution to J is not as significant.

3.5 Discussion and Summary

Our best-fit models corresponding to our Hα spectroscopy and interferometry and SED fits are summarized in Table 3.6. Figure 3.9 is a graphical representation of the best-fitting regions

corresponding to each observational technology used in the study. Table 3.6 and Figure 3.9 show that 48 Per has a moderately dense disk with values of $n \sim 2$ to 3 and $\log \rho_0 \sim$ -11.8 to -9.4 or $\rho_0 \sim 2.0 \times 10^{-12}$ to 4.0×10^{-10} g $\cdot$ cm^{-3}, respectively from the the spectroscopy and interferometry analysis (see the red and blue ellipses on Figure 3.9 for the Hα and V^2 fits, respectively.) The radial extent with all of the best-fitting models for the Hα and V^2 fits correspond to the largest disks ($50R_*$) in our grid. The results from the spectroscopy and interferometry show agreement with a combined best-fit of $n = 2.25$ and $\log \rho_0 = -11.1$ or $\rho_0 = 7.94 \times 10^{-12}$ g $\cdot$ cm^{-3} corresponding to the dashed lines on Figure 3.9. The SED fitting suggests that a much denser disk of relatively small radial extent is required to fit the infrared wavelength regime. The best-fitting SED has an n of 4.0 and ρ_0 of 2.5×10^{-10} g $\cdot$ cm^{-3} as shown by the blue line on Figure 3.8 and shaded circle on Figure 3.9.

From spectroscopic analysis, there are 4 Hα models within 20% of $\mathcal{F}/\mathcal{F}_{min}$ value, and 19 models within 20% with χ^2_ν ranging from 1.39 to 1.68 corresponding to the visibilities. Only one SED model is within 20%, but we note that there are 36 models outside 20% with χ^2_ν from 1.49 to 4.01. Interestingly, all of these models have a range of $i \sim 20^\circ$ to 40° each with an n of 4 and $\rho_0 = 2.50 \times 10^{-10}$ g $\cdot$ cm^{-3}, consistently demonstrating the requirement of a dense region near the star that falls off quickly with radial distance.

As discussed in Section 3.4 our model spectral lines were too weak in the wings. Therefore, for line fitting purposes we used a core-weighted formula for our figure of merit, $\mathcal{F}$, which places more emphasis on the central portion of the line (see Figure 3.3). Di1 also found that it was not possible to fit the broad wings in the Hα line for 48 Per. They adopted an *ad hoc* scheme to account for non-coherent electron scattering, a process which redistributes absorbed line photons resulting in broader lines. This process has been well studied in the literature (see, for example, Mihalas (1978) for a detailed treatment) but it is difficult to properly account for in models because it lacks an analytic solution. The fact that our models were weak in the wings may also be due to this process. However, including a region of enhanced density near the star, where disk rotational velocities are largest (as suggested by our SED fitting analysis) may also improve our fits to the wings by adding more material at large rotational velocities. Alternatively, the poorer fit in the wings could also be due to the fact that a single value of n for each model was adopted for this study.

Jones, Tycner, and Smith 2011 analyze variability in the Hα equivalent widths for a sample of 49 Be stars. They determined that over the time frame of their study, which overlaps our observations, 48 Per was remarkably stable. In future, we plan to extend our modelling technique to include a two-component power law for the density parameter, n, to account for the dense inner region as predicted from our SED fitting while simultaneously matching the Hα

emitting region. It is interesting to speculate that the enhanced density in the disk near the central star may be signalling a disk building event and we plan to investigate this possibility.

References

Armstrong, J. T., Mozurkewich, D., Rickard, L. J., et al. (1998). *ApJ* 496, p. 550. DOI: 10.1086/305365.

Borgman, J. (1960). *Bull. Astron. Inst. Netherlands* 15, p. 255.

Burbidge, G. R. and Burbidge, E. M. (1953). *ApJ* 117, p. 407. DOI: 10.1086/145706.

Butler, H. E. and Seddon, H. (1960). *Publications of the Royal Observatory of Edinburgh* 2, pp. 188–217.

Cox, A. N. (2000). New York: AIP Press; Springer.

Delaa, O., Stee, P., Meilland, A., et al. (2011). *A & A* 529, A87, A87 (D11). DOI: 10.1051/0004-6361/201015639.

Hall, J. C., Fulton, E. E., Huenemoerder, D. P., et al. (1994). *PASP* 106, pp. 315–326. DOI: 10.1086/133381.

Hoffleit, D. and Jaschek, C. (1982).

Hutter, D., Zavala, R., Tycner, C., et al. (2016). *ApJS, submitted, arXiv e-print 1609.05254*. arXiv: 1609.05254 [astro-ph.SR].

Jones, C. E., Tycner, C., and Smith, A. D. (2011). *AJ* 141, 150, p. 150. DOI: 10.1088/0004-6256/141/5/150. arXiv: 1103.1514 [astro-ph.SR].

Mihalas, D. (1978). San Francisco: W. H. Freeman and Co.

Mourard, D., Clausse, J. M., Marcotto, A., et al. (2009). *A & A* 508, pp. 1073–1083. DOI: 10.1051/0004-6361/200913016.

Porter, J. M. and Rivinius, T. (2003). *PASP* 115, pp. 1153–1170. DOI: 10.1086/378307.

Quirrenbach, A., Bjorkman, K. S., Bjorkman, J. E., et al. (1997). *ApJ* 479, 477 (Q97). DOI: 10.1086/303854.

Rivinius, T., Carciofi, A. C., and Martayan, C. (2013). *A & Ar* 21, 69, p. 69. DOI: 10.1007/s00159-013-0069-0. arXiv: 1310.3962 [astro-ph.SR].

Ruusalepp, M. (1982). In: *Be Stars*. Ed. by M. Jaschek and H.-G. Groth. Vol. 98. IAU Symposium, pp. 303–310.

Shao, M., Colavita, M. M., Hines, B. E., et al. (1988). *A & A* 193, pp. 357–371.

Sigut, T. A. A. (2011). In: *IAU Symposium*. Ed. by C. Neiner, G. Wade, G. Meynet, et al. Vol. 272. IAU Symposium, pp. 426–427. DOI: 10.1017/S1743921311011045.

Sigut, T. A. A. and Jones, C. E. (2007). *ApJ* 668, pp. 481–491. DOI: 10.1086/521209. arXiv: 0706.4036.

Sigut, T. A. A., McGill, M. A., and Jones, C. E. (2009). *ApJ* 699, pp. 1973–1981. DOI: 10.1088/0004-637X/699/2/1973. arXiv: 0905.1295 [astro-ph.SR].

Sigut, T. A. A., Tycner, C., Jansen, B., et al. (2015). *The Astrophysical Journal* 814.2, p. 159.

Slettebak, A. (1949). *ApJ* 110, p. 498. DOI: 10.1086/145226.

Struve, O. (1931). *ApJ* 73, p. 94. DOI: 10.1086/143298.

ten Brummelaar, T. A., McAlister, H. A., Ridgway, S. T., et al. (2005). *ApJ* 628, pp. 453–465. DOI: 10.1086/430729. eprint: astro-ph/0504082.

Thompson, A. R., Moran, J. M., and Swenson, G. W. (1986). New York: Wiley-Interscience.

Touhami, Y., Richardson, N. D., Gies, D. R., et al. (2010). *PASP* 122, pp. 379–395. DOI: 10.1086/652009. arXiv: 1003.5876 [astro-ph.SR].

Tur, N. S., Goraya, P. S., and Chaubey, U. S. (1987). *Ap & SS* 139, pp. 257–262. DOI: 10.1007/BF00644354.

Tycner, C., Gilbreath, G. C., Zavala, R. T., et al. (2006). *AJ* 131, pp. 2710–2721. DOI: 10.1086/502679. eprint: astro-ph/0602087.

van Leeuwen, F. (2007). *A & A* 474, pp. 653–664. DOI: 10.1051/0004-6361:20078357. arXiv: 0708.1752.

Waters, L. B. F. M. (1986). *A & A* 162, pp. 121–139.

"That deep and lovely dark.
We'd never see the stars without it."

The Twelfth Doctor

4

ψ Persei

4.1 Introduction

Classical B-emission (Be) stars, such as ψ Per, are hot, rapidly rotating, and on the main sequence or slightly evolved. The defining characteristic of a Be star is the presence, even if transient, of a hydrogen Balmer emission line in its spectrum. Struve (1931) first proposed that the lines originate in a disk of circumstellar material around the equator of a star; later research has confirmed that this is, indeed, the case (see the reviews by Rivinius, Carciofi, and Martayan 2013; Porter and Rivinius 2003). Further distinguishing features include infrared excess and linearly polarized light. These systems also tend to be highly variable on a variety of timescales ranging from days to decades.

The first reported resolution of a Be star disk was made by Dougherty and Taylor (1992) who were able to constrain the position angle of the disk around ψ Per as well as the angular extent of the the 15 GHz emitting region; ψ Per is unusually radio-bright among Be stars. Recent studies such as Quirrenbach et al. (1997), Delaa et al. (2011) and Draper et al. (2014) present findings about ψ Per.

The results of this work have been compared to the study by Quirrenbach et al. (1997), hereafter called Q97. Q97 combined observations from the Mark III interferometer (Shao et al., 1988) with spectropolarimetric observations to characterize a set of seven Be stars including ψ Per. The interferometric portion of their program recorded 50 observations of ψ Per on 6 baselines between December 1991 and November 1992. Q97 concluded that the circumstellar

B. J. Grzenia, C. E. Jones, C. Tycner, T. A. A. Sigut, in preparation.

disk of ψ Per has an inclination angle of not less than 62°. More profoundly, Q97 also showed definitively that disks surrounding Be stars are geometrically thin, as their results proved that disks are not simultaneously geometrically and optically thick.

Doubly peaked emission lines infer that ψ Per is highly inclined to our line of sight, and this star also exhibits variability (Draper et al., 2014). Prior studies have limited themselves to observations from a single epoch. This work includes interferometric observations from 2006 and 2010; the availability of interferometry from these two epochs affords us a unique opportunity to quantify the effects of variability on the disk system.

The remainder of this chapter will cover details of the observation program in Section 4.2, followed by a brief description of the data pipeline used to compute our models and analyze the observations in Section 4.3. The results of the study are presented in Section 4.4 and discussed further in Section 4.5.

4.2 Observation Program

ψ Per was observed with the Navy Precision Optical Interferometer (NPOI), located on Anderson Mesa near Flagstaff, AZ, USA; for a complete technical description refer to Armstrong et al. (1998). A successor instrument to the Mark III, NPOI utilizes a system of 50-cm siderostats to direct starlight into an optics processing facility to produce interference fringes. Baselines can range from 18.9 m to 64.4 m, and observations from up to five baselines may be made simultaneously. Our observations of ψ Per used a 150 Å bandpass centred on Hα (6563 Å). This bandpass is considerably wider than the Hα line and ensures that the entire emission line is observed. A total of 335 interferometric visibility measurements were taken of ψ Per. Of these, 218 observations were taken in 2006 and the remaining 117 are from 2010. For a comprehensive list of the observation dates, see Table 4.1. Table 4.2 lists each observation by its modified Julian date and specifies which baseline was used.

Figure 4.1 shows the (u, v) plane positions of the observations of ψ Per. Actual observations are marked with open circles, and the uniform disk (UD) model fits to the observations in order to describe them are shown as arcs. For a given baseline, the arcs show where observations could lie in the (u, v) plane, with locations between the meridian and 6 h west denoted with solid lines and positions between the meridian and 6 h east with the dotted lines. A more detailed description of the modelling process can be found in Section 4.3. Figure 4.2 shows the squared, normalized interferometric visibilities plotted against spatial frequency. Each colour represents a different baseline pair in the same manner as Figure 4.1; going outward from the centre, the inner dark blue, inner red, orange, green, cyan, light blue, outer dark blue and outer red curves correspond to data from baselines of 18.9, 22.2, 29.5, 34.9 37.5, 38.2, 51.6

Table 4.1. Dates of NPOI Observations of ψ Per

Dates	Data Points
2006 Nov 07	22
2006 Nov 08	16
2006 Nov 09	16
2006 Nov 10	10
2006 Nov 11	14
2006 Nov 14	2
2006 Nov 15	10
2006 Nov 16	24
2006 Nov 17	36
2006 Nov 18	24
2006 Nov 20	10
2006 Nov 21	12
2006 Nov 22	18
2006 Nov 23	4
2010 Jan 06	36
2010 Jan 07	32
2010 Jan 08	4
2010 Jan 09	4
2010 Jan 10	1
2010 Jan 12	40

Table 4.2. Interferometric NPOI Observations of ψ Per for 2006 and 2010 (partial)

JD-2,450,000	u (m)	v (m)	V^2	Baseline
4046.741	18.963	−20.782	0.721 ± 0.024	AC-AE
4046.741	−30.128	−1.345	0.853 ± 0.036	AC-AW
4046.777	22.937	−17.209	0.770 ± 0.035	AC-AE
4046.777	−31.424	−6.594	0.906 ± 0.060	AC-AW
4046.811	25.630	−13.253	0.744 ± 0.018	AC-AE

Table 4.2 is shown in its entirety in Appendix B as a machine readable table. A portion is shown here for guidance regarding its form and content. This table contains observations from all reported epochs.

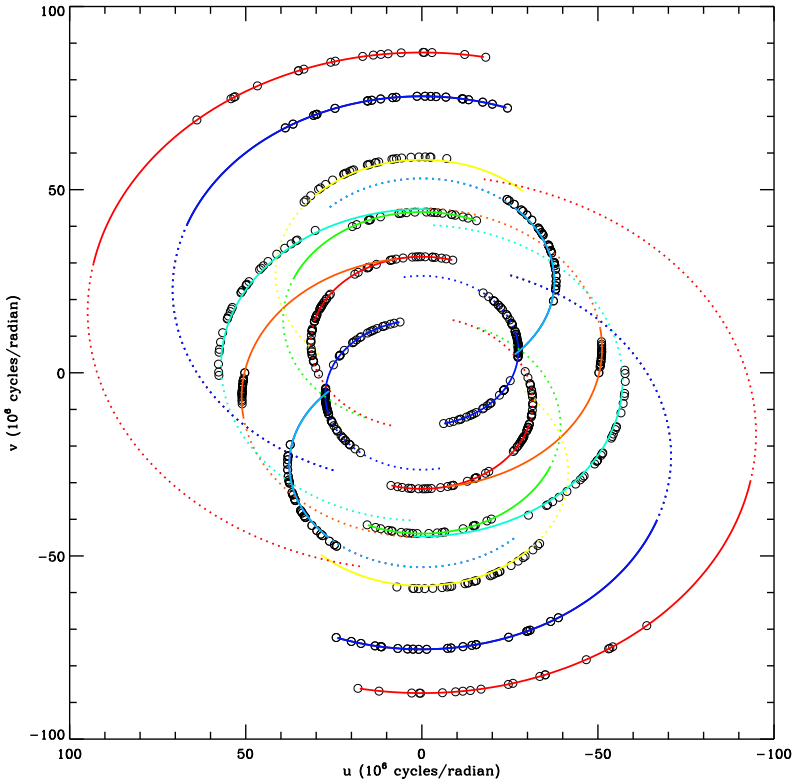

Figure 4.1: Sky coverage in the (u, v) plane for ψ Per. Observations are represented by open black circles and the arcs, each of which corresponds to a separate baseline, delineate the full expanse of possible (u, v) plane coverage for the observations. The dotted half of each arc represents the region of the (u, v) space from the meridian to 6h east; the solid portion covers the meridian to 6h west. The observations shown in this figure combine both the 2006 and 2010 observations. Observations were made with eight distinct baselines. The inner dark blue, inner red, green, outer dark blue and outer red curves correspond to data from baselines of 18.9, 22.2, 29.5, 34.9, 37.5, 38.2, 51.6, and 64.4 m, respectively.

and 64.4 m, respectively. The solid curves connecting these points account for the changes in a baseline's projection onto the sky due to diurnal motion. The three lines on the plot correspond to the structure of ψ Per. The dashed line near the top is a model of the visibility curve if ψ Per and its extended structure could not be differentiated from a point source. The two dotted lines forming an envelope around the squared visibilities correspond to the minor and major axes of the extended disk structure, with the lower curve showing the change in visibility associated with resolution of the major axis, and the upper curve describing the same for the minor axis.

An echelle spectrograph, the Solar Stellar Spectrograph (SSS) is mounted on the John S. Hall Telescope at Lowell Observatory (Hall et al. 1994; Tycner et al. 2006). This instrument was used contemporaneously with the 2006 observing campaign to record Hα spectra from

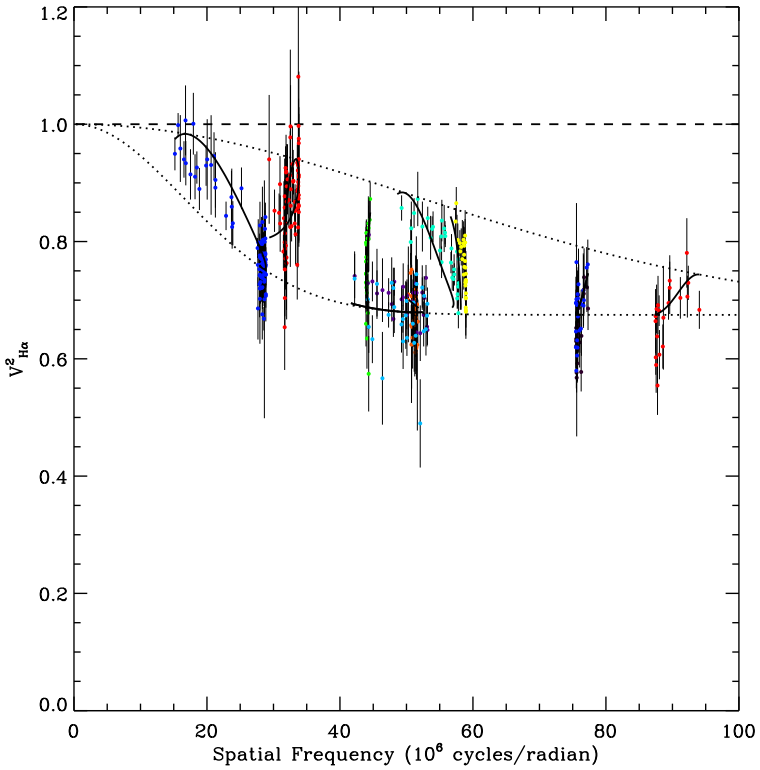

Figure 4.2: Observed interferometric visibility per spatial frequency for ψ Per. The coloured points correspond to the baseline arcs in Figure 4.1 while the black arcs seen within each grouping of observations represent the change in projected baseline due to the effects of diurnal motion. Other lines on the plot describe the geometry of the extended structure; dotted lines demarcate the minor (upper curve) and major (lower curve) axes as fit with a UD. The dashed line is the visibility curve that would be seen if ψ Per could not be distinguished from a point source.

ψ Per. Consistent with a highly inclined disk, the Hα line profile is doubly peaked (see Figure 4.8).

4.3 Modelling

This study used the Bedisk-Beray-2dDFT pipeline described in greater detail in Chapter 3. Bedisk adopts a power-law relationship, Equation 4.1,

$$\rho(R, Z) = \rho_0 \left(\frac{R_*}{R}\right)^n \exp\left[-\left(\frac{Z}{H}\right)^2\right], \tag{4.1}$$

to calculate the density of material in the disk (ρ) at R (horizontal) and Z vertical points within the disk as a function of the density at the disk-photosphere interface (ρ_0) and the power law factor n. H is the vertical scale height measured normal to the disk. Bedisk calculates thermal and density structures of the circumstellar environment from the stellar UV flux, assuming radiative equilibrium in the disk material (Sigut and Jones, 2007). These outputs from Bedisk are supplied to Beray, which solves the radiative transfer equation along the observer's line of sight (Sigut, 2011). Beray output includes an intensity image of the disk system. 2dDFT is then used to produce visibilities in Fourier space which can then be compared directly to interferometric observations.

4.4 Results

4.4.1 Model Grids

Q97 modelled ψ Per as a B5Ve star, with the parameters found in Table 4.3 and consistent with Cox (2000) as well as older references (Miczaika 1951; Lesh 1968). After adopting these same parameters, we consulted references such as Waters (1986) in order to make certain that our grid space would cover all combinations of n and ρ_0 which are likely to produce valid models. Additional verification was made with more recent work, such as that seen in section 5.1.3 of Rivinius, Carciofi, and Martayan (2013). A total of 1798 models were calculated, covering $1.5 \leq n \leq 5.0$, $1.0 \times 10^{-12} \leq \rho_0 \leq 5.0 \times 10^{-10}$ g $\cdot$ cm^{-3}, at inclination angles ranging from 50° to 85°. The models were incremented in steps of 0.5 in n and 2.5 over each order of magnitude in ρ_0; i was incremented in 5° steps. In some parts of the (n, ρ_0, i) space, the increments were narrowed to steps of 0.1 in n and 0.3 over each order of magnitude for ρ_0. This was done in order to discern subtle differences in fit quality among the V^2 models. The models were calculated out to a distance of $50R_*$ to ensure that they were not prematurely truncated.

Table 4.3. Adopted stellar parameters

Parameter	B5Ve
Radius ($R_\odot$)	3.9
Mass ($\mathcal{M}_\odot$)	5.9
Luminosity ($L_\odot$)	7.28×10^2
T_{eff} (K)	15200
$\log g$	4.0
Distance (pc)	178
Central star angular diameter* (mas)	0.0

Parameters adopted for ψ Per, consistent with Q97 and Cox (2000). *Central star is unresolved.

4.4.2 Interferometry

Modelling the 2006 observations, we find that the data are best reproduced by the model with $(n, \rho_0, i) = 2.5, 4.0 \times 10^{-11}, 75°$, with a χ^2_i of 1.18 and equivalent width (EW) = 26.16 Å (calculated theoretically in Beray), compared to a measured EW of 40.0 Å. The major and minor axis curves, observations, and modelled V^2 for the 2006 best fit is shown in Figure 4.3. Basing the models on the subset of NPOI observations from 2010 instead, as seen in Figure 4.4, produces a different result with the best fit occurring at $(n, \rho_0, i) = 2.0, 5.0 \times 10^{-12}$ g $\cdot$ cm^{-3}, 77.5° and $\chi^2_i = 0.90$. The theoretical Hα linewidth, again as calculated with Beray, is EW = 28.38 Å.

Figure 4.5 shows the goodness-of-fit for each model V^2 compared to the 2006 NPOI observations. The data markers indicate the goodness-of-fit for each model. Those that fall within the error range for their corresponding observations are indicated by open green circles. Those that fall below the range appear as red triangles, and the blue '+' signs indicate that the model is below the lower limit of the error bar. Figure 4.6 contains the same information for the 2010 observations; consistent with the numerical χ^2_i, the lower proportion of blue and red symbols indicates that the model for 2010 is a better fit to the observation than the best-fit 2006 model. Both the 2006 and 2010 models fit 80% of their respective observations to within error. The models that fell above and below were evenly distributed, with 2006 having 10% of its models falling into each category and 2010 having 8% above and 12% below.

Figure 4.7 was generated by combining the 2006 and 2010 interferometry into a single set

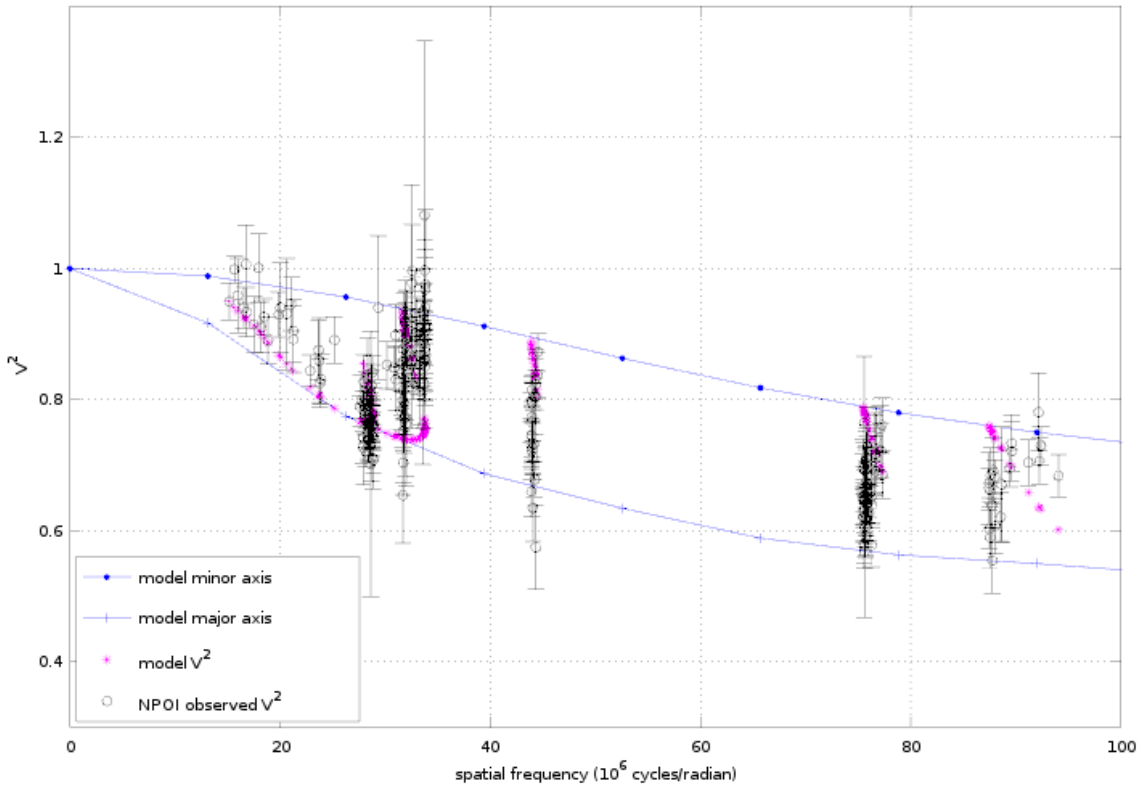

Figure 4.3: NPOI observations from 2006 plotted with model observations and minor (upper) and major (lower) axis curves for the best-fit V^2 model, where $n = 2.5$, $\rho_o = 4.0 \times 10^{-11}$ g $\cdot$ cm^{-3}, $i = 75^\circ$ and χ^2_i=1.18. The corresponding theoretical Hα EW from Beray is 26.16 Å (measured EW = 40.0 Å).

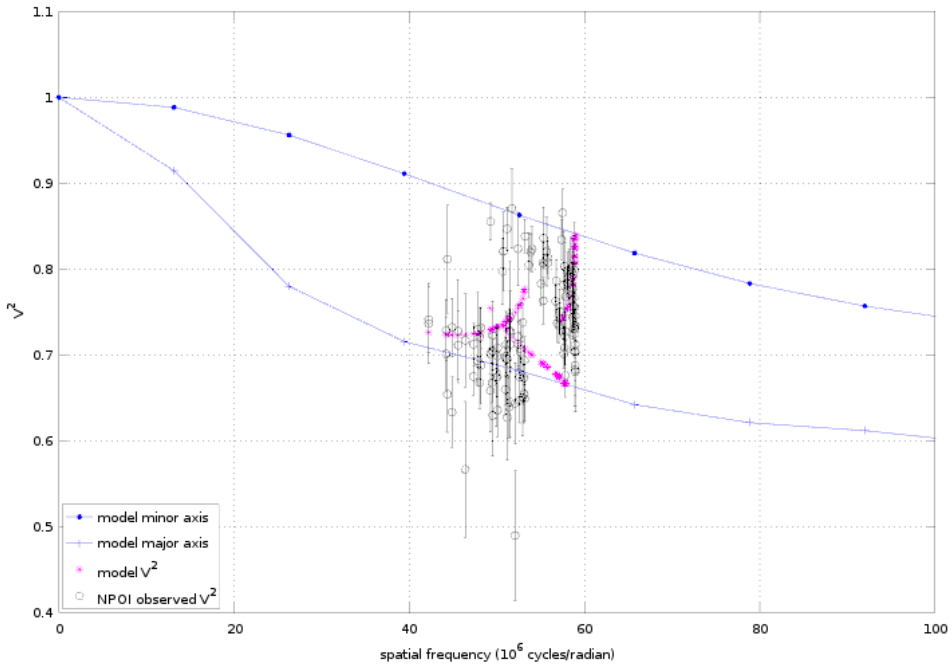

Figure 4.4: Plot of best-fit V^2 models with observations from 2010. The best-fit (n, ρ_o, i) is 2.0, 5.0×10^{-12} g · cm^{-3}, 75°, with χ^2_i = 0.90. The dotted curves below, which intersect with both the observed and modelled data, represent the minor axis (upper curve) and major axis (lower curve) of the disk as it is seen on the sky. The corresponding theoretical Hα EW (Beray) is 28.38 Å (observed EW = 40.0 Å).

which was compared with the 2006 best-fit model. There is an obviously larger number of red triangles marking the data points in the combined plot, which are concentrated in an area bounded approximately by $-50 \leq v \leq +50$ 10^6 cycles/radian and $-50 \leq u \leq +50$ 10^6 cycles/radian. These points fall in the same positions as the 2010 observations shown by themselves in Figure 4.6. As mentioned, red triangles indicate that the model falls outside the lower error bar of the corresponding 2006 observation. This is a strong indication that the disk has changed substantially between 2006 and 2010. The decrease in the base density (ρ_o) parameter between 2006 and 2010 is consistent with a disk mass-loss event. Draper et al. (2014) also note the occurrence of a mass-loss event in their observations, which covered the epochs from 1991 to 2004. These are discussed in more detail in Section 4.5.

4.4.3 Hα Line Spectroscopy

Poorly fitting Hα models were removed in the next step. The remaining profiles were then compared with the observed lines. Since it is understood that the line modelling routine does not simulate all processes in the wings the portion of a model profile with F/F_c less than the full-width half-maximum was not considered. This was done so that a figure-of-merit

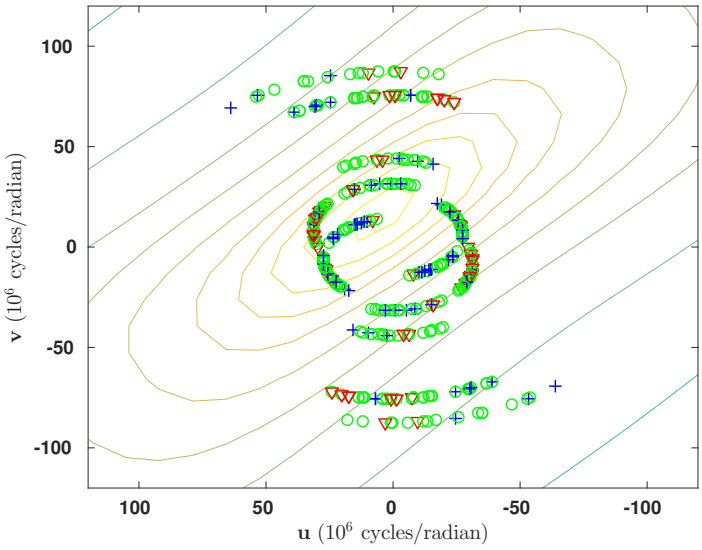

Figure 4.5: Plot of modelled V^2 for ψ Per. Goodness-of-fit is indicated for each model by its data point marker; fits within the observational error range are indicated by green circles (80% of points shown). Models that fall above or below the error range are shown as blue `+' signs (10%) or red triangles (10%), respectively. Figure 4.5 is the best-fit V^2 model for the 2006 data, with $n = 2.5, \rho_o = 4.0 \times 10^{-11}$ g $\cdot$ cm$^{-3}, i = 75^\circ$ and χ_i^2=1.18. Theoretical EW is 26.16 Å (observed EW = 40.0 Å) and the position angle of the major axis is 135°.

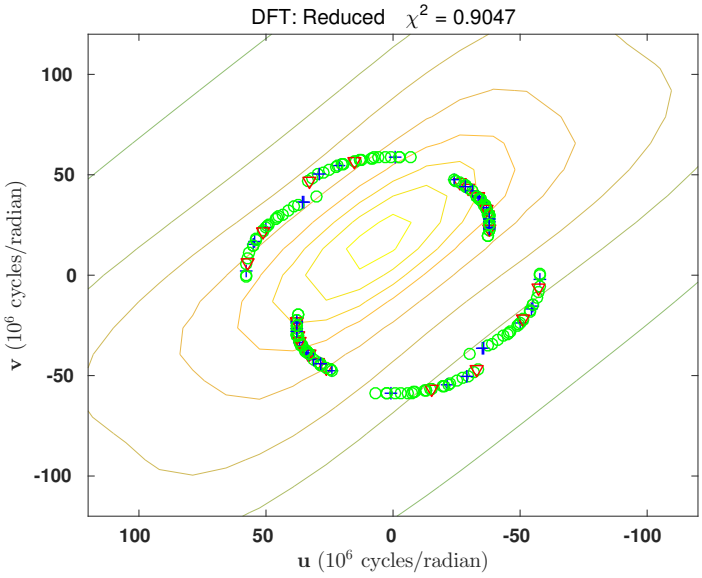

Figure 4.6: Same as Figure 4.5 but for 2010 V^2 observations. This figure shows the best-fit V^2 model for the 2010 data, with $n = 2.0, \rho_o = 5.0 \times 10^{-12}$ g $\cdot$ cm$^{-3}, i = 75^\circ$ and χ_i^2= 0.90. In this case, 80% of the fits are represented by green circles, indicating that the model fits to within error. Blue `+' signs and red triangles, indicating fits outside errors, are 8% and 12%, respectively. EW is 28.38 Å (observed EW = 40.0 Å) and the position angle of the major axis is 135°.

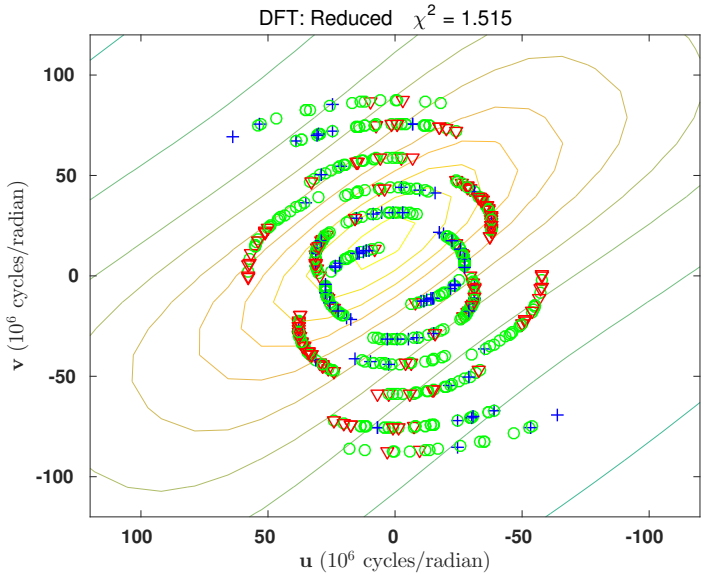

Figure 4.7: Same as Figures 4.5 and 4.6, but with observations for both epochs combined and compared to the 2006 best-fit V^2 model. This plot is the result of combining the 2006 and 2010 observations. Note the large proportion of red triangles in the region bounded by $-50 \leq v \leq +50\ 10^6$ cycles/radian and $-50 \leq u \leq +50\ 10^6$ cycles/radian. These points indicate the 2010 observations and clearly show that they are well outside the error range of the 2006 data. This result is indicative of ψ Per's variability. Overall, of the points shown on this plot, 71% indicate fits to within error, 12% are for fits above error, and the remaining 17% mark models below the error bars for their corresponding observations.

Table 4.4. Best-fit (n, ρ_o, i) for V^2 fits for each epoch.

Spectral Type	Epoch	n	ρ_o (g · cm^{-3})	$i(^\circ)$	χ^2_i
B5Ve	2006	2.5	4.0×10^{-11}	75	1.18
	2010	2.0	5.0×10^{-12}	75	0.90

Best-fit interferometric (V^2) (ρ_o, n, R_{disk}, i) for 2006 and 2010. Disk models were calculated out to a distance of $50R_*$.

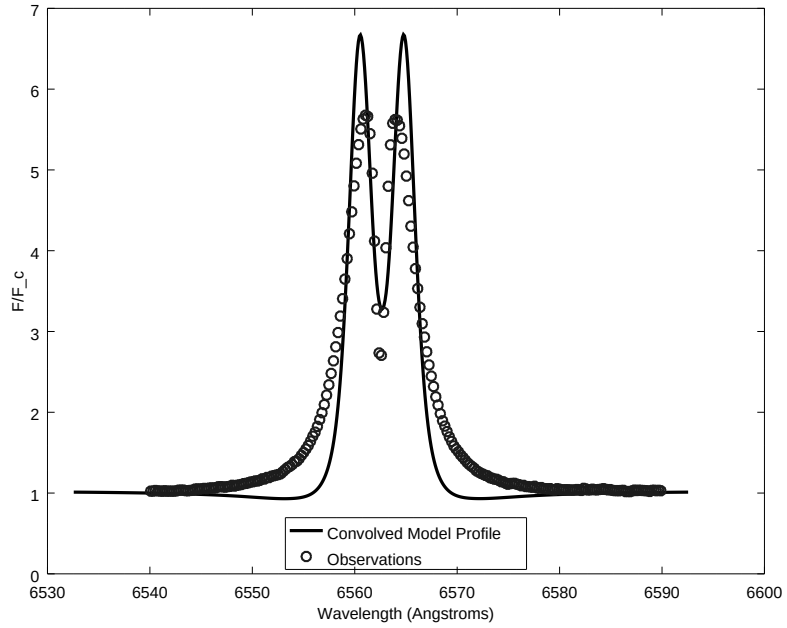

Figure 4.8: Line profile of the best Hα fit convolved with the 2006 data, with $n = 2.0, \rho_o = 7.5 \times 10^{-12}\,\mathrm{g \cdot cm^{-3}}$, $i = 85^\circ$ and a normalized $\mathcal{F}/\mathcal{F}_{min} = 1.0$. This line has an EW of 31 Å.

could be used to quantify the goodness of fit between the central features of the observed and modelled lines without introducing a bias due to the wing discrepancies. The figure-of-merit, $\mathcal{F}$, is defined by Equation 4.2,

$$\mathcal{F} = \frac{1}{N} \sum_i \frac{\left| F_i^{obs} - F_i^{mod} \right|}{F_i^{obs}}. \tag{4.2}$$

Here, the absolute value of the difference between a given observed intensity F_i^{obs} and its model counterpart F_i^{mod} is normalized by the observed intensity and summed. The summation is then multiplied by the reciprocal of the total number of data points, N. For ease of comparison, figures-of-merit for all model-observation comparisons are normalized by $\mathcal{F}_{min}$. The figure-of-merit is used to assess the goodness-of-fit for Hα spectroscopy models. Since it is also used in a manner similar to χ_i^2, $\mathcal{F}/\mathcal{F}_{min}$ is denoted as χ_s^2, with the subscript s to signify that it describes the spectroscopic rather than the interferometric result.

The model Hα profiles associated with the best fits fell in a range from 25.69 to 30.94 Å, as compared to the observationally measured EW of 40.0 Å. We used the full-width half-maximum width of the observed line to designate cutoff points. Intensities associated with

Table 4.5. Disk radii determined from the proportion of Hα flux enclosed.

Spectral Type	Epoch	50% (R_*)	75% (R_*)	90% (R_*)
B5Ve	2006	2.3	9.2	24
	2010	15	30	43

Radii of disks containing 50%, 75% and 90% of the Hα flux for the best-fit V^2 model for 2006, given in terms of R_* (where $R_* = 3.9 R_\odot$). Parameters for the 2006 fit are $n = 2.5$, $\rho_0 = 4.0 \times 10^{-11}$ g $\cdot$ cm^{-3}. The best-fit V^2 model for 2010 used the parameters $n = 2.0$, $\rho_0 = 5.0 \times 10^{-12}$ g $\cdot$ cm^{-3}.

wavelengths shorter than 6557 Å or longer than 6569 Å were excluded from the analysis, which gave us information about the fit quality as it pertains to the peaks and central absorption feature of the line (the full profile is shown nonetheless in Figure 4.8). Some of the discrepancy between the observed and modelled EWs can be attributed to the linewing mismatch which was described previously. The portion of the line considered by the fitting routine was a reasonably good fit in terms of the figure-of-merit, although the tops of the peaks and bottom of the trough are clearly higher in intensity than their observed counterparts. Nonetheless, the model fit shown in Figure 4.8 was the best available match.

Despite the fact that our model calculations extended to a radial distance of $50R_*$, we can more accurately compute the size of the Hα emitting region by the following procedure. The physical extent of the Hα-emitting portion of the ψ Per disk system was estimated by integrating over the horizontal distance R until a given proportion of the flux was enclosed, using a model with $i = 0°$. Estimates of the disk sizes required to enclose 50%, 75% and 90% of the Hα flux are listed in Table 4.5.

4.5 Discussion and Summary

Hα emission in Be star spectra originates in regions of the disk located approximately 10 to $50R_*$ from the star (Wisniewski et al., 2007). Size estimates based on a GD model encompassing 80% of a star's brightness at FWHM for Hα emitting regions for 12 Be stars are shown in Rivinius, Carciofi, and Martayan (2013). Estimated radii range from $3.24R_*$ for β CMi to $16.36R_*$ for ψ Per. ψ Per is not known to be part of a binary system (Chapter 2; Rivinius, Štefl, and Baade (2006); Balona (1995); Hiltner, Garrison, and Schild (1969)), which would likely necessitate an earlier truncation due to the influence of the companion object. The size

of the Hα emitting region as determined from our model results, as provided in Table 4.5, is in agreement with these estimates.

As mentioned in Section 4.2, observations from two epochs were compared for purposes of modelling ψ Per. The data from Jones, Tycner, and Smith 2011 demonstrate that ψ Per had entered a quiescent phase when their observations were taken. While their observations were recorded between 2003 and 2007 and therefore were contemporaneous with our 2006 interferometry, by 2010 the quiescent phase had ended. Variability of ψ Per was studied as well by Draper et al. (2014) using archived polarimetric observations from the HPOL spectropolarimeter at the Pine Bluff Observatory. Their observations, recorded between 1991 and 2004 and preceding those made by Jones, Tycner, and Smith 2011, show significant variability which they attribute to partial disk dissipation, based on the results of a similar study of π Aqr and 60 Cyg by Wisniewski et al. (2010).

While the 2006 (n, ρ_0, i) parameters for the best Hα and V^2 fits did not overlap precisely, the (n, ρ_0, i) of the best 10% models overall coincide in two regions. Figure 4.9 shows two sets of points: orange, marking the points on the (n, ρ_0) space where the best 10% of the interferometric models occurred, and the blue points indicating the same for spectroscopy. The intersecting regions run from $2.0 \leq n \leq 2.3$ with $5.0 \times 10^{-12} \leq \rho_0 \leq 1.0 \times 10^{-11}$ and $2.5 \leq n \leq 2.7$ with $2.0 \times 10^{-11} \leq \rho_0 \leq 7.0 \times 10^{-11}$. The best fitting model for 2006 is $n = 2.5$, $\rho_0 = 4.0 \times 10^{-11}$ g $\cdot$ cm^{-3}, $i = 75°$. For 2010, the best-fit model corresponds to $n = 2.0$, $\rho_0 = 5.0 \times 10^{-12}$ g $\cdot$ cm^{-3}, $i = 75°$. We note that the reduction in ρ_0 a loss of disk mass between 2006 and 2010 consistent with the findings of Draper et al. (2014).

In addition to the information described previously, the data pipeline also calculates position angles (PAs) for the major axis of the disk on the sky with respect to north, which are summarized in Table 4.6. For ψ Per, we obtained an estimate of $135 \pm 3°$. Draper et al. 2014 also modelled ψ Per and obtained a field-star estimate of $112 \pm 11°$ for the PA of ψ Per. While this is still outside the error range for Q97 (that study found PA = $37 \pm 11°$), it is nonetheless more consistent with our estimate for this study. Per Draper et al. 2014, it is likely that some of the inconsistencies in PA between Q97 (which was based on observations made in 1991 and 1992) and newer studies could be due to changes within the disk.

A description of the disk system can be obtained by means of geometric disk fitting. Information such as the position angle, inclination and physical size of the disk can be inferred from the overall shape of the extended structure. Both UD and GD fits were applied to the observations in order to estimate the ratio of the disk's minor and major axes. From these quantities estimates were made of the angular size of the disk on the sky, which can then be used with parallax measurements to make a first-order approximation of the actual physical

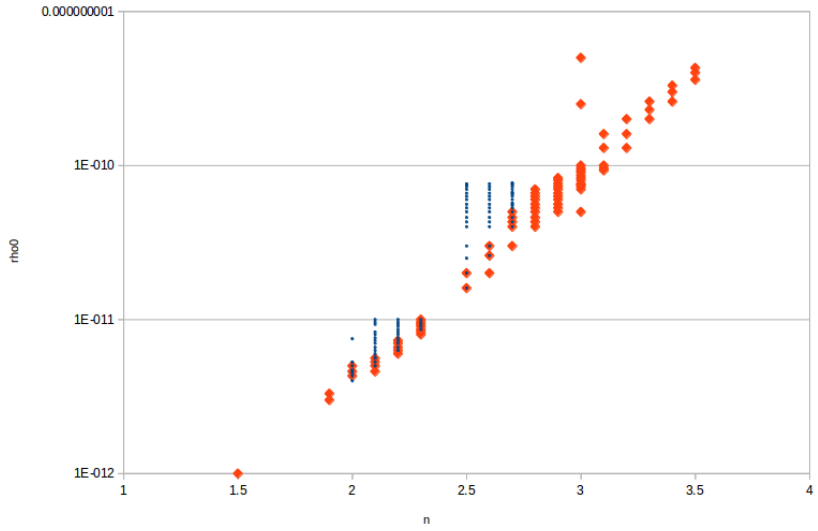

Figure 4.9: Plot delineating regions in (n, ρ_o) space corresponding to the best V^2 (orange) and Hα (blue) fits. The best Hα fits and best V^2 fits coincide in two regions, $2.0 \leq n \leq 2.3$ and $5.0 \times 10^{-12} \leq \rho_o \leq 1.0 \times 10^{-11}$ g $\cdot$ cm^{-3} and $2.5 \leq n \leq 2.7$ and $2.0 \times 10^{-11} \leq \rho_o \leq 7.0 \times 10^{-11}$ g $\cdot$ cm^{-3}. These points on the (n, ρ_o) space correspond to the best 10% of the V^2 and Hα models, respectively.

Table 4.6. Position angles of the best χ_i^2 and χ_s^2 models.

Parameters	Position Angle (°)	χ_i^2	χ_s^2
This study (2006 interferometry)	135 ± 3	1.18	1.28
This study (2010 interferometry)	136 ± 4	0.90	1.05
Q97	-37 $\pm$ 11	–	–
Draper et al. 2014	112 ± 11	–	–

Position angles of the major axis of the extended structure of ψ Per, measured east from north. Error estimates for PAs calculated for our study are equal to one standard deviation in PA over the parameter set.

extent of the disk, which subsequently can be compared to model results. As seen in Table 4.7, applying a UD fit to our 2006 interferometry gives an axis ratio of 0.38 ± 0.16 whereas the axis ratio corresponding to the GD fit is 0.34 ± 0.02. Q97 made axis ratio estimates of 0.47 ± 0.11 (GD). In the review by Rivinius, Carciofi, and Martayan 2013, table 2 gives a summary of GD sizes organized by emitting region. Two listings exist for each star; ψ Per shows $13.34 \pm 0.94 R_*$, derived from Q97's measurements and assuming a central star of radius $4.7 R_\odot$. Our models assume a $3.9 R_\odot$ central star. Note that our estimate of $9.2 R_*$ as the extent of a disk enclosing 75% of the Hα flux is only slightly smaller than the $13.34 R_*$ which encloses 80% of the flux as reported in Rivinius, Carciofi, and Martayan (2013).

The disk axis ratios obtained by geometric fitting can be used to estimate the inclination angle of the disk. In Equation 4.3,

$$i = \arccos(r), \tag{4.3}$$

i is the inclination angle of the disk and r is the minor-to-major axis ratio as determined from geometric fitting. This expression assumes an infinitely thin axisymmetric disk and treats the shortening of the minor axis as an effect of projection. Thus, the ratio of the minor and major axes is equivalent to the cosine of the angle between the minor axis of the disk and the vertical direction. Inclination angles obtained by this method are lower limits; as explained in Quirrenbach et al. (1993), adding thickness to the disk will change Equation 4.3 such that $i \geq \arccos(r)$. Table 4.7 lists the axis ratios obtained from UD and GD fitting based on interferometry for both epochs. Utilizing Equation 4.3, we obtain inclination angles of $68 \pm 9^\circ$ (UD) and $70 \pm 1^\circ$ (GD) for 2006. For 2010, we obtain $59 \pm 3^\circ$ for the UD and $61 \pm 2^\circ$ for the GD. As all of our inclination angles measured by other methods are in excess of these estimated lower limits, these two sets of quantities are in good agreement.

It has been duly noted that the wings of the Hα lines, such as those in Figure 4.8, are forecast to be considerably narrower than the actual observations. The exact cause of this line broadening has not been determined conclusively but it is believed to result from noncoherent scattering that occurs in the region of the disk nearest the stellar surface. This type of scattering lacks an analytical description and for that reason it is difficult to implement. Also, the uniform power-law model of the disk may not be valid for the entirety of the disk. Further study will be needed to determine if a different modelling approach will account for the discrepancy.

The variability of ψ Per was a significant issue and made it inadvisable to combine the observations from both 2006 and 2010. The article by Jones, Tycner, and Smith 2011 described

Table 4.7. Optimal Geometric Disk Fits.

Star	θ_{UD} (mas)	a_{min}/a_{maj} (UD)	θ_{GD} (mas)	a_{min}/a_{maj} (GD)
ψ Per (2006 observed)	6.48 ± 0.35	0.38 ± 0.16	3.94 ± 0.12	0.34 ± 0.02
ψ Per (2010 observed)	6.34 ± 1.95	0.51 ± 0.05	3.03 ± 0.33	0.48 ± 0.03
Q97* result	–	–	3.26 ± 0.23	0.47 ± 0.11

Best geometric disk fits for ψ Per. UD = uniform disk; GD = Gaussian disk. Disk major axis estimates for the current study were made based on the Hipparcos parallax measurements (van Leeuwen, 2007) and calculated axis ratios; results for Q97 were taken directly from that study. *Results are for the modified GD fits shown on the right-hand side of Q97's table 4.

an extensive analysis of variability trends in the EW of the Hα line profile for a sample of 49 Be stars. Their study coincided with a relatively quiescent period for ψ Per, a time span of approximately 1100 Julian days during which the Hα EW increased steadily by only 3 Å. Their findings led them to report that ψ Per may be a variable star, but at a confidence level of only 34%. Later observation programs such as the one by Draper et al. (2014) demonstrate that this period of quiescence is an anomaly. Hubert and Floquet (1998) measured a cyclical Hα variability for ψ Per, with a period of 1.029 d. The differences in the (n, ρ_o, i) results (see Section 4.4.2) seem to indicate that the variability of ψ Per between 2006 and 2010 is sufficient to necessitate a new model to describe the disk system.

Future study will necessitate systematic, epoch-on-epoch interferometric observation of variable Be stars. Preferably this will be combined with contemporaneous recording of other observables, such as emission line spectroscopy consistent with wavelength regime of the interferometry. Combining the two will strengthen claims of changes to the observational signatures between epochs, allow for cross-checking of model parameters, and ultimately help us improve the descriptions we make about the physics within the disks.

References

Armstrong, J. T., Mozurkewich, D., Rickard, L. J., et al. (1998). *ApJ* 496, p. 550. DOI: 10.1086/305365.

Balona, L. A. (1995). *MNRAS* 277, p. 1547. DOI: 10.1093/mnras/277.4.1547.

Cox, A. N. (2000). New York: AIP Press; Springer.

Delaa, O., Stee, P., Meilland, A., et al. (2011). *A & A* 529, A87, A87 (D11). DOI: 10.1051/0004-6361/201015639.

Dougherty, S. M. and Taylor, A. R. (1992). *Nature* 359, pp. 808–810. DOI: 10.1038/359808a0.

Draper, Z. H., Wisniewski, J. P., Bjorkman, K. S., et al. (2014). *ApJ* 786, 120, p. 120. DOI: 10.1088/0004-637X/786/2/120. arXiv: 1402.5240 [astro-ph.SR].

Hall, J. C., Fulton, E. E., Huenemoerder, D. P., et al. (1994). *PASP* 106, pp. 315–326. DOI: 10.1086/133381.

Hiltner, W. A., Garrison, R. F., and Schild, R. E. (1969). *ApJ* 157, p. 313. DOI: 10.1086/150069.

Hubert, A. M. and Floquet, M. (1998). *A & A* 335, pp. 565–572.

Jones, C. E., Tycner, C., and Smith, A. D. (2011). *AJ* 141, 150, p. 150. DOI: 10.1088/0004-6256/141/5/150. arXiv: 1103.1514 [astro-ph.SR].

Lesh, J. R. (1968). *ApJS* 17, p. 371. DOI: 10.1086/190179.

Miczaika, G. R. (1951). *Zeitschrift für Astrophysik* 29, p. 262.

Porter, J. M. and Rivinius, T. (2003). *PASP* 115, pp. 1153–1170. DOI: 10.1086/378307.

Quirrenbach, A., Hummel, C. A., Buscher, D. F., et al. (1993). *ApJL* 416, p. L25. DOI: 10.1086/187062.

Quirrenbach, A., Bjorkman, K. S., Bjorkman, J. E., et al. (1997). *ApJ* 479, 477 (Q97). DOI: 10.1086/303854.

Rivinius, T., Carciofi, A. C., and Martayan, C. (2013). *A & Ar* 21, 69, p. 69. DOI: 10.1007/s00159-013-0069-0. arXiv: 1310.3962 [astro-ph.SR].

Rivinius, T., Štefl, S., and Baade, D. (2006). *A & A* 459, pp. 137–145. DOI: 10.1051/0004-6361:20053008.

Shao, M., Colavita, M. M., Hines, B. E., et al. (1988). *A & A* 193, pp. 357–371.

Sigut, T. A. A. (2011). In: *IAU Symposium*. Ed. by C. Neiner, G. Wade, G. Meynet, et al. Vol. 272. IAU Symposium, pp. 426–427. DOI: 10.1017/S1743921311011045.

Sigut, T. A. A. and Jones, C. E. (2007). *ApJ* 668, pp. 481–491. DOI: 10.1086/521209. arXiv: 0706.4036.

Struve, O. (1931). *ApJ* 73, p. 94. DOI: 10.1086/143298.

Tycner, C., Gilbreath, G. C., Zavala, R. T., et al. (2006). *AJ* 131, pp. 2710–2721. DOI: 10.1086/502679. eprint: astro-ph/0602087.

van Leeuwen, F. (2007). *A & A* 474, pp. 653–664. DOI: 10.1051/0004-6361:20078357. arXiv: 0708.1752.

Waters, L. B. F. M. (1986). *A & A* 162, pp. 121–139.

Wisniewski, J. P., Kowalski, A. F., Bjorkman, K. S., et al. (2007). *ApJL* 656, pp. L21–L24. DOI: 10.1086/512123. eprint: arXiv:astro-ph/0701010.

Wisniewski, J. P., Draper, Z. H., Bjorkman, K. S., et al. (2010). *ApJ* 709, pp. 1306–1320. DOI: 10.1088/0004-637X/709/2/1306. arXiv: 0912.1504 [astro-ph.SR].

"...and the stars look very different today."

David Bowie, "Space Oddity"

5 Conclusions

5.1 The Projects

In this work we have combined three studies of B-emission star disks based primarily on interferometric data. A number of modelling modalities were employed, ranging from relatively simple geometrical disk models to describe the overall shape and size of the extended disk structure to the sophisticated and detailed models computed with the Bedisk-Beray-2dDFT pipeline.

5.1.1 PTI

Chapter 2 dealt with underutilized observational data contained within the Palomar Testbed Interferometer (PTI) database. Data are available for a range of spectral types, wind structures, binarity states and level of variability. For the PTI project we extracted and analyzed K-band interferometry for sixteen stars; full analyses were performed for the thirteen stars which had sufficient data.

We assembled a collection of uniform disk and numerical disk models for comparison with K-band interferometric observations for sixteen Be stars spanning spectral types from B0 to B8. Uniform disk models for sixteen targets were fitted to K-band archival observations from the Palomar Testbed Interferometer. We also determined the disk density distribution using numerical models constructed with the non-LTE radiative code Bedisk (Sigut and Jones, 2007) for thirteen of the sixteen stars, as it was determined that one star did not have sufficient data for analysis. Our collection of numerical models has the distinction of being thermally

balanced in addition to having been generated with solar chemical composition.

By combining the results from all our targets, we find best-fit models corresponding to model input parameters that ranged substantially in value with $1.0 < n < 6.5$ and $1.0 \times 10^{-12} < \rho_0 < 3.0 \times 10^{-8}$ g $\cdot$ cm^{-3}. A simple average value of n over all of our program stars for our preferred models is 3.03 ± 0.94. This result is in good agreement with other investigations of Be star disks in the infrared regime (Gies et al., 2007; Waters, Coté, and Lamers, 1987).

5.1.2 48 Persei

The study in Chapter 3 was an in-depth analysis of the Be star 48 Per. Large sets of observations with exceptional (u, v) plane coverage were acquired at NPOI for 48 Per. For 48 Per, 291 observations were recorded in November and December of 2006. Spectral lines in Hα were also acquired for contemporaneously for 48 Per. Given its stability, 48 Per represents a simpler case. Our findings were generally consistent with those published by Q97 and D11. Previous studies have found 48 Per to be inclined at approximately 30-35°, whereas our results are more consistent with a disk inclined at approximately 45°. Estimates of the PA for the disk surrounding 48 Per were made as well; using a GD model, we calculated PA = $122 \pm 3°$ for the major axis. D11 reports their result of $115 \pm 33°$, which agrees well with our measurement. Q97 reported $81 \pm 43°$ and 68° as the PAs associated with their regular and modified GD fits, respectively.

48 Per has a moderately dense disk with values of $n \sim 2$ to 3 and log $\rho_0 \sim$-11.8 to -9.4 or $\rho_0 \sim 2.0 \times 10^{-12}$ to 4.0×10^{-10} g $\cdot$ cm^{-3}, respectively from the the spectroscopy and interferometry analysis. The radial extent with all of the best-fitting models for the Hα and V^2 fits correspond to the largest disks ($50R_*$) in our grid. The results from the spectroscopy and interferometry show agreement with a combined best-fit of $n = 2.25$ and $\log \rho_0 = -11.1$ or $\rho_0 = 7.94 \times 10^{-12}$ g $\cdot$ cm^{-3} corresponding to the dashed lines on Figure 3.9. The SED fitting suggests that a much denser disk of relatively small radial extent is required to fit the infrared wavelength regime. The best-fitting SED has an n of 4.0 and ρ_0 of 2.5×10^{-10} g $\cdot$ cm^{-3} as shown by the blue line on Figure 3.8 and shaded circle on Figure 3.9.

By taking our best-fit combined model with parameters with n and log ρ_0 of 2.25 and = -11.1, respectively, obtained from interferometry and spectroscopy we calculated a better approximation for the radial extent of the Hα emitting region by integrating the corresponding interferometric image associated with these parameters until the radial extent of the disk included 90% of the Hα flux. We obtain a disk size of $R_{90}/R_* = 28.4$ with this method, which is typical for the size of the Hα emitting region of a Be star disk.

5.1.3 ψ Per

The situation associated with ψ Per was very different. Studies such as Draper et al. (2014) describe variation in the polarization signature of ψ Per contemporaneous with our interferometry collected in 2010. This is a fortuitous coincidence; very few studies of the effects of variability on interferometric observation exist. Having two epochs of observation included in our data set is a unique opportunity to examine the changes in disk structure over time. Specifically, Figure 4.8 shows that when the 2006 and 2010 observations were compared to the best-fit model for 2006, the 2010 data did not match the 2006 model fit, indicating that the disk density structure may have changed. Such a signature has not been reported previously.

The (n, ρ_0, i) parameters for the best Hα and V^2 fits for 2006 did not exactly align, however the (n, ρ_0, i) of the best 10% models overall coincide in two regions seen in Figure 4.9. The Figure shows two sets of points: orange, marking the points on the (n, ρ_0) space where the best 10% of the interferometric models occurred, and the blue points indicating the same for spectroscopy. The intersecting regions run from $2.0 \leq n \leq 2.3$ with $5.0 \times 10^{-12} \leq \rho_0 \leq 1.0 \times 10^{-11}$ g $\cdot$ cm^{-3} and $2.5 \leq n \leq 2.7$ with $2.0 \times 10^{-11} \leq \rho_0 \leq 7.0 \times 10^{-11}$ g $\cdot$ cm^{-3}. The best fitting model parameters change from $n = 2.5$, $\rho_0 = 4.0 \times 10^{-11}$ g $\cdot$ cm^{-3}, $i = 75°$ for 2006 to $n = 2.0$, $\rho_0 = 5.0 \times 10^{-12}$ g $\cdot$ cm^{-3}, $i = 75°$ for 2010. This is a key finding of this study, as it is the first time an interferometric signature of variability has been detected. Furthermore, the reduction in ρ_0 during this time period is consistent with the suggestion of partial disk loss by Draper et al. (2014).

We also calculated position angles (PAs) for the major axis of the disk on the sky with respect to north, which are summarized in Table 4.6. For ψ Per, we obtained an estimate of $135 \pm 3°$. Draper et al. 2014 also modelled ψ Per and obtained a field-star estimate of $112 \pm 11°$ for the PA of ψ Per.

Both UD and GD fits were applied to the observations in order to estimate the ratio of the disk's minor and major axes. From these quantities estimates were a first-order approximation of the actual physical extent of the disk, which subsequently can be compared to model results. As seen in Table 4.7, applying a UD fit to our 2006 interferometry gives an axis ratio of 0.38 ± 0.16 whereas the axis ratio corresponding to the GD fit is 0.34 ± 0.02. Q97 made axis ratio estimates of 0.47 ± 0.11 (GD). In the review by Rivinius, Carciofi, and Martayan 2013, table 2 gives a summary of GD sizes organized by emitting region.

The review by Rivinius, Carciofi, and Martayan (2013) reanalyzed published estimates of various emission regions for several Be star disks. For ψ Per they assumed a $4.7 R_\odot$ central star rather than the $3.9 R_\odot$ central star used in this study, as well as 80% flux enclosure. After their

analysis, Rivinius, Carciofi, and Martayan (2013) report that the extent of the Hα emission region surrounding ψ Per extends to $13.34 \pm 0.94 R_*$, based on the published results in Q97. Our estimate for the Hα region, based on our best V^2 model for 2006, is that a disk enclosing 75% of the Hα flux extends to $9.2 R_*$. Similarly, for 2010 we compute a disk extent of $30 R_*$. Given the differences between the central star models and the proportion of the Hα region that each model encloses, we find our result to be in reasonable agreement with Rivinius, Carciofi, and Martayan (2013).

5.2 Avenues for Future Research

The non-LTE modelling routines Bedisk and Beray calculate very detailed models of the disk environment down to the atomic level. Bedisk models contain significant amounts of information regarding level populations, heating and cooling processes and the like. As mentioned in Chapters 3 and 4 we had difficulty matching the wings of the Hα spectra. In future it may be appropriate to develop a method for approximating noncoherent electron scattering so these models can include this process. As well, our codes employed one value of the power law n. It would be interesting to develop models that could have varying values of n with distance from the star.

As the facilities and techniques related to interferometry continue to improve, future observing campaigns should emphasize acquisition of the most comprehensive data sets possible. For example, contemporaneous Hα spectroscopy was not available for all epochs in the ψ Per study. While our data were well constrained, having complete sets of spectrointerferometric data would improve the constraints further and allow us to quantify the changes in ψ Per more precisely. Doing so could potentially allow us to relate specific changes in spectral line profiles to co-occurring changes in the interferometric signature, which may allow for greater predictability and characterization of variability. Given the detection of an interferometric signature of variability for ψ Per and other Be stars, future research efforts should be focussed on obtaining similarly comprehensive multiepoch observations of variable Be stars.

One "wish list" item for interferometry is to develop an instrument capable of observing in multiple wavelengths simultaneously. The clear advantage of such a facility is that one would have a comprehensive set of observations taken from precisely the same projected baseline and subject to identical atmospheric conditions. The resulting observations could be used to probe different regions of the disk where emission from various wavelengths originate, providing exceptionally clear snapshots of the star and its extended structure. Finally, additional baselines added to interferometric facilities would provide greater (u, v) coverage, allowing stronger constraints on models.

The development of dynamic models capable of following disk structure as it evolves with time depends on accurate disk physical conditions. My thesis work contributes to this goal, and with the "wish list" items described above finer details of disk structure could be probed.

References

Draper, Z. H., Wisniewski, J. P., Bjorkman, K. S., et al. (2014). *ApJ* 786, 120, p. 120. DOI: 10.1088/0004-637X/786/2/120. arXiv: 1402.5240 [astro-ph.SR].

Gies, D. R., Bagnuolo Jr., W. G., Baines, E. K., et al. (2007). *Astrophysical Journal* 654, pp. 527–543. DOI: 10.1086/509144. eprint: astro-ph/0609501.

Rivinius, T., Carciofi, A. C., and Martayan, C. (2013). *A & Ar* 21, 69, p. 69. DOI: 10.1007/s00159-013-0069-0. arXiv: 1310.3962 [astro-ph.SR].

Sigut, T. A. A. and Jones, C. E. (2007). *ApJ* 668, pp. 481–491. DOI: 10.1086/521209. arXiv: 0706.4036.

Waters, L. B. F. M., Coté, J., and Lamers, H. J. G. L. M. (1987). *A & A* 185, pp. 206–224.

A

NPOI Observations for 48 Per

JD-2,450,000	u (m)	v (m)	V^2 (arbitrary)	Baseline
4046.749	17.189	−21.882	0.834 ± 0.026	AC-AE
4046.749	−29.224	0.422	0.849 ± 0.033	AC-AW
4046.782	21.140	−18.991	0.854 ± 0.062	AC-AE
4046.782	−30.994	−4.121	0.893 ± 0.128	AC-AW
4046.815	24.338	−15.402	0.793 ± 0.040	AC-AE
4046.815	−31.480	−9.050	0.935 ± 0.046	AC-AW
4046.846	26.281	−11.819	0.836 ± 0.025	AC-AE
4046.846	−30.710	−13.453	0.871 ± 0.041	AC-AW
4046.867	27.082	−9.152	0.932 ± 0.026	AC-AE
4046.867	−29.490	−16.462	0.839 ± 0.024	AC-AW
4047.003	20.853	7.050	0.813 ± 0.039	AC-AE
4047.003	20.012	73.182	0.717 ± 0.043	AC-W7
4047.003	40.865	80.232	0.757 ± 0.035	AE-W7
4047.003	−10.945	−30.129	1.016 ± 0.064	AC-AW
4047.003	20.003	73.148	0.716 ± 0.029	AC-W7
4047.003	9.057	43.019	0.858 ± 0.029	AW-W7
4047.061	13.057	11.725	0.893 ± 0.059	AC-AE
4047.061	0.424	−31.579	0.901 ± 0.083	AC-AW

JD-2,450,000	u (m)	v (m)	V^2 (arbitrary)	Baseline
4047.733	15.259	−22.934	0.843 ± 0.042	AC-AE
4047.733	−28.085	2.278	0.874 ± 0.044	AC-AW
4047.765	19.563	−20.288	0.835 ± 0.034	AC-AE
4047.765	−30.396	−2.164	0.938 ± 0.049	AC-AW
4047.793	22.637	−17.515	0.868 ± 0.019	AC-AE
4047.793	−31.375	−6.224	0.801 ± 0.018	AC-AW
4047.814	24.483	−15.192	0.844 ± 0.036	AC-AE
4047.814	−31.465	−9.321	0.871 ± 0.026	AC-AW
4047.836	25.948	−12.598	0.799 ± 0.023	AC-AE
4047.836	−30.967	−12.533	0.931 ± 0.041	AC-AW
4047.859	26.938	−9.783	0.828 ± 0.023	AC-AE
4047.859	−29.824	−15.769	0.885 ± 0.039	AC-AW
4047.951	25.252	1.763	0.776 ± 0.046	AC-AE
4047.951	39.621	66.343	0.719 ± 0.051	AC-W7
4047.951	64.873	68.106	0.741 ± 0.040	AE-W7
4047.951	−19.371	−26.652	0.935 ± 0.089	AC-AW
4047.951	39.603	66.313	0.811 ± 0.043	AC-W7
4047.951	20.232	39.661	0.875 ± 0.044	AW-W7
4048.759	19.190	−20.565	0.831 ± 0.025	AC-AE
4048.759	−30.232	−1.732	0.927 ± 0.039	AC-AW
4048.808	24.216	−15.575	0.844 ± 0.013	AC-AE
4048.808	−31.488	−8.827	0.915 ± 0.019	AC-AW
4048.833	25.906	−12.689	0.804 ± 0.028	AC-AE
4048.833	−30.994	−12.425	0.923 ± 0.029	AC-AW
4048.853	26.820	−10.230	0.828 ± 0.016	AC-AE
4048.853	−30.044	−15.271	0.987 ± 0.041	AC-AW
4048.872	27.300	−7.786	0.836 ± 0.040	AC-AE
4048.872	−28.672	−17.922	0.937 ± 0.045	AC-AW
4048.940	25.819	0.680	0.818 ± 0.054	AC-AE
4048.940	42.915	64.592	0.678 ± 0.050	AC-W7
4048.940	68.734	65.272	0.762 ± 0.027	AE-W7
4048.940	−20.762	−25.801	0.987 ± 0.075	AC-AW
4048.940	42.895	64.563	0.746 ± 0.027	AC-W7

JD-2,450,000	u (m)	v (m)	V^2 (arbitrary)	Baseline
4048.940	22.133	38.762	0.870 ± 0.027	AW-W7
4049.002	20.391	7.441	0.872 ± 0.059	AC-AE
4049.002	18.265	73.545	0.758 ± 0.064	AC-W7
4049.002	38.656	80.986	0.701 ± 0.053	AE-W7
4049.002	−10.185	−30.329	1.105 ± 0.067	AC-AW
4049.002	18.257	73.511	0.686 ± 0.052	AC-W7
4049.002	8.072	43.182	0.835 ± 0.037	AW-W7
4049.056	−5.654	75.152	0.737 ± 0.066	AC-W7
4049.056	0.369	−31.580	0.871 ± 0.077	AC-AW
4049.056	−5.651	75.117	0.807 ± 0.069	AC-W7
4049.056	−5.282	43.537	0.767 ± 0.079	AW-W7
4049.753	18.692	−20.917	0.890 ± 0.021	AC-AE
4049.753	−30.000	−1.172	0.927 ± 0.033	AC-AW
4049.829	25.814	−12.885	0.859 ± 0.024	AC-AE
4049.829	−31.049	−12.190	0.889 ± 0.027	AC-AW
4049.853	26.903	−9.923	0.891 ± 0.024	AC-AE
4049.853	−29.895	−15.614	0.903 ± 0.027	AC-AW
4049.961	24.108	3.532	0.863 ± 0.060	AC-AE
4049.961	−16.881	−27.951	0.971 ± 0.067	AC-AW
4050.019	17.962	9.210	0.939 ± 0.055	AC-AE
4050.019	−6.405	−31.094	0.942 ± 0.063	AC-AW
4050.751	18.765	−20.866	0.912 ± 0.040	AC-AE
4050.751	−30.035	−1.253	0.919 ± 0.049	AC-AW
4050.797	23.758	−16.191	0.903 ± 0.020	AC-AE
4050.797	−31.495	−8.018	0.821 ± 0.047	AC-AW
4050.823	25.659	−13.199	0.820 ± 0.014	AC-AE
4050.823	−31.133	−11.810	0.858 ± 0.038	AC-AW
4050.846	26.760	−10.436	0.854 ± 0.025	AC-AE
4050.846	−30.141	−15.040	0.924 ± 0.057	AC-AW
4050.957	24.205	3.398	0.840 ± 0.033	AC-AE
4050.957	34.234	68.785	0.800 ± 0.035	AC-W7
4050.957	58.438	72.183	0.732 ± 0.034	AE-W7
4050.957	−17.079	−27.857	0.876 ± 0.109	AC-AW

JD-2,450,000	u (m)	v (m)	V^2 (arbitrary)	Baseline
4050.957	34.218	68.753	0.731 ± 0.025	AC-W7
4050.957	17.138	40.896	0.815 ± 0.024	AW-W7
4053.760	−30.913	−3.805	0.878 ± 0.080	AC-AW
4054.755	20.666	−19.404	0.902 ± 0.013	AC-AE
4054.755	−30.833	−3.509	0.891 ± 0.021	AC-AW
4054.791	24.174	−15.634	0.921 ± 0.023	AC-AE
4054.791	−31.491	−8.750	0.835 ± 0.039	AC-AW
4054.818	25.986	−12.514	0.847 ± 0.022	AC-AE
4054.818	−30.941	−12.633	0.906 ± 0.022	AC-AW
4054.842	27.002	−9.519	0.868 ± 0.032	AC-AE
4054.842	−29.688	−16.060	0.880 ± 0.030	AC-AW
4054.861	27.363	−7.079	0.919 ± 0.024	AC-AE
4054.861	−28.198	−18.658	0.890 ± 0.037	AC-AW
4055.747	19.977	−19.969	0.855 ± 0.032	AC-AE
4055.747	−30.569	−2.657	0.929 ± 0.031	AC-AW
4055.780	23.439	−16.591	0.870 ± 0.031	AC-AE
4055.780	−31.479	−7.484	0.843 ± 0.056	AC-AW
4055.817	26.059	−12.351	0.836 ± 0.036	AC-AE
4055.817	−30.890	−12.826	0.878 ± 0.039	AC-AW
4055.833	26.801	−10.295	0.886 ± 0.024	AC-AE
4055.833	−30.075	−15.198	0.907 ± 0.026	AC-AW
4055.851	27.262	−8.094	0.875 ± 0.030	AC-AE
4055.851	−28.867	−17.597	0.886 ± 0.051	AC-AW
4055.977	21.004	6.918	0.932 ± 0.037	AC-AE
4055.977	20.591	73.054	0.743 ± 0.046	AC-W7
4055.977	41.595	79.972	0.720 ± 0.049	AE-W7
4055.977	−11.197	−30.059	0.958 ± 0.039	AC-AW
4055.977	20.581	73.020	0.751 ± 0.022	AC-W7
4055.977	9.384	42.961	0.850 ± 0.037	AW-W7
4056.018	15.885	10.420	0.977 ± 0.051	AC-AE
4056.018	2.832	75.277	0.751 ± 0.050	AC-W7
4056.018	18.717	85.697	0.703 ± 0.061	AE-W7
4056.018	−3.404	−31.445	0.748 ± 0.092	AC-AW

JD-2,450,000	u (m)	v (m)	V^2 (arbitrary)	Baseline
4056.018	2.831	75.243	0.667 ± 0.048	AC-W7
4056.018	−0.573	43.798	0.770 ± 0.041	AW-W7
4056.751	20.780	−19.302	0.856 ± 0.025	AC-AE
4056.751	−30.886	−3.671	0.891 ± 0.017	AC-AW
4056.758	21.554	−18.605	0.828 ± 0.017	AC-AE
4056.758	−31.131	−4.693	0.816 ± 0.026	AC-AW
4056.790	24.524	−15.128	0.839 ± 0.020	AC-AE
4056.790	−31.464	−9.416	0.810 ± 0.020	AC-AW
4056.810	25.821	−12.871	0.816 ± 0.016	AC-AE
4056.810	−31.046	−12.219	0.922 ± 0.021	AC-AW
4056.827	26.655	−10.782	0.840 ± 0.015	AC-AE
4056.827	−30.293	−14.661	0.879 ± 0.021	AC-AW
4056.843	27.154	−8.799	0.867 ± 0.026	AC-AE
4056.843	−29.285	−16.856	0.891 ± 0.028	AC-AW
4056.860	27.391	−6.610	0.848 ± 0.020	AC-AE
4056.860	−27.857	−19.150	0.861 ± 0.018	AC-AW
4056.951	23.398	4.465	0.859 ± 0.037	AC-AE
4056.951	30.478	70.229	0.708 ± 0.024	AC-W7
4056.951	53.876	74.694	0.714 ± 0.039	AE-W7
4056.951	−15.429	−28.588	0.849 ± 0.034	AC-AW
4056.951	30.464	70.196	0.727 ± 0.021	AC-W7
4056.951	15.034	41.608	0.809 ± 0.021	AW-W7
4056.987	19.564	8.111	0.846 ± 0.072	AC-AE
4056.987	−8.812	−30.645	0.894 ± 0.068	AC-AW
4056.987	15.228	74.074	0.790 ± 0.036	AC-W7
4056.987	6.416	43.428	0.765 ± 0.046	AW-W7
4056.991	19.087	8.462	0.902 ± 0.033	AC-AE
4056.991	13.533	74.369	0.801 ± 0.033	AC-W7
4056.991	32.620	82.831	0.686 ± 0.034	AE-W7
4056.991	−8.066	−30.799	0.885 ± 0.048	AC-AW
4056.991	13.527	74.335	0.819 ± 0.029	AC-W7
4056.991	5.461	43.536	0.857 ± 0.023	AW-W7
4057.020	15.209	10.780	0.948 ± 0.028	AC-AE

JD-2,450,000	u (m)	v (m)	V^2 (arbitrary)	Baseline
4057.020	0.729	75.333	0.716 ± 0.028	AC-W7
4057.020	15.938	86.113	0.780 ± 0.045	AE-W7
4057.020	−2.415	−31.507	0.875 ± 0.035	AC-AW
4057.020	0.728	75.299	0.740 ± 0.031	AC-W7
4057.020	−1.687	43.791	0.799 ± 0.019	AW-W7
4057.049	10.770	12.559	0.854 ± 0.032	AC-AE
4057.049	−12.262	74.543	0.755 ± 0.040	AC-W7
4057.049	−1.493	87.102	0.670 ± 0.042	AE-W7
4057.049	3.388	−31.441	0.834 ± 0.058	AC-AW
4057.049	−12.257	74.509	0.742 ± 0.035	AC-W7
4057.049	−8.869	43.069	0.802 ± 0.032	AW-W7
4057.974	20.779	7.114	0.887 ± 0.038	AC-AE
4057.974	19.730	73.243	0.724 ± 0.055	AC-W7
4057.974	40.509	80.357	0.746 ± 0.049	AE-W7
4057.974	−10.823	−30.162	0.925 ± 0.108	AC-AW
4057.974	19.721	73.209	0.669 ± 0.053	AC-W7
4057.974	8.898	43.047	0.865 ± 0.037	AW-W7
4058.008	16.405	10.139	0.928 ± 0.039	AC-AE
4058.008	4.495	75.213	0.771 ± 0.031	AC-W7
4058.008	20.900	85.352	0.751 ± 0.029	AE-W7
4058.008	−4.139	−31.379	0.780 ± 0.067	AC-AW
4058.008	4.493	75.179	0.749 ± 0.026	AC-W7
4058.008	0.353	43.800	0.730 ± 0.057	AW-W7
4058.031	13.152	11.687	0.915 ± 0.046	AC-AE
4058.031	−5.498	75.161	0.655 ± 0.048	AC-W7
4058.031	7.654	86.848	0.713 ± 0.032	AE-W7
4058.031	0.300	−31.580	0.863 ± 0.033	AC-AW
4058.031	−5.496	75.127	0.710 ± 0.021	AC-W7
4058.031	−5.196	43.546	0.857 ± 0.041	AW-W7
4058.056	9.157	13.010	0.902 ± 0.036	AC-AE
4058.056	−16.665	73.847	0.740 ± 0.062	AC-W7
4058.056	−7.507	86.857	0.744 ± 0.040	AE-W7
4058.056	5.311	−31.248	0.943 ± 0.085	AC-AW

JD-2,450,000	u (m)	v (m)	V^2 (arbitrary)	Baseline
4058.056	−16.657	73.813	0.786 ± 0.039	AC-W7
4058.056	−11.346	42.565	0.819 ± 0.045	AW-W7
4059.978	19.594	8.071	0.878 ± 0.043	AC-AE
4059.978	15.340	74.074	0.791 ± 0.046	AC-W7
4059.978	−8.908	−30.630	0.820 ± 0.074	AC-AW
4059.978	15.333	74.040	0.768 ± 0.039	AC-W7
4059.978	6.425	43.410	0.760 ± 0.051	AW-W7
4060.037	11.327	12.362	1.011 ± 0.072	AC-AE
4060.037	−10.735	74.713	0.805 ± 0.098	AC-W7
4060.037	0.592	87.075	0.852 ± 0.364	AE-W7
4060.037	2.643	−31.499	0.902 ± 0.133	AC-AW
4060.037	−10.730	74.679	0.844 ± 0.079	AC-W7
4060.037	−8.087	43.180	0.833 ± 0.069	AW-W7
4060.041	10.735	12.555	0.898 ± 0.047	AC-AE
4060.041	−12.381	74.511	0.695 ± 0.045	AC-W7
4060.041	3.382	−31.447	0.889 ± 0.048	AC-AW
4060.041	−12.376	74.477	0.835 ± 0.035	AC-W7
4060.041	−8.993	43.031	0.818 ± 0.027	AW-W7
4060.044	10.226	12.711	0.936 ± 0.029	AC-AE
4060.044	−13.781	74.317	0.681 ± 0.061	AC-W7
4060.044	4.012	−31.392	0.920 ± 0.048	AC-AW
4060.044	−13.774	74.283	0.731 ± 0.038	AC-W7
4060.044	−9.763	42.891	0.860 ± 0.030	AW-W7
4060.049	9.459	12.929	0.915 ± 0.069	AC-AE
4060.049	−15.856	73.988	0.661 ± 0.104	AC-W7
4060.049	4.946	−31.292	0.876 ± 0.037	AC-AW
4060.049	−15.849	73.954	0.817 ± 0.055	AC-W7
4060.049	−10.902	42.662	0.832 ± 0.040	AW-W7
4060.052	8.916	13.072	0.921 ± 0.052	AC-AE
4060.052	−17.305	73.729	0.734 ± 0.107	AC-W7
4060.052	5.601	−31.210	0.951 ± 0.062	AC-AW
4060.052	−17.297	73.696	0.818 ± 0.042	AC-W7
4060.052	−11.697	42.486	0.800 ± 0.043	AW-W7

JD-2,450,000	u (m)	v (m)	V^2 (arbitrary)	Baseline
4060.058	7.901	13.315	0.949 ± 0.035	AC-AE
4060.058	−19.964	73.192	0.667 ± 0.087	AC-W7
4060.058	6.803	−31.031	0.839 ± 0.057	AC-AW
4060.058	−19.955	73.159	0.781 ± 0.046	AC-W7
4060.058	−13.152	42.128	0.891 ± 0.056	AW-W7
4060.930	24.253	3.349	0.868 ± 0.032	AC-AE
4060.930	34.455	68.707	0.726 ± 0.027	AC-W7
4060.930	58.709	72.056	0.716 ± 0.051	AE-W7
4060.930	−17.136	−27.825	0.837 ± 0.035	AC-AW
4060.930	34.439	68.676	0.761 ± 0.029	AC-W7
4060.930	17.304	40.850	0.825 ± 0.030	AW-W7
4060.996	17.002	9.815	0.863 ± 0.038	AC-AE
4060.996	6.445	75.118	0.773 ± 0.053	AC-W7
4060.996	23.447	84.933	0.699 ± 0.054	AE-W7
4060.996	−4.947	−31.287	0.762 ± 0.063	AC-AW
4060.996	6.442	75.084	0.773 ± 0.047	AC-W7
4060.996	1.495	43.797	0.858 ± 0.025	AW-W7
4061.037	11.014	12.481	0.903 ± 0.035	AC-AE
4061.037	−11.586	74.629	0.772 ± 0.088	AC-W7
4061.037	−0.572	87.110	0.712 ± 0.041	AE-W7
4061.037	3.084	−31.464	0.814 ± 0.062	AC-AW
4061.037	−11.580	74.595	0.794 ± 0.049	AC-W7
4061.037	−8.496	43.131	0.827 ± 0.022	AW-W7
4061.040	10.387	12.678	0.877 ± 0.071	AC-AE
4061.040	−13.317	74.400	0.619 ± 0.139	AC-W7
4061.040	−2.930	87.078	0.803 ± 0.114	AE-W7
4061.040	3.862	−31.400	0.886 ± 0.109	AC-AW
4061.040	−13.311	74.366	0.720 ± 0.112	AC-W7
4061.040	−9.448	42.966	0.781 ± 0.057	AW-W7
4061.045	9.725	12.871	0.931 ± 0.033	AC-AE
4061.045	−15.115	74.127	0.765 ± 0.059	AC-W7
4061.045	−5.390	86.998	0.724 ± 0.039	AE-W7
4061.045	4.672	−31.318	0.852 ± 0.045	AC-AW

JD-2,450,000	u (m)	v (m)	V^2 (arbitrary)	Baseline
4061.045	−15.108	74.093	0.714 ± 0.028	AC-W7
4061.045	−10.436	42.775	0.821 ± 0.029	AW-W7
4061.049	9.054	13.052	0.926 ± 0.056	AC-AE
4061.049	−16.912	73.818	0.808 ± 0.115	AC-W7
4061.049	−7.858	86.870	0.717 ± 0.098	AE-W7
4061.049	5.483	−31.220	0.872 ± 0.125	AC-AW
4061.049	−16.904	73.784	0.848 ± 0.125	AC-W7
4061.049	−11.421	42.564	0.779 ± 0.080	AW-W7
4061.053	8.435	13.206	0.886 ± 0.080	AC-AE
4061.053	−18.545	73.505	0.650 ± 0.128	AC-W7
4061.053	−10.110	86.711	0.689 ± 0.100	AE-W7
4061.053	6.221	−31.117	1.029 ± 0.081	AC-AW
4061.053	−18.536	73.472	0.673 ± 0.084	AC-W7
4061.053	−12.315	42.355	0.840 ± 0.038	AW-W7
4061.923	24.573	2.885	0.926 ± 0.045	AC-AE
4061.923	36.030	68.038	0.717 ± 0.039	AC-W7
4061.923	60.603	70.922	0.733 ± 0.038	AE-W7
4061.923	−17.809	−27.493	0.941 ± 0.059	AC-AW
4061.923	36.013	68.007	0.740 ± 0.023	AC-W7
4061.923	18.205	40.513	0.801 ± 0.018	AW-W7
4061.986	17.952	9.233	0.896 ± 0.045	AC-AE
4061.986	9.610	74.851	0.752 ± 0.037	AC-W7
4061.986	27.562	84.083	0.744 ± 0.026	AE-W7
4061.986	−6.342	−31.099	0.807 ± 0.062	AC-AW
4061.986	9.605	74.816	0.748 ± 0.022	AC-W7
4061.986	3.263	43.718	0.838 ± 0.037	AW-W7
4062.018	13.389	11.605	0.948 ± 0.050	AC-AE
4062.018	−4.779	75.216	0.693 ± 0.027	AC-W7
4062.018	8.610	86.821	0.766 ± 0.036	AE-W7
4062.018	0.037	−31.576	0.929 ± 0.065	AC-AW
4062.018	−4.777	75.182	0.722 ± 0.037	AC-W7
4062.018	−4.741	43.606	0.828 ± 0.029	AW-W7
4062.040	10.000	12.792	0.979 ± 0.034	AC-AE

JD-2,450,000	u (m)	v (m)	V^2 (arbitrary)	Baseline
4062.040	−14.371	74.244	0.688 ± 0.041	AC-W7
4062.040	−4.371	87.037	0.740 ± 0.030	AE-W7
4062.040	4.337	−31.354	0.907 ± 0.075	AC-AW
4062.040	−14.365	74.210	0.738 ± 0.027	AC-W7
4062.040	−10.028	42.856	0.810 ± 0.039	AW-W7
4062.977	18.783	8.661	0.943 ± 0.079	AC-AE
4062.977	12.461	74.501	0.558 ± 0.114	AC-W7
4062.977	31.244	83.162	0.640 ± 0.095	AE-W7
4062.977	12.455	74.467	0.660 ± 0.122	AC-W7

B

NPOI Observations for ψ Per, 2006 and 2010

JD-2,450,000	u (m)	v (m)	V^2 (arbitrary)	Baseline
4046.741	18.963	−20.782	0.721 ± 0.024	AC-AE
4046.741	−30.128	−1.345	0.853 ± 0.036	AC-AW
4046.777	22.937	−17.209	0.770 ± 0.035	AC-AE
4046.777	−31.424	−6.594	0.906 ± 0.060	AC-AW
4046.811	25.630	−13.253	0.744 ± 0.018	AC-AE
4046.811	−31.147	−11.691	0.853 ± 0.036	AC-AW
4046.841	26.976	−9.598	0.701 ± 0.203	AC-AE
4046.841	−29.744	−15.922	1.081 ± 0.266	AC-AW
4046.864	27.381	−6.683	0.799 ± 0.042	AC-AE
4046.864	−27.956	−19.015	0.850 ± 0.049	AC-AW
4046.991	19.610	8.225	0.892 ± 0.051	AC-AE
4046.991	15.395	74.242	0.709 ± 0.047	AC-W7
4046.991	35.005	82.467	0.721 ± 0.045	AE-W7
4046.991	−8.932	−30.718	0.868 ± 0.098	AC-AW
4046.991	15.388	74.208	0.703 ± 0.041	AC-W7
4046.991	6.456	43.489	0.795 ± 0.032	AW-W7

JD-2,450,000	u (m)	v (m)	V^2 (arbitrary)	Baseline
4047.053	10.986	12.673	1.007 ± 0.060	AC-AE
4047.053	−11.685	74.781	0.649 ± 0.074	AC-W7
4047.053	−0.699	87.455	0.664 ± 0.055	AE-W7
4047.053	3.070	−31.571	0.787 ± 0.064	AC-AW
4047.053	−11.680	74.747	0.606 ± 0.046	AC-W7
4047.053	−8.610	43.176	0.726 ± 0.041	AW-W7
4047.726	17.415	−21.809	0.727 ± 0.025	AC-AE
4047.726	−29.347	0.333	0.940 ± 0.110	AC-AW
4047.761	21.639	−18.567	0.750 ± 0.035	AC-AE
4047.761	−31.144	−4.688	0.783 ± 0.029	AC-AW
4047.790	24.319	−15.445	0.757 ± 0.020	AC-AE
4047.790	−31.481	−8.942	0.826 ± 0.026	AC-AW
4047.811	25.771	−12.969	0.710 ± 0.046	AC-AE
4047.811	−31.074	−12.034	0.812 ± 0.051	AC-AW
4047.831	26.734	−10.502	0.745 ± 0.031	AC-AE
4047.831	−30.182	−14.913	0.921 ± 0.053	AC-AW
4047.856	27.340	−7.336	0.796 ± 0.018	AC-AE
4047.856	−28.406	−18.343	0.940 ± 0.149	AC-AW
4047.937	36.582	67.909	0.722 ± 0.042	AC-W7
4047.937	−18.081	−27.427	0.932 ± 0.065	AC-AW
4047.937	36.566	67.878	0.755 ± 0.035	AC-W7
4047.937	18.484	40.451	0.837 ± 0.035	AW-W7
4048.747	20.317	−19.743	0.759 ± 0.025	AC-AE
4048.747	−30.703	−2.954	0.849 ± 0.033	AC-AW
4048.805	25.562	−13.386	0.743 ± 0.018	AC-AE
4048.805	−31.179	−11.528	0.867 ± 0.030	AC-AW
4048.829	26.747	−10.457	0.746 ± 0.018	AC-AE
4048.829	−30.161	−14.964	0.890 ± 0.031	AC-AW
4048.850	27.295	−7.779	0.738 ± 0.029	AC-AE
4048.850	−28.695	−17.880	0.975 ± 0.042	AC-AW
4048.868	27.384	−5.450	0.742 ± 0.071	AC-AE
4048.868	−27.030	−20.253	0.997 ± 0.047	AC-AW
4048.929	25.097	2.150	0.891 ± 0.036	AC-AE

JD-2,450,000	u (m)	v (m)	V^2 (arbitrary)	Baseline
4048.929	38.773	66.881	0.686 ± 0.037	AC-W7
4048.929	63.870	69.031	0.683 ± 0.032	AE-W7
4048.929	−19.012	−26.921	0.902 ± 0.054	AC-AW
4048.929	38.756	66.851	0.761 ± 0.042	AC-W7
4048.929	19.744	39.929	0.873 ± 0.029	AW-W7
4049.746	20.583	−19.520	0.764 ± 0.026	AC-AE
4049.746	−30.803	−3.290	0.898 ± 0.048	AC-AW
4049.781	24.007	−15.880	0.764 ± 0.027	AC-AE
4049.781	−31.496	−8.375	0.889 ± 0.049	AC-AW
4049.819	26.465	−11.319	0.805 ± 0.025	AC-AE
4049.819	−30.527	−13.981	0.760 ± 0.059	AC-AW
4049.849	27.324	−7.504	0.833 ± 0.060	AC-AE
4049.849	−28.517	−18.168	0.913 ± 0.116	AC-AW
4049.950	23.178	4.849	0.876 ± 0.045	AC-AE
4049.950	−15.054	−28.826	0.913 ± 0.075	AC-AW
4050.744	20.638	−19.473	0.780 ± 0.020	AC-AE
4050.744	−30.823	−3.360	0.831 ± 0.048	AC-AW
4050.778	23.999	−15.892	0.842 ± 0.025	AC-AE
4050.778	−31.497	−8.360	0.861 ± 0.040	AC-AW
4050.817	26.477	−11.285	0.778 ± 0.022	AC-AE
4050.817	−30.513	−14.020	0.934 ± 0.031	AC-AW
4050.842	27.267	−8.010	0.803 ± 0.038	AC-AE
4050.842	−28.841	−17.636	0.968 ± 0.031	AC-AW
4050.946	23.242	4.773	0.859 ± 0.065	AC-AE
4050.946	29.792	70.602	0.717 ± 0.059	AC-W7
4050.946	53.035	75.375	0.781 ± 0.059	AE-W7
4050.946	−15.176	−28.777	0.978 ± 0.150	AC-AW
4050.946	29.779	70.570	0.716 ± 0.064	AC-W7
4050.946	14.603	41.793	0.831 ± 0.046	AW-W7
4053.820	26.930	−9.788	0.734 ± 0.059	AC-AE
4053.820	−29.841	−15.712	0.901 ± 0.076	AC-AW
4054.749	22.319	−17.885	0.766 ± 0.044	AC-AE
4054.749	−31.313	−5.657	0.925 ± 0.037	AC-AW

JD-2,450,000	u (m)	v (m)	V^2 (arbitrary)	Baseline
4054.787	25.456	−13.588	0.769 ± 0.021	AC-AE
4054.787	−31.224	−11.282	0.831 ± 0.022	AC-AW
4054.812	26.747	−10.456	0.822 ± 0.032	AC-AE
4054.812	−30.161	−14.965	0.857 ± 0.047	AC-AW
4054.838	27.351	−7.192	0.769 ± 0.042	AC-AE
4054.838	−28.309	−18.492	0.879 ± 0.026	AC-AW
4054.858	27.325	−4.583	0.798 ± 0.040	AC-AE
4054.858	−26.318	−21.099	0.895 ± 0.042	AC-AW
4055.741	21.799	−18.412	0.772 ± 0.027	AC-AE
4055.741	−31.188	−4.910	0.840 ± 0.063	AC-AW
4055.777	24.977	−14.431	0.760 ± 0.039	AC-AE
4055.777	−31.378	−10.235	0.903 ± 0.023	AC-AW
4055.804	26.530	−11.133	0.780 ± 0.045	AC-AE
4055.804	−30.453	−14.194	0.886 ± 0.030	AC-AW
4055.812	26.845	−10.111	0.800 ± 0.045	AC-AE
4055.812	−30.000	−15.351	0.824 ± 0.068	AC-AW
4055.830	27.290	−7.824	0.762 ± 0.057	AC-AE
4055.830	−28.724	−17.833	0.860 ± 0.047	AC-AW
4055.847	27.390	−5.671	0.827 ± 0.040	AC-AE
4055.847	−27.203	−20.035	0.873 ± 0.040	AC-AW
4055.967	19.622	8.216	0.905 ± 0.047	AC-AE
4055.967	15.439	74.235	0.658 ± 0.048	AC-W7
4055.967	35.061	82.450	0.733 ± 0.043	AE-W7
4055.967	−8.951	−30.714	0.894 ± 0.043	AC-AW
4055.967	15.432	74.201	0.672 ± 0.032	AC-W7
4055.967	6.481	43.486	0.815 ± 0.023	AW-W7
4056.011	13.636	11.678	1.001 ± 0.053	AC-AE
4056.011	−4.067	75.419	0.622 ± 0.040	AC-W7
4056.011	9.569	87.096	0.685 ± 0.042	AE-W7
4056.011	−0.339	−31.681	0.858 ± 0.048	AC-AW
4056.011	−4.065	75.384	0.647 ± 0.018	AC-W7
4056.011	−4.404	43.703	0.746 ± 0.042	AW-W7
4056.745	22.513	−17.675	0.731 ± 0.024	AC-AE

JD-2,450,000	u (m)	v (m)	V^2 (arbitrary)	Baseline
4056.745	−31.361	−5.962	0.919 ± 0.028	AC-AW
4056.783	25.580	−13.351	0.707 ± 0.020	AC-AE
4056.783	−31.171	−11.584	0.852 ± 0.020	AC-AW
4056.806	26.714	−10.572	0.762 ± 0.018	AC-AE
4056.806	−30.210	−14.847	0.933 ± 0.016	AC-AW
4056.824	27.225	−8.338	0.743 ± 0.018	AC-AE
4056.824	−29.035	−17.300	0.862 ± 0.023	AC-AW
4056.840	27.398	−6.281	0.771 ± 0.023	AC-AE
4056.840	−27.656	−19.435	0.910 ± 0.019	AC-AW
4056.856	27.290	−4.201	0.789 ± 0.017	AC-AE
4056.856	−25.977	−21.475	0.930 ± 0.023	AC-AW
4056.943	22.033	6.117	0.844 ± 0.024	AC-AE
4056.943	24.659	72.214	0.639 ± 0.034	AC-W7
4056.943	46.692	78.331	0.704 ± 0.035	AE-W7
4056.943	−12.917	−29.612	0.871 ± 0.047	AC-AW
4056.943	24.648	72.181	0.693 ± 0.024	AC-W7
4056.943	11.731	42.569	0.805 ± 0.020	AW-W7
4056.983	17.261	9.839	0.930 ± 0.035	AC-AE
4056.983	7.298	75.241	0.645 ± 0.048	AC-W7
4056.983	24.558	85.080	0.621 ± 0.038	AE-W7
4056.983	−5.323	−31.339	0.771 ± 0.053	AC-AW
4056.983	7.294	75.206	0.702 ± 0.034	AC-W7
4056.983	1.971	43.867	0.766 ± 0.031	AW-W7
4057.014	12.690	12.080	0.914 ± 0.043	AC-AE
4057.014	−6.826	75.276	0.576 ± 0.034	AC-W7
4057.014	5.863	87.355	0.589 ± 0.047	AE-W7
4057.014	0.951	−31.667	0.799 ± 0.051	AC-AW
4057.014	−6.823	75.241	0.580 ± 0.030	AC-W7
4057.014	−5.872	43.575	0.721 ± 0.015	AW-W7
4057.045	7.865	13.543	0.999 ± 0.021	AC-AE
4057.045	−20.027	73.364	0.628 ± 0.043	AC-W7
4057.045	−12.162	86.907	0.554 ± 0.050	AE-W7
4057.045	6.892	−31.108	0.793 ± 0.046	AC-AW

JD-2,450,000	u (m)	v (m)	V^2 (arbitrary)	Baseline
4057.045	−20.018	73.330	0.648 ± 0.028	AC-W7
4057.045	−13.126	42.222	0.678 ± 0.027	AW-W7
4057.964	19.281	8.472	0.946 ± 0.041	AC-AE
4057.964	14.216	74.430	0.641 ± 0.049	AC-W7
4057.964	33.496	82.902	0.695 ± 0.028	AE-W7
4057.964	−8.416	−30.829	0.773 ± 0.089	AC-AW
4057.964	14.209	74.396	0.710 ± 0.041	AC-W7
4057.964	5.793	43.567	0.773 ± 0.061	AW-W7
4058.002	14.152	11.451	0.910 ± 0.038	AC-AE
4058.002	−2.522	75.472	0.630 ± 0.049	AC-W7
4058.002	11.630	86.924	0.638 ± 0.034	AE-W7
4058.002	−1.027	−31.670	0.654 ± 0.073	AC-AW
4058.002	−2.520	75.438	0.620 ± 0.035	AC-W7
4058.002	−3.548	43.768	0.745 ± 0.066	AW-W7
4058.026	10.406	12.857	0.940 ± 0.031	AC-AE
4058.026	−13.289	74.567	0.618 ± 0.037	AC-W7
4058.026	−2.883	87.424	0.673 ± 0.023	AE-W7
4058.026	3.790	−31.512	0.814 ± 0.044	AC-AW
4058.026	−13.283	74.533	0.619 ± 0.026	AC-W7
4058.026	−9.492	43.021	0.635 ± 0.052	AW-W7
4058.052	6.184	13.861	0.950 ± 0.028	AC-AE
4058.052	−24.323	72.291	0.578 ± 0.033	AC-W7
4058.052	−18.139	86.152	0.607 ± 0.042	AE-W7
4058.052	8.782	−30.751	0.763 ± 0.096	AC-AW
4058.052	−24.312	72.258	0.651 ± 0.041	AC-W7
4058.052	−15.530	41.507	0.574 ± 0.064	AW-W7
4059.964	18.563	8.984	0.930 ± 0.085	AC-AE
4059.964	11.693	74.780	0.645 ± 0.084	AC-W7
4059.964	−7.310	−31.041	0.918 ± 0.064	AC-AW
4059.964	11.688	74.746	0.692 ± 0.036	AC-W7
4059.964	4.378	43.705	0.798 ± 0.026	AW-W7
4060.030	8.923	13.274	0.959 ± 0.057	AC-AE
4060.030	−17.287	73.907	0.687 ± 0.074	AC-W7

JD-2,450,000	u (m)	v (m)	V^2 (arbitrary)	Baseline
4060.030	5.592	−31.310	0.830 ± 0.058	AC-AW
4060.030	−17.279	73.874	0.727 ± 0.061	AC-W7
4060.030	−11.687	42.564	0.732 ± 0.053	AW-W7
4060.918	23.311	4.709	0.825 ± 0.037	AC-AE
4060.918	30.088	70.513	0.711 ± 0.034	AC-W7
4060.918	53.399	75.222	0.706 ± 0.036	AE-W7
4060.918	−15.262	−28.736	0.824 ± 0.068	AC-AW
4060.918	30.074	70.481	0.691 ± 0.035	AC-W7
4060.918	14.813	41.744	0.804 ± 0.057	AW-W7
4060.990	14.681	11.223	0.926 ± 0.028	AC-AE
4060.990	−0.899	75.518	0.653 ± 0.045	AC-W7
4060.990	13.782	86.740	0.691 ± 0.050	AE-W7
4060.990	−1.692	−31.643	0.877 ± 0.065	AC-AW
4060.990	−0.898	75.483	0.695 ± 0.045	AC-W7
4060.990	−2.591	43.840	0.660 ± 0.039	AW-W7
4061.914	23.456	4.532	0.831 ± 0.038	AC-AE
4061.914	30.736	70.283	0.739 ± 0.049	AC-W7
4061.914	54.192	74.815	0.730 ± 0.029	AE-W7
4061.914	−15.540	−28.620	0.996 ± 0.070	AC-AW
4061.914	30.722	70.251	0.700 ± 0.027	AC-W7
4061.914	15.181	41.631	0.823 ± 0.022	AW-W7
4061.982	15.420	10.860	0.890 ± 0.036	AC-AE
4061.982	1.385	75.512	0.634 ± 0.030	AC-W7
4061.982	16.805	86.372	0.682 ± 0.026	AE-W7
4061.982	−2.707	−31.590	0.752 ± 0.080	AC-AW
4061.982	1.384	75.477	0.695 ± 0.023	AC-W7
4061.982	−1.322	43.887	0.730 ± 0.036	AW-W7
4062.011	11.066	12.662	0.934 ± 0.038	AC-AE
4062.011	−11.439	74.828	0.592 ± 0.030	AC-W7
4062.011	−0.372	87.490	0.602 ± 0.030	AE-W7
4062.011	3.018	−31.569	0.704 ± 0.049	AC-AW
4062.011	−11.433	74.794	0.632 ± 0.027	AC-W7
4062.011	−8.415	43.224	0.712 ± 0.025	AW-W7

JD-2,450,000	u (m)	v (m)	V^2 (arbitrary)	Baseline
4062.964	17.563	9.638	0.940 ± 0.069	AC-AE
4062.964	8.293	75.142	0.568 ± 0.100	AC-W7
4062.964	25.856	84.780	0.670 ± 0.088	AE-W7
4062.964	8.289	75.108	0.765 ± 0.101	AC-W7
5202.662	−26.225	45.990	0.738 ± 0.022	AE-AN
5202.662	57.757	2.363	0.678 ± 0.026	AE-AW
5202.662	−26.221	45.983	0.650 ± 0.045	AE-AN
5202.662	31.537	48.346	0.803 ± 0.028	AN-AW
5202.684	−29.827	43.062	0.713 ± 0.026	AE-AN
5202.684	57.160	8.366	0.723 ± 0.032	AE-AW
5202.684	−29.822	43.056	0.721 ± 0.038	AE-AN
5202.684	27.338	51.422	0.791 ± 0.032	AN-AW
5202.708	−33.061	39.514	0.712 ± 0.026	AE-AN
5202.708	55.264	14.709	0.744 ± 0.019	AE-AW
5202.708	−33.056	39.508	0.728 ± 0.047	AE-AN
5202.708	22.208	54.217	0.797 ± 0.029	AN-AW
5202.715	−33.950	38.291	0.695 ± 0.022	AE-AN
5202.715	54.376	16.710	0.738 ± 0.022	AE-AW
5202.715	−33.945	38.285	0.627 ± 0.049	AE-AN
5202.715	20.431	54.995	0.777 ± 0.026	AN-AW
5202.736	−35.918	34.891	0.708 ± 0.027	AE-AN
5202.736	51.385	21.857	0.809 ± 0.019	AE-AW
5202.736	−35.912	34.885	0.636 ± 0.031	AE-AN
5202.736	15.472	56.743	0.767 ± 0.034	AN-AW
5202.745	−36.589	33.347	0.723 ± 0.040	AE-AN
5202.745	49.796	24.012	0.765 ± 0.027	AE-AW
5202.745	−36.584	33.342	0.630 ± 0.047	AE-AN
5202.745	13.213	57.353	0.730 ± 0.032	AN-AW
5202.764	−37.586	30.131	0.731 ± 0.024	AE-AN
5202.764	46.070	28.168	0.825 ± 0.026	AE-AW
5202.764	−37.580	30.126	0.688 ± 0.044	AE-AN
5202.764	8.490	58.294	0.704 ± 0.034	AN-AW
5202.784	−38.099	26.477	0.717 ± 0.054	AE-AN

JD-2,450,000	u (m)	v (m)	V^2 (arbitrary)	Baseline
5202.784	41.194	32.381	0.825 ± 0.043	AE-AW
5202.784	−38.093	26.473	0.567 ± 0.079	AE-AN
5202.784	3.101	58.854	0.683 ± 0.049	AN-AW
5202.806	−37.957	22.648	0.729 ± 0.036	AE-AN
5202.806	35.381	36.236	0.799 ± 0.039	AE-AW
5202.806	−37.951	22.645	0.701 ± 0.043	AE-AN
5202.806	−2.571	58.881	0.745 ± 0.039	AN-AW
5203.648	−24.187	47.335	0.649 ± 0.025	AE-AN
5203.648	57.627	−0.702	0.703 ± 0.017	AE-AW
5203.648	−24.183	47.328	0.694 ± 0.028	AE-AN
5203.648	33.443	46.626	0.834 ± 0.023	AN-AW
5203.671	−28.247	44.455	0.704 ± 0.022	AE-AN
5203.671	57.573	5.626	0.729 ± 0.022	AE-AW
5203.671	−28.243	44.448	0.707 ± 0.034	AE-AN
5203.671	29.330	50.074	0.797 ± 0.022	AN-AW
5203.708	−33.426	39.042	0.729 ± 0.025	AE-AN
5203.708	54.930	15.499	0.736 ± 0.020	AE-AW
5203.708	−33.421	39.036	0.639 ± 0.036	AE-AN
5203.708	21.509	54.536	0.744 ± 0.025	AN-AW
5203.717	−34.434	37.576	0.698 ± 0.022	AE-AN
5203.717	53.805	17.848	0.764 ± 0.018	AE-AW
5203.717	−34.429	37.571	0.660 ± 0.030	AE-AN
5203.717	19.377	55.419	0.757 ± 0.025	AN-AW
5203.736	−36.148	34.420	0.679 ± 0.054	AE-AN
5203.736	50.911	22.531	0.822 ± 0.040	AE-AW
5203.736	−36.143	34.415	0.674 ± 0.057	AE-AN
5203.736	14.768	56.946	0.798 ± 0.055	AN-AW
5203.746	−36.847	32.696	0.701 ± 0.023	AE-AN
5203.746	49.083	24.893	0.785 ± 0.026	AE-AW
5203.746	−36.841	32.691	0.659 ± 0.048	AE-AN
5203.746	12.242	57.584	0.725 ± 0.023	AN-AW
5203.766	−37.779	29.269	0.693 ± 0.030	AE-AN
5203.766	44.978	29.212	0.806 ± 0.037	AE-AW

JD-2,450,000	u (m)	v (m)	V^2 (arbitrary)	Baseline
5203.766	−37.773	29.265	0.730 ± 0.043	AE-AN
5203.766	7.205	58.477	0.687 ± 0.048	AN-AW
5203.797	−38.085	23.742	0.732 ± 0.034	AE-AN
5203.797	37.115	35.194	0.849 ± 0.025	AE-AW
5203.797	−38.080	23.738	0.633 ± 0.041	AE-AN
5203.797	−0.964	58.932	0.680 ± 0.027	AN-AW
5204.688	−31.220	41.682	0.644 ± 0.047	AE-AN
5204.688	56.551	10.947	0.783 ± 0.063	AE-AW
5204.688	−31.215	41.676	0.490 ± 0.075	AE-AN
5204.688	25.336	52.623	0.770 ± 0.067	AN-AW
5205.796	−37.999	22.848	0.811 ± 0.063	AE-AN
5205.796	35.704	36.049	0.823 ± 0.046	AE-AW
5205.796	−37.993	22.845	0.654 ± 0.044	AE-AN
5205.796	−2.290	58.893	0.712 ± 0.034	AN-AW
5206.734	49.910	23.867	0.836 ± 0.035	AE-AW
5208.637	−24.802	46.951	0.655 ± 0.034	AE-AN
5208.637	57.695	0.202	0.710 ± 0.024	AE-AW
5208.637	−24.798	46.944	0.674 ± 0.031	AE-AN
5208.637	32.898	47.146	0.865 ± 0.028	AN-AW
5208.660	−28.707	44.070	0.675 ± 0.023	AE-AN
5208.660	57.480	6.404	0.770 ± 0.028	AE-AW
5208.660	−28.703	44.063	0.647 ± 0.026	AE-AN
5208.660	28.777	50.467	0.783 ± 0.016	AN-AW
5208.692	−33.154	39.406	0.645 ± 0.040	AE-AN
5208.692	55.186	14.898	0.752 ± 0.026	AE-AW
5208.692	−33.149	39.400	0.744 ± 0.064	AE-AN
5208.692	22.037	54.298	0.803 ± 0.031	AN-AW
5208.702	−34.241	37.874	0.713 ± 0.033	AE-AN
5208.702	54.046	17.381	0.788 ± 0.025	AE-AW
5208.702	−34.236	37.868	0.696 ± 0.055	AE-AN
5208.702	19.810	55.249	0.793 ± 0.032	AN-AW
5208.720	−35.986	34.772	0.674 ± 0.024	AE-AN
5208.720	51.264	22.032	0.815 ± 0.020	AE-AW

JD-2,450,000	u (m)	v (m)	V^2 (arbitrary)	Baseline
5208.720	−35.980	34.767	0.699 ± 0.032	AE-AN
5208.720	15.283	56.799	0.810 ± 0.028	AN-AW
5208.730	−36.650	33.223	0.705 ± 0.015	AE-AN
5208.730	49.659	24.186	0.809 ± 0.025	AE-AW
5208.730	−36.645	33.217	0.668 ± 0.023	AE-AN
5208.730	13.014	57.403	0.755 ± 0.021	AN-AW
5208.749	−37.672	29.806	0.668 ± 0.031	AE-AN
5208.749	45.661	28.568	0.822 ± 0.021	AE-AW
5208.749	−37.666	29.801	0.721 ± 0.035	AE-AN
5208.749	7.995	58.369	0.734 ± 0.019	AN-AW
5208.758	−37.941	28.274	0.712 ± 0.025	AE-AN
5208.758	43.674	30.377	0.840 ± 0.020	AE-AW
5208.758	−37.936	28.270	0.675 ± 0.022	AE-AN
5208.758	5.738	58.647	0.734 ± 0.018	AN-AW
5208.776	−38.142	24.942	0.711 ± 0.039	AE-AN
5208.776	38.950	33.995	0.873 ± 0.046	AE-AW
5208.776	−38.136	24.938	0.728 ± 0.060	AE-AN
5208.776	0.815	58.934	0.703 ± 0.033	AN-AW
5208.806	−37.368	19.622	0.741 ± 0.038	AE-AN
5208.806	30.276	38.873	0.857 ± 0.022	AE-AW
5208.806	−37.363	19.619	0.737 ± 0.047	AE-AN
5208.806	−7.087	58.492	0.731 ± 0.034	AN-AW

Bethany Grzenia *Curriculum Vitæ*

Experience

The University of Western Ontario — London, ON, CA
- **Graduate Research Assistant** — *September 2012 – present*
- **Graduate Teaching Assistant** — *September 2012 – April 2016*

University of Cincinnati Blue Ash College — Blue Ash, OH, US
- **Visiting Professor of Physics** — *September 2011 – August 2012*

Central Michigan University — Mount Pleasant, MI, US
- **Lecturer** — *January 2010 – August 2011*
- **Graduate Assistant** — *September 2007 – December 2009*

Delta College — University Center, MI, US
- **Adjunct Lecturer** — *January – May 2010*
- *January – May 2007*

University of Missouri-Rolla — Rolla, MO, US
- **Technical Staff and Graduate Assistant** — *September 2003 – May 2006*

Argonne National Laboratory — Argonne, IL, US
- **Intern** — *May 2003 – August 2003*
- *May 2002 – August 2002*

Education

The University of Western Ontario — London, ON, CA
- **Doctor of Philosophy in Astronomy** — *2012 – 2016*
  Supervisor: C. E. Jones
  Thesis topic: computational astrophysics

Central Michigan University — Mount Pleasant, MI, US
- **Master of Science in Physics** — *2007 – 2009*
  Supervisor: C. Tycner
  Thesis topic: observational astronomy

Illinois Institute of Technology — Chicago, IL, US
- **Bachelor of Science with Honors in Physics** — *1999 – 2003*
  Supervisors: C. U. Segre and J. Terry
  Research areas: materials physics, synchrotron radiation

Natural languages: English *(native speaker)*, French *(limited working proficiency)*, Spanish *(limited working proficiency)* and Polish *(elementary proficiency)*

Recognitions

K. P. Brooks Astronomy Award: Received in 2010 from Central Michigan University Department of Physics

Publications and Presentations

Publications:

Grzenia, B. J., Tycner, C., Jones, C. E., et al. 2013, AJ, 145, 141.

Terry, J., Grzenia, B., Papagiannopoulou, D., Kyger, J., Jurrison, S., et al. 2005, Journal of Radioanalytical and Nuclear Chemistry, Volume 263, Number 2, Pages 531-537.

Presentations:

The Disks Surrounding 48 Per and psi Per, Bright Emissaries Conference, 2014

Investigations of Be Star Disks with the Palomar Testbed Interferometer, University of Western Ontario, 2013

Observation and Modelling of Hot Stars, Illinois Institute of Technology, 2010

Determining Be Star Disk Characteristics using Data from the Palomar Testbed Interferometer, Grzenia, Bethany J.; Tycner, C.; Rinehart, S.; van Belle, G.; Jones, C. E.; Sigut, T. A. A. 2009, AAS, 21340913G

Hot Disks Around Early-Type Stars: Hα and K-band Interferometry, Tycner, Christopher; Grzenia, B. J.; Rinehart, S.; van Belle, G.; Jones, C. E.; Sigut, T. A. A. 2009, AAS, 21335803T

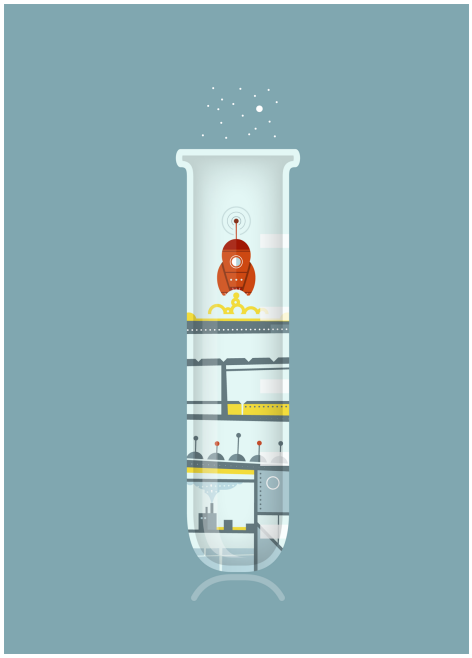

This thesis was typeset using LaTeX, originally developed by Leslie Lamport and based on Donald Knuth's TeX. The body text is set in 11 point Egenolff-Berner Garamond, a revival of Claude Garamont's humanist typeface. The above illustration, *Science Experiment 02*, was created by Ben Schlitter and released under CC BY-NC-ND 3.0. A template that can be used to format a PhD dissertation with this look & feel has been released under the permissive AGPL license, and can be found online at github.com/suchow/Dissertate or from its lead author, Jordan Suchow, at suchow@post.harvard.edu.